DEVELOPMENT AND CHARACTERIZATION OF FURNACE ATOMIZATION PLASMA EXCITATION SPECTROMETRY

by

TERRANCE DAYAKANTHA HETTIPATHIRANA

B.Sc., University of Colombo, Sri Lanka, 1985
M.Sc., University of British Columbia, 1989

A THESIS SUBMITTED IN PARTIAL FULFILLMENT OF

THE REQUIREMENTS FOR THE DEGREE OF

DOCTOR OF PHILOSOPHY

in

THE FACULTY OF GRADUATE STUDIES

DEPARTMENT OF CHEMISTRY

We accept this thesis as conforming

to the required standard

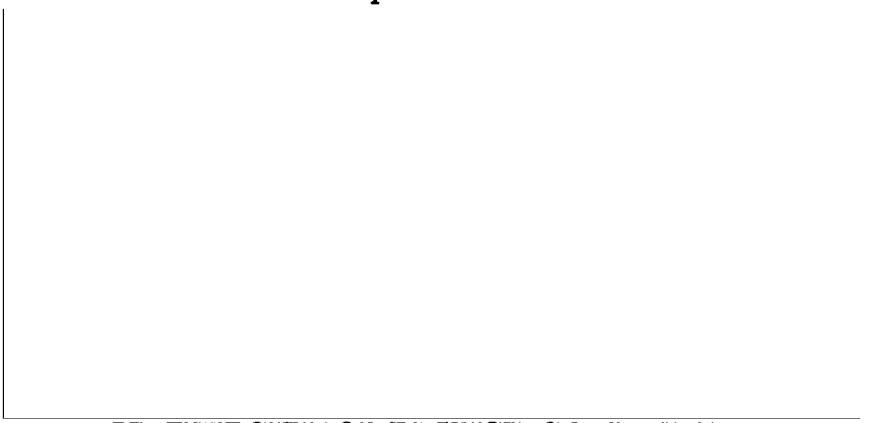

UNIVERSITY OF BRITISH COLUMBIA

July 1993

In presenting this thesis in partial fulfilment of the requirements for an advanced degree at the University of British Columbia, I agree that the Library shall make it freely available for reference and study. I further agree that permission for extensive copying of this thesis for scholarly purposes may be granted by the head of my department or by his or her representatives. It is understood that copying or publication of this thesis for financial gain shall not be allowed without my written permission.

(Signature) _____

Department of CHEMISTRY.

The University of British Columbia
Vancouver, Canada

Date Aug 23, 1993

DE-6 (2/88)

ABSTRACT

Furnace Atomization Plasma Excitation Spectrometry (FAPES) is a new emission spectrochemical method which employs a graphite furnace for analyte atomization and an atmospheric pressure plasma sustained inside the furnace for analyte excitation. The primary objective of this work was to characterize the fundamental processes that are occurring within the plasma during the analyte atomization, vaporization, and excitation.

Background spectra are dominated by emission features from CO^+, N_2^+, OH, NH, and N_2. The plasma background emission is most intense near the radio frequency (RF) electrode and less intense near the graphite furnace wall. The Fe and Pb-excitation temperatures are in the range of 3000 - 5000 K at RF powers between 10 and 100 W. The Fe-excitation temperature also exhibits a spatial dependence. The emission features of CO^+ and N_2^+ indicate that this plasma source is capable of exciting energy levels as high as 20 eV.

Both atomic absorption and emission experiments show a non-uniform temperature distribution along the length of the RF electrode. The temperature lag of the RF electrode relative to the furnace wall causes condensation of analytes on the RF electrode and subsequent second-surface vaporization resulting in two peaks in the temporal response of the emission signal. Analyte condensation on the RF electrode is severe at low RF powers and can be observed when high amounts of analyte are deposited. Similar temporal responses are observed for simultaneously measured atomic

absorption and emission signals for Ag and Pb. The time-resolved Pb-excitation temperature also suggests that the temporal emission profiles of these analytes in FAPES are determined by atomization and vaporization characteristics of the analyte rather than by excitation characteristics.

Results obtained for Pb also show an early shift in the appearance and peak temperatures in FAPES compared with those in Graphite Furnace Atomic Absorption Spectrometry (GFAAS), probably because of a shift in the dissociation equilibria of Pb species in the gas-phase. Experimental results show the presence of high levels of CO in the FAPES source due to the enhanced oxidation of graphite on the RF electrode and on the graphite furnace wall in the presence of the plasma. At RF powers higher than 50 W, the Pb emission intensity decreases. The highest signal-to-noise and signal-to-background ratios are observed at relatively low RF powers (about 20 W).

For both Pb and Ag, the major cause of interference effects from NaCl is the formation of volatile molecular species which are lost prior to atomization, and consequently, leads to a decrease in the atomic emission intensity in FAPES. The interference effect for both Pb and Ag in a $NaNO_3$ matrix is complex and exhibits both condensed and gas-phase effects.

The work presented in this thesis demonstrates that the FAPES source has the potential to be a potent excitation source for atomic emission spectrometry. This work also identifies the limitations of FAPES and suggests further improvements to the instrumentation.

TABLE OF CONTENTS

Abstract ii

Table of Contents iv

List of Tables viii

List of Figures ix

List of Abbreviations xv

Acknowledgements xvii

Chapter 1

Introduction 1

1.1 FAPES: Historical Development 2

1.2 Furnace Atomization Plasma Excitation Spectrometry 8

1.3 Analyte Atomization: The Graphite Furnace 11

1.3.1 L'vov Furnace 12

1.3.2 Massmann Furnace 13

1.3.3 Limitations of Massmann-type Furnaces 15

1.3.3.1 L'vov Platform 16

1.3.3.2 Integrated Contact Cuvette 17

1.3.4 Atomization Mechanisms 18

1.4 Analyte Excitation: The Plasma 20

1.4.1 The RF Discharge at Atmospheric Pressure 21

1.4.2 The RF Discharge in FAPES 25

1.4.3 Excitation Mechanisms 26

1.4.4 Plasma Temperature 29

1.4.5 Spectroscopic Temperature Measurements 31

1.5 Overview of the Thesis 34

Chapter 2

The Experimental System 36

2.1 Instrumentation 36

2.1.1 The Plasma Source Work-Head 38

2.1.2 The Atmospheric Pressure RF Discharge 41
2.1.3 Spatially Resolved Intensity Measurements 43
2.1.4 Spectral Isolation and Detection 43
2.1.5 Atomic Absorption Measurements 44
2.1.6 Graphite Furnace Temperature Measurements 45
2.2 Data Acquisition 46
2.3 Data Processing 47
2.4 The FAPES Method 47

Chapter 3
Spectral and Excitation Characteristics of the Atmospheric Pressure Helium Plasma Source in FAPES 49
3.1 Introduction 49
3.2 Experimental 51
3.2.1 Plasma Background and Iron Emission Spectra 51
3.2.2 Spatially and Temporally Resolved Spectra 53
3.3 Results and Discussion 54
3.3.1 Background Emission Spectra 54
3.3.2 Spatially Resolved Background Emission Intensities 61
3.3.3 Temporally Resolved Background Emission Intensities . . . 64
3.3.4 Fe-Excitation Temperatures 69
3.3.5 Atmospheric Pressure Ar Plasma 74
3.4 Summary 76

Chapter 4
Temporal Emission and Absorption Characteristics of Silver, Lead, and Manganese in FAPES 78
4.1 Introduction 78
4.2 Experimental 80
4.2.1 Signal Presentation 80
4.2.2 Appearance and Peak Temperatures 81
4.2.3 Reagents 81
4.2.4 Procedure 81
4.3 Results and Discussion 82

4.3.1 Silver 83
4.3.2 Lead 93
4.3.3 Manganese 107
4.4 Summary 116

Chapter 5
Emission Characteristics and Figures of Merit for Lead in FAPES 118
5.1 Introduction 118
5.2 Experimental 121
5.2.1 Signal Presentation 122
5.2.2 Reagents 122
5.2.3 Procedure 122
5.3 Results and Discussion 123
5.3.1 Time-resolved Pb-excitation temperature 123
5.3.2 Effect of RF power 128
5.3.3 Signal-to-Noise ratio 133
5.3.4 Figures of merit 143
5.4 Summary 149

Chapter 6
Effects of Sodium Chloride and Sodium Nitrate on the Lead and Silver Emission in FAPES 151
6.1 Introduction 151
6.2 Experimental 154
6.2.1 Signal Presentation 154
6.2.2 Reagents 154
6.2.3 Procedure 155
6.3 Results and Discussion 156
6.3.1 Reflected Power 156
6.3.2 Temporal Response of Na (as NaCl and $NaNO_3$) 158
6.3.3 Effects of NaCl and $NaNO_3$ on the Pb Emission Intensity . 161
6.3.4 Effects of NaCl and $NaNO_3$ on the Ag Emission Intensity . 172
6.3.5 Effects of ascorbic acid and phosphoric acid 178

6.4 Summary 185

Chapter 7
Conclusions 188

Bibliography 195

LIST OF TABLES

TABLE PAGE

3.1. Transitions of species observed in helium plasma at atmospheric pressure in 215 - 515 nm range. 58

3.2. Fe (I) lines used for the temperature measurement and relevant spectral data [83]. 70

5.1. Wavelengths, Excitation energies, and Spectral characteristics for Pb lines used for the Pb-excitation temperature determination [122]. 124

LIST OF FIGURES

FIGURES PAGE

1.1. Schematic diagram of the FANES source. (Adapted from H. Falk, E. Hoffmann, and Ch. Ludke, *Spectrochim. Acta*, 283, **39B** (1984), with permission of Pergamon Journal Inc.) 5

1.2. Schematic diagram of the HA-FANES source. (Adapted from N. E. Ballou, D. L. Styris, and J. M. Harnly, *J. Anal. At. Spectrom.*, 1141, **3** (1988), with permission of The Royal Society of Chemistry.) 7

1.3. Schematic diagram of the FAPES source. (Adapted from D. C. Liang and M. W. Blades, *Spectrochim. Acta*, 1049, **44B** (1989), with permission of Pergamon Journal Inc.) 9

1.4. Schematic diagram of the L'vov graphite furnace and electrode assembly. (Adapted from B. V. L'vov, *Spectrochim. Acta*, 53, **24B** (1969), with permission of Pergamon Journal Inc.) 13

1.5. Schematic diagram of the Massmann graphite furnace. (Adapted from H. Massmann, *Spectrochim. Acta*, 215, **23B** (1968), with permission of Pergamon Journal Inc.) 14

1.6. Schematic representation of the L'vov platform inside the graphite furnace. 17

1.7. Schematic diagram of an RF discharge system. 24

2.1. Schematic diagram of the experimental system. 37

2.2. Schematic diagram of the plasma source work-head. 39

2.3. End view of the (a) vertical mount and (b) horizontal mount. The dash line represents the RF connector. 41

3.1. Background Spectra of helium plasma. (a) 215 - 300 nm, (b) 300 - 400 nm, and (c) 400 - 515 nm. 57

FIGURES PAGE

3.2. Emission spatial profile for CO^+. 62

3.3. Temporal emission behavior for (a) He (I), (b) CO^+, (c) N_2^+, and (d) OH at RF powers of 14, 18, 22, 26, and 30 W; (e) furnace temperature corresponding to these diagrams. 68

3.4. Emission spectrum for 50 ng Fe at an RF power of 20 W. 71

3.5. Iron excitation temperature as a function of RF power. 73

3.6. Background spectrum of the Ar plasma for the spectral region, 220 - 260 nm. 75

4.1. Temporal response of the Ag atomic absorption signal at an RF power of 0 W for 0.5 ng of Ag deposited on the furnace wall with (- - -) and without (——) the graphite co-axial rod; background (· · ·); and the temperature profile of the furnace wall (— — —). 84

4.2. Temporal response of the Ag atomic absorption signal at an RF power of 0 W for 0.5 ng of Ag deposited on the graphite co-axial rod (——) and tungsten co-axial rod (- - -); and background (· · ·). 86

4.3. Temporal response of the Ag atomic emission signal at an RF power of 20 W for 0.5 ng of Ag deposited on the furnace wall (——) and RF electrode (- - -); and background (· · ·). 88

4.4. Temporal response of the Ag atomic emission signal at an RF power of 20 W for Ag deposited on the furnace wall. Analyte amounts: 0.05 (——), 0.25 (- - -), 0.50 (- · - · -), and 5.0 ng (— — —); and background (· · ·) at 20 W. 90

4.5. Temporal response of the Ag atomic emission signal for 0.5 ng of Ag deposited on the furnace wall at an RF power of 14 (——), 20 (- - -), 26 (- · - · -), 32 (— — —), and 38 W (- ··· - ···); and background at 20 W (· · ·). 91

FIGURES PAGE

4.6. Temporal response of the Ag atomic absorption signal for 0.5 ng of Ag deposited on the furnace wall at an RF power of 20 (· · ·) and 40 W (- - -). 92

4.7. Temporal response of the Pb atomic absorption signal at an RF power of 0 W for 5 ng of Pb deposited on the furnace wall with (- - -) and without (——) the co-axial rod; and background (· · ·). 94

4.8. Temporal response of the Pb atomic absorption signal at an RF power of 0 W for 5 ng of Pb deposited on the graphite co-axial rod (——) and tungsten co-axial rod (- - -); and background (· · ·). 97

4.9. Temporal response of the Pb atomic emission signal at an RF power of 20 W for 5 ng of Pb deposited on the furnace wall (——) and RF electrode (- - -), 0.5 ng of Pb deposited on the furnace wall (-·-·-, × 10); and background at 20 W (· · ·). 100

4.10. Atomic absorbance for 5 ng of Pb deposited on the furnace wall as a function of RF power: for 1 - 5 (●), and 1 - 3 s (■). 101

4.11. Temporal response of the Pb atomic emission signal for 5 ng of Pb deposited on the furnace wall at an RF power of 14 (——), 20 (- - -), 30 (- · - · -), and 40 W (— — —); and background at 20 W (· · ·). 105

4.12. Temporal response of the Pb signal for 5 ng of Pb deposited on the furnace wall at an RF power of 40 W: emission (——) and absorption (- - -). 106

4.13. Temporal response of the Mn atomic absorption signal at an RF power of 0 W for 1.25 ng of Mn deposited on the furnace wall with (- - -), and without (——) the co-axial rod; and background (· · ·). 108

4.14. Temporal response of the Mn atomic absorption signal at an RF power of 0 W for 1.25 ng of Mn deposited on the graphite co-axial rod (——), tungsten co-axial rod (- - -); and background (· · ·). 109

FIGURES PAGE

4.15. Temporal response of the Mn atomic emission signal at an RF power of 20 W for 1.25 ng of Mn deposited on the furnace wall (——) and RF electrode (- - -); and background at 20 W (· · ·). 111

4.16. Temporal response of the Mn atomic emission signal for 1.25 ng of Mn deposited on the furnace wall at an RF power of 14 (——), 20 (- - -), 30 (- · - · -), and 40 W (— — —); and background at 20 W (. . .). 113

4.17. Atomic absorbance for 1.25 ng of Mn deposited on the furnace wall as a function of RF power: for 2.8 - 5.5 (●), and 3.5 - 5.5 s (■). 114

4.18. Temporal response of the Mn signal for 1.25 ng of Mn deposited on the furnace wall at an RF power of 40 W: emission (——) and absorption (- - -). 115

5.1. Time-resolved Pb-excitation temperature (——) at an RF power of 50 W and the corresponding graphite furnace temperature (- - -) during the atomization step of Pb. 125

5.2. Effect of the RF power on the net emission intensity of Pb (●) and on the Boltzmann factor (- - -). 129

5.3. Temporal response of the Pb emission signal at an RF power of 20 W for 0.5 ng of Pb (——); background (- - -). 134

5.4. Lead signal-to-noise ratio (SNR) as a function of signal intensity. 138

5.5. Effect of RF power on the signal-to-noise ratio (SNR: ●) and the signal-to-background ratio (SBR: ■) for Pb. 139

5.6. Effect of RF power on the net background emission (●) and the relative standard deviation of the background (RSDB: ○). 140

5.7. Effect of the spectral bandwidth on the background emission intensity at 283.3 nm; 20 W (●), 40 W (■). 141

FIGURES PAGE

5.8. The analyte calibration graph for Pb. 144

5.9. Effect of integration time on the sensitivity of the Pb emission intensity. The values in the parentheses give the correlation coefficient of the least square fit for each calibration graph. 145

5.10. Effect of integration time on the detection limit (DL) for Pb. 146

6.1. Temporal response of the reflected power at an RF power of 20 W for the deposition of distilled water (——), and 160 ng of Na as NaCl in distilled water (· · ·); and the temperature profile of the graphite furnace (- - -). 157

6.2. Temporal response of the Na emission signal at an RF power of 20 W for the deposition of 160 ng of Na as NaCl (——), and 160 ng of Na as $NaNO_3$ (- - -); and water blank (· · ·). 159

6.3. Temporal response of the Pb emission signal at an RF power of 20 W for the deposition of 0.5 ng of Pb (——), 0.5 ng of Pb and 160 ng of Na as NaCl (- - -), and 0.5 ng of Pb and 160 ng of Na as $NaNO_3$ (— —). 163

6.4. Interference effect of 160 ng of Na as NaCl (●) and 160 ng of Na as $NaNO_3$ (■) on the Pb emission intensity as a function of RF power. 169

6.5. Temporal response of the Pb emission signal at an RF power of 14 W for 0.5 ng of Pb (——) and 0.5 ng of Pb and 160 ng of Na as NaCl (- - -). 170

6.6. Interference effect on the Pb emission intensity at an RF power of 20 W as a function of amount of Na as NaCl. 171

6.7. Temporal response of the Ag emission signal at an RF power of 20 W for 0.25 ng of Ag (——), 0.25 ng of Ag and 160 ng of Na as NaCl (- - -), and 0.25 ng of Ag and 160 ng of Na as $NaNO_3$ (· · ·). 173

FIGURES PAGE

6.8. Interference effect of 160 ng of Na as NaCl (●) and 160 ng of Na as $NaNO_3$ (■) on the Ag emission intensity as a function of RF power. 175

6.9. Interference effect on the Ag emission intensity at an RF power of 20 W as a function of amount of Na as NaCl. 176

6.10. Interference effect on the Ag emission intensity at an RF power of 20 W as a function of amount of Na as NaCl in 1 % HNO_3 (○), and Na as $NaNO_3$ (●). 177

6.11. Temporal response of the Pb emission signal at an RF power of 20 W for 0.5 ng of Pb (——), 0.5 ng of Pb in 0.25 % (w/v) ascorbic acid (- - -), and 0.5 ng of Pb in 1.5 % (w/v) ascorbic acid (— —). 180

6.12. Interference effect on the Pb emission intensity at an RF power of 20 W as a function of concentration of ascorbic acid. 181

6.13. Temporal response of the Ag emission signal for the deposition of 0.25 ng of Ag (——), 0.25 ng of Ag in 0.25 % (w/v) ascorbic acid (- - -), and 0.25 ng of Pb in 1.5 % (w/v) ascorbic acid (—· —) at an RF power of 20 W. 183

6.14. Temporal response of the Pb emission signal for 0.5 ng of Pb (——), 0.5 ng of Pb in 2.5 % (v/v) phosphoric acid (— — —), 2.5 % (v/v) phosphoric acid blank (- - -), and water blank (· · ·) at an RF power of 20 W. 184

List of Abbreviations

AAS	atomic absorption spectrometry
ADC	analog-to-digital converter
AES	atomic emission spectrometry
APF-CCP	atmospheric pressure furnace capacitively coupled plasma
CFAES	carbon furnace atomic emission spectrometry
CRA	carbon rod atomizer
d. c.	direct current
DL	detection limit
EIE	easily ionizable element
FANES	furnace atomization non-thermal excitation spectrometry
FAPES	furnace atomization plasma excitation spectrometry
GF	graphite furnace
GFAAS	graphite furnace atomic absorption spectrometry
HA	hollow-anode
HC	hollow cathode
HCL	hollow cathode lamp
HGA	heated graphite atomizer
ICC	integrated contact cuvette
ICP	inductively coupled plasma
ICP-OES	inductively coupled plasma optical emission spectrometry
IP	ionization potential
ISM	industrial, scientific, and medical

LTE	local thermal equilibrium
LPDA	linear photodiode array
MS	mass spectrometric
NRC	national research council
PMT	photomultiplier tube
RF	radio frequency
RSD	relative standard deviation
RSDB	relative standard deviation of the background
S	sensitivity
SBR	signal-to-background ratio
SDB	standard deviation of the background
SNR	signal-to-noise ratio
SQRT	square root
STPF	stabilized temperature platform
TE	thermal equilibrium
v/v	volume-to-volume ratio
w/v	weight-to-volume ratio
σ_{bl}	standard deviation of the background

ACKNOWLEDGEMENTS

I would like to express my sincere appreciation to my research supervisor, Dr. M. W. Blades, for his guidance and encouragement throughout the course of this project.

I wish to thank members of my guidance committee, Dr. W. R. Cullen, Dr. L. Burtnick and Dr. D. Dolphin for their valuable suggestions.

I thank Dr. K. Orians for lending a sodium hollow cathode lamp, which was used in the interference studies. I would like to extend my thanks to Mr. M. Vagg in the Mechanical Services Shop of the Chemistry Department for constructing the FAPES source and for his prompt help. Thanks also go to Mr. M. Carlisle of the Electronics Shop for technical assistance.

Finally, I would like to thank my wife for her patience and encouragement during the past few years.

CHAPTER 1

INTRODUCTION

Advancements in many areas of analytical chemistry are driven by environmental needs, made possible by technological development, and based on progress in fundamental scientific understanding. Analytical atomic spectroscopy is one branch of analytical chemistry, wherein the analytical spectroscopist develops, improves, and characterizes spectrochemical sources. The "characterization studies" in analytical atomic spectroscopy reflect the need for solving problems in chemical measurement in atomic spectrometry.

The primary objective of the work described in this thesis is to characterize the radio frequency (RF) helium plasma source at 13.56 MHz in FURNACE ATOMIZATION PLASMA EMISSION SPECTROMETRY (FAPES) as a spectrochemical source for elemental analysis. As compared with "The Seven Ages of an Analytical Method" described in H. A. Laitinen's editorial in *Analytical Chemistry* [1], this new spectrochemical method, FAPES, has undergone the first two ages, *i.e.*, "conception" and "experimental measurement". The third and fourth stages described in this thesis are the "development of instrumentation" and "characterization". Yet to come are the fifth stage, "applications", the sixth stage, "establishment of procedures" and the seventh stage, "recognition as an accepted method".

The discussion that follows in this chapter is devoted to an introduction to FAPES and some special topics related to the work described in this thesis. The last section of this chapter presents the scope of the thesis.

1.1 FAPES: Historical Development

Australian physicist Alan Walsh's classic publication on Atomic Absorption Spectrometry (AAS), describing flame AAS [2], revolutionized atomic spectrometric methods. During the 1970s, flame AAS became the most widely employed spectrometric method for the determination of metallic elements. Even today, flame AAS is a useful method for a variety of analyses. Although flame AAS has interferences, these interferences can be easily controlled. But, refractory oxides, for example, those of B, V, Ta, and W, are only partially dissociated in the flame, and therefore, are difficult to analyze by employing flame AAS. Since the introduction of the nitrous oxide-acetylene flame in 1966 [3], there have been no major advances in the flame method, which appears to have reached a plateau of development.

Graphite Furnace Atomic Absorption Spectrometry (GFAAS), first described three decades ago by Boris L'vov [4], appears to be the most sensitive atomic spectrometric method for the determination of trace metals. Unlike the flame AAS method, wherein Walsh employed continuous nebulization of the sample into the flame to provide a steady state absorption signal, L'vov converted a very small sample volume to an atomic vapor inside

a resistance-heated graphite furnace. This graphite furnace method yields the best detection limits for absolute amounts and very few techniques can successfully compete with those detection levels [5]. However, AAS is well recognized as a "single element at a time" technique(1).

In GFAAS, 1 to 100 μL of aqueous sample is deposited onto the inner furnace wall, dried, and then vaporized into a furnace volume of less than 1 cm^3, to create a highly concentrated atom cloud. The analyte transport efficiency into the observation volume is close to 100 %, compared with 1 to 5 % for other conventional sources (flame or ICP). Furthermore, the residence times of analyte atoms in the observation volume are about two orders of magnitude higher than those found in other sources. Consequently, analyte densities in the observation volume are several orders of magnitude higher in the furnace methods, resulting in higher sensitivities, and hence, lower detection limits. The graphite furnace also facilitates matrix modification in situ, because chemical and thermal pre-treatment of the sample can be incorporated into the heating program.

Several kinds of plasma spectrometric methods have been employed in emission spectrometry [6], but the most prevalent is the Inductively Coupled Plasma Optical Emission Spectrometry (ICP-OES) described by

---

(1) Some commercial instruments are now available with limited multi-elemental capability. Smith-Hieftje 8000 flame furnace AA (Thermo Jarrel Ash, Franklin, Massachusetts, USA) is configured with eight hollow cathode lamps that permit the operator to determine eight elements without changing hollow cathode lamps, and to perform determinations up to four at a time.

Greenfield *et al.* in 1964 [7], and Wendt and Fassel in 1965 [8]. Unlike the AAS method, emission spectrometric methods such as ICPs are inherently multi-elemental techniques. Inductively coupled plasma is also relatively free from interferences, and those refractory oxides only partially dissociated in the flame are completely dissociated at high ICP temperatures. However, on a concentration basis, ICP detection limits are 10 to 100 times higher and on an absolute basis, 1000 times higher than GFAAS [5].

Because of the low detection limits in GFAAS, the graphite furnace has been employed as an atomization source for emission spectrometric methods which are capable of simultaneous, multi-elemental analysis(2). Ottaway and Shaw employed the high temperature produced during the atomization step of the analyte in a graphite furnace to thermally excite the analyte atoms [10]. This method, Carbon Furnace Atomic Emission Spectrometry (CFAES), is limited by the energy available for thermal excitation. For elements having resonance wavelengths below 300 nm, the detection limits are much poorer than those for GFAAS [10]. Furthermore, at temperatures above 2500 K, the intense emission from the furnace wall is a major spectral interference in the visible region [11].

---

(2) The graphite furnace is an atomization source, not only for emission spectrometric methods but also for mass spectrometric (MS) methods, such as GF-ICP-MS, with femto gram level detection limits [9]. However, a discussion about such methods is beyond the scope of this thesis.

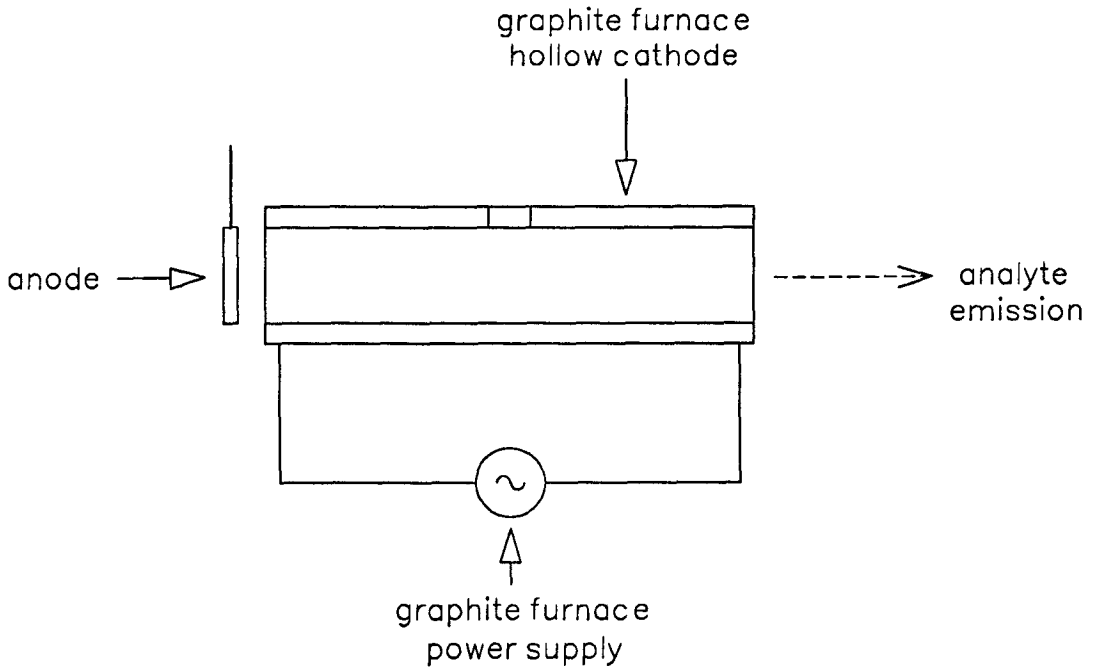

Figure 1.1. Schematic diagram of the FANES source. (Adapted from H. Falk, E. Hoffmann, and Ch. Ludke, *Spectrochim. Acta*, 283, 39B (1984), with permission of Pergamon Journal Inc.)

Falk *et al.* reported a low pressure, direct current (d. c.) glow discharge sustained inside a graphite furnace, with the furnace employed as a Hollow Cathode (HC), and a point or ring external to the furnace as the anode [12,13]. This spectrometric method has been designated Furnace Atomization Non-thermal Excitation Spectrometry (FANES), or HC-FANES. Figure 1.1 depicts a schematic diagram of the FANES source. The furnace was a Massmann-type (Section 1.3.2), and was graphite or pyrolytic-graphite coated. The sample was introduced by depositing a μL volume onto the inner wall of the graphite furnace, and vaporized into the discharge during the high temperature atomization step of the analyte. The

analyte atoms are excited while inside the discharge and emit characteristic line spectra that can be used for simultaneous multi-elemental analysis. Detection limits of the FANES determinations are comparable to those of GFAAS. Because of the low pressure requirement of the glow discharge operation, sample introduction is somewhat laborious and time consuming.

Ballou *et al.* also employed a d. c. glow discharge [14], which was conceptually similar to the FANES source. Figure 1.2 illustrates a schematic diagram of the HA-FANES source. In this source, the graphite furnace was employed as a Hollow Anode (HA), and a graphite rod, which was oriented co-axially with the furnace and extended the entire furnace length, acted as the cathode. The graphite furnace was an integrated contact cuvette (Section 1.3.3.2) and the axial electrode was a pyrolytic-graphite coated rod. Analytical figures of merit for HA-FANES are not much known. The operation of this source is similar to that of FANES and requires low pressures.

Liang and Blades first reported an atmospheric pressure plasma source inside the graphite furnace for analyte excitation [15]. This plasma source had the same geometry as that of HA-FANES, but was operated with an RF power source. The spectrometric method with such an RF plasma source has been designated Furnace Atomization Plasma Excitation Spectrometry (FAPES) [16,17]. Compared with the low pressure operation, the atmospheric pressure operation was expected to offer convenient sample introduction and increased residence time of analyte atoms within the

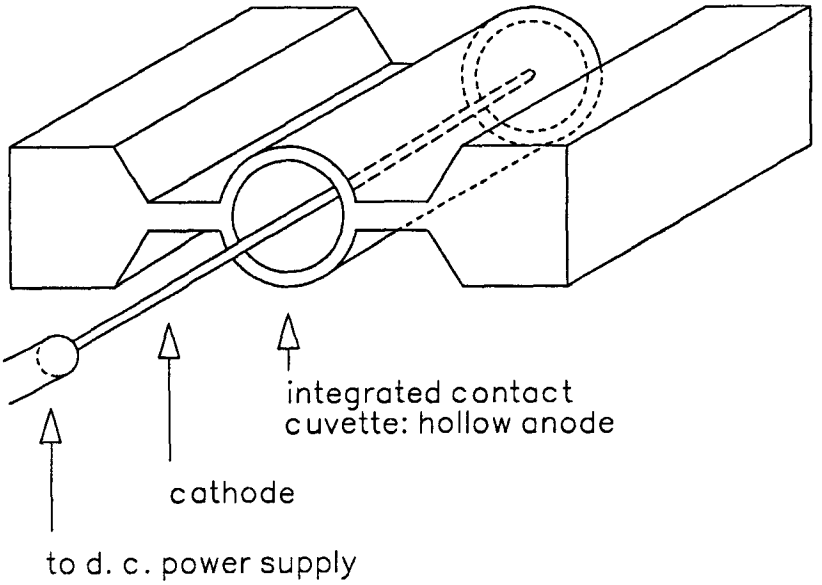

Figure 1.2. Schematic diagram of the HA-FANES source. (Adapted from N. E. Ballou, D. L. Styris, and J. M. Harnly, *J. Anal. At. Spectrom.*, 1141, 3 (1988), with permission of The Royal Society of Chemistry.)

graphite furnace [15]. A more detailed description of FAPES is presented in the next section.

As stated previously, the development of new spectrochemical methods stem from the need for determining ultra-trace concentrations of analytes in various samples. During the last two to three decades, improvements in detection limits, use of small sample volumes, and fast analysis have been achieved [18]. Detection limits have gone from microgram to sub-picogram levels or even single atom detection, and sample size has gone from milliliters to microliter volumes [19]. With the variety of analytical methods available

today, no method is really rendered obsolete by another. There is no "best" method; the choice depends on one's skills and on the nature of the chemical measurement.

The historical development [20,21] and the general status [5,22-24] of GFAAS has been reviewed elsewhere. Comprehensive reviews of the historical development of various plasma sources [6], development of ICP [25], graphite furnaces for sample introduction in plasma source spectrometry [26], GF-ICP-OES methods [27], and ICP-mass spectrometric methods [28-30] are available. Recently, a graphite furnace has also been employed as a sample introduction method for d. c. arc plasmas [31-33].

1.2 Furnace Atomization Plasma Excitation Spectrometry

Figure 1.3 illustrates a schematic diagram of the RF plasma source described by Liang and Blades [15]. This plasma source consists of a conventional Massmann-type graphite furnace work-head (Instrumentation Laboratory, model IL 455) and a co-axial thoriated-tungsten RF electrode. The rear optical window (through which light from the hollow cathode lamp was normally directed) of the furnace work-head was removed and replaced with the RF electrode. The operating frequency was 27 MHz and the RF power delivered to the plasma was about 20 W. Helium was used as the plasma gas of this atmospheric pressure RF plasma. Liang and Blades suggested that the mode of power coupling to the plasma was primarily capacitive in

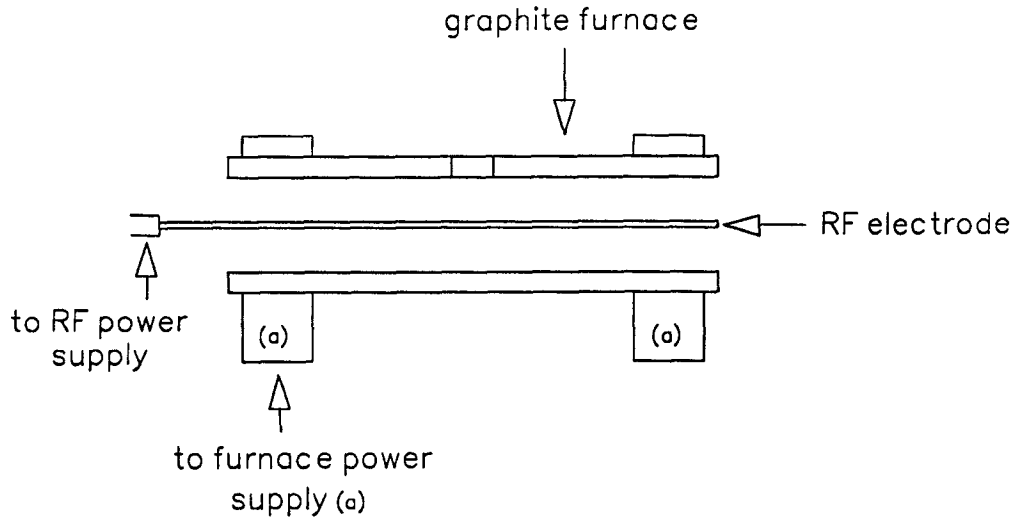

Figure 1.3. Schematic diagram of the FAPES source. (Adapted from D. C. Liang and M. W. Blades, *Spectrochim. Acta*, 1049, 44B (1989), with permission of Pergamon Journal Inc.)

nature [15]. Liang and Blades designated this plasma source as Atmospheric Pressure Furnace Capacitively Coupled Plasma (APF-CCP). However, this plasma source is now recognized as a FAPES source in the literature [34].

The analyte sample was a small brass chip about 5 mg. Some emission spectra of Cu and Zn were recorded when the furnace was heated to about 800 ^{o}C. Liang and Blades suggested that at low RF powers, the dominant sample introduction mechanism to the plasma was RF sputtering [15]. A relatively high gas temperature and, as a consequence,

a reduction in gas-phase chemical interferences compared with GFAAS, were expected within the graphite furnace with the plasma.

In a follow up study, Smith *et al.* determined the analytical figures of merit for Ag [17]. For Ag, the absolute detection limit was 0.3 pg and the linear dynamic range was 2-orders of magnitude. Smith *et al.* also reported a decrease of 20 % and 50 % in the Ag emission intensity when 2.3 μg of Na is present as NaCl and $NaNO_3$, respectively.

Sturgeon *et al.* employed a Perkin-Elmer furnace work-head (model HGA-2200) with a co-axial graphite electrode [16]. The power delivered to the helium plasma was about 50 to 70 W. A 10 μL aliquot of test solution, Cd or Mn, was deposited on the furnace wall and subjected to the atomization step as in GFAAS. The plasma background emission and transient emission signals for Cd and Mn were given. The detection limits for Cd and Mn were 36 pg and 52 pg, respectively.

In the next section, the analyte atomization within the graphite furnace is discussed. The various graphite furnace designs along with the role of the graphite furnace for analyte atomization and vaporization are presented.

1.3 Analyte Atomization: The Graphite Furnace

The graphite furnace is a resistance-heated cylindrical device. Liquid samples can be deposited onto the inner furnace wall by means of a micro-pipette through a hole in the furnace. To prevent the oxidation of graphite at high temperatures, the furnace is coated with a thin layer of pyrolytic-graphite and purged with an inert gas.

The sample is placed on the furnace wall (wall atomization) or on a separate device inserted into the furnace (platform atomization, Section 1.3.3.1). In the case of platform atomization, the platform is primarily heated by the radiation from the furnace wall. The sample on the furnace wall (or on the platform) can be subjected to thermal treatment. Generally, there are two thermal treatment stages: drying and ashing. During the drying stage, solvent is evaporated. During the ashing stage, any organic residues in the sample are removed by decomposition and vaporization. The next stage is the vaporization and atomization (or simply: atomization) stage, during which the analyte and the remainder of the sample form a vapor cloud inside the furnace. During the atomization step, the temperature of the furnace (atomization temperature) can reach a maximum as high as 3200 K.

In the next section, some graphite furnace designs are presented. A more detailed discussion about graphite furnaces in AAS is available elsewhere [35-39].

1.3.1 L'vov Furnace

The first successful non-flame atomizer in the form of a carbon-rod electrode and a graphite furnace was described by L'vov [4,40]. The L'vov furnace has now been widely described in the GFAAS literature, and is depicted in Figure 1.4. The graphite furnace was 30 to 50 mm long, with an inner diameter of 2.5 to 5 mm. The furnace was heated up to about 2700 K.

The sample was introduced into the furnace on a carbon-rod electrode of 6 mm diameter. The head of the electrode was shaped to fit the orifice in the wall of the graphite furnace. The graphite furnace was heated for 20 to 30 s and the electrode was moved into the orifice of the graphite furnace. The auxiliary electrical heating of the electrode was turned on for 2 to 3 s, and the atomic absorption was measured. The electrode was then lowered away from the graphite furnace, and the system was ready for the introduction of another electrode carrying a sample. Because the atomic vapor can penetrate the walls of the furnace, the inner wall was lined with a thin layer of pyrolytic-graphite, Ta or W foil.

In the original form of the L'vov furnace, vaporization of the sample was achieved by a d. c. arc formed between the carbon-rod electrode and an auxiliary electrode mounted under the furnace [4]. To eliminate the furnace background, light from the hollow cathode lamp was modulated. L'vov also employed two-channels that permit simultaneous recording of absorption for two elements, one of which can be an internal standard [40].

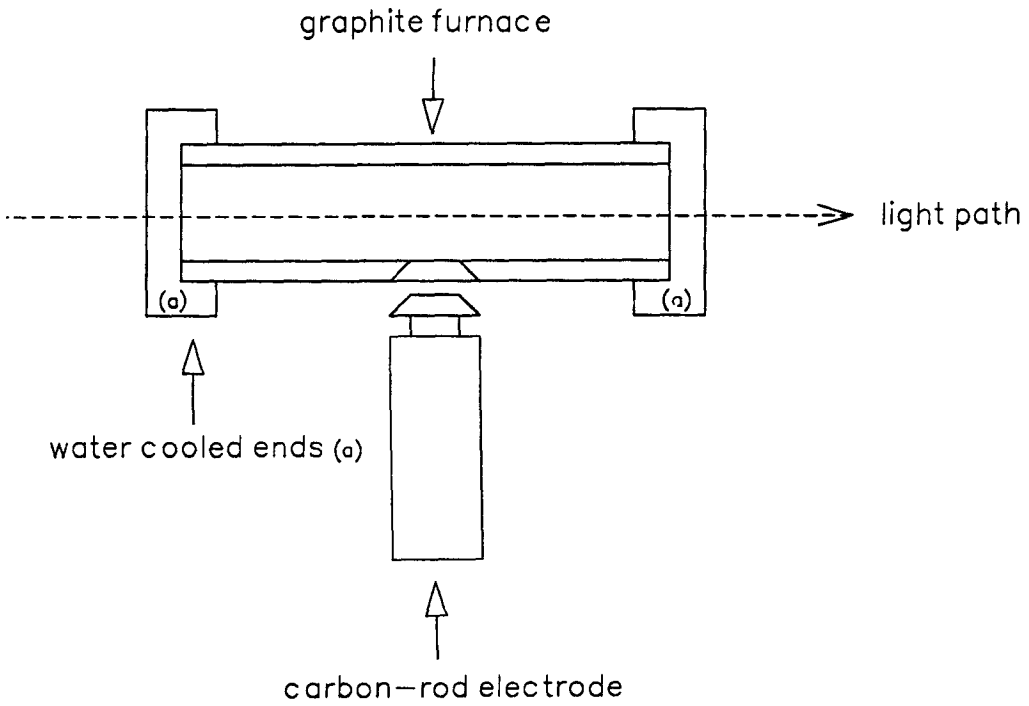

Figure 1.4. Schematic diagram of the L'vov graphite furnace and electrode assembly. (Adapted from B. V. L'vov, *Spectrochim. Acta*, 53, 24B (1969), with permission of Pergamon Journal Inc.)

1.3.2 Massmann Furnace

The Massmann furnace [41], a simplified version of the L'vov graphite furnace, is depicted in Figure 1.5. The Massmann furnace was 55 mm long, 6.5 mm in internal diameter, and had a wall thickness of 1.5 mm. The electrical contacts were made at both ends of the furnace. Unlike the L'vov method, liquid samples were deposited onto the inner furnace wall through a small hole in the center of the furnace by means of a micro-pipette, while solid samples were inserted from one side of the furnace. Sample volumes of 5 to 200 μL were used. The temperature of the furnace reached 2900 K

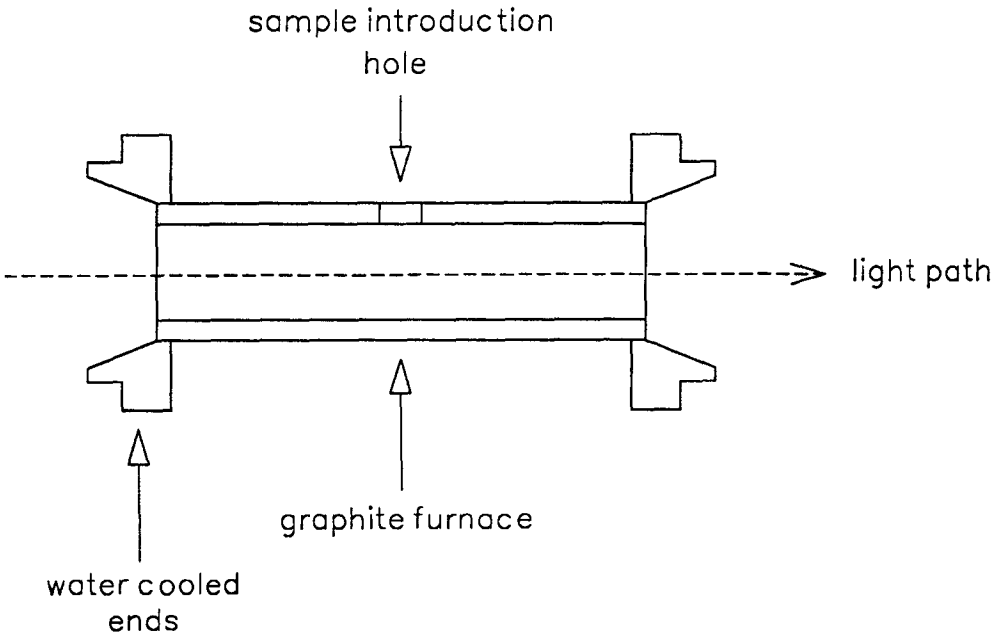

Figure 1.5. Schematic diagram of the Massmann graphite furnace. (Adapted from H. Massmann, *Spectrochim. Acta*, 215, 23B (1968), with permission of Pergamon Journal Inc.)

within a few seconds. The furnace was enclosed in a chamber and purged with Ar.

The Massmann graphite furnace has been further developed for commercial AAS instruments. Almost all the research work carried out in GFAAS during the last three decades employed two commercial graphite furnaces, namely, Perkin-Elmer model, Heated Graphite Atomizer (HGA) and Varian Techtron model, Carbon Rod Atomizer (CRA). The HGA is similar to the Massmann-type furnace. The CRA is a 1.5 mm diameter rod with a transverse hole of 1.5 mm in diameter. The CRA is supported by two

graphite electrodes, which are mounted on water cooled terminal blocks and connected to the furnace power supply. Recent models of the Varian spectrometers contain Massmann-type furnaces. A more detailed description of these commercial graphite furnaces is available in reference [39].

1.3.3 Limitations of Massmann-type Furnaces

Some fundamental limitations are inherent in the Massmann-type furnaces. Temporal non-isothermality and spatial non-isothermality are two of the major limitations [42]. Temporal non-isothermality occurs when analyte atoms appear in the observation volume during a time in which the temperature of the gas-phase is low and is rapidly changing to the atomization temperature. The temperature range within which analyte atoms persist in the furnace, and hence, the residence time of analyte atoms, is dependent on the nature of the analyte and the accompanying matrix [43]. As a result, the degree of atomization is often low and matrix dependent [43,44]. In addition, temperature dependent kinetic effects on the atomization of the analyte cannot be eliminated [43].

Spatial non-isothermality is the non-uniform temperature distribution along the furnace length and is caused by the heating characteristics of the water cooled ends of the furnace. This non-uniformity results in vapor condensation on the cooler end-regions of the furnace, causing memory effects [43]. In addition, recombination of the sample vapor leaving the furnace through the cooler end-regions is a major contribution to spectral

interferences: molecular absorption and light scattering, in AAS [40]. Spatial non-isothermality of the furnace also has a severe effect in CFAES due to self-absorption [45].

1.3.3.1 L'vov Platform

L'vov first employed a graphite platform installed inside the furnace, from which the sample was vaporized rather than from the furnace wall [43]. The graphite platform is sometimes called the "L'vov platform" or the "Stabilized Temperature Platform" (STPF) [44,46]. A schematic diagram of the L'vov platform is provided in Figure 1.6.

The platform slides into the furnace operated in the usual manner, except longer thermal treatment times are necessary. The platform is heated primarily by furnace radiation during the heating cycle of the furnace, and hence, the temperature of the platform lags compared with that of the furnace wall. Therefore, analyte vaporization and atomization are delayed until the gas-phase temperature within the furnace reaches the atomization temperature. In addition, due to the temperature difference between the furnace wall and the platform, a higher heating rate for the platform is achieved in the initial stages of the atomization step [43].

A more detailed discussion on theoretical and experimental studies on the platforms for GFAAS has been published by Wu *et al.* [47].

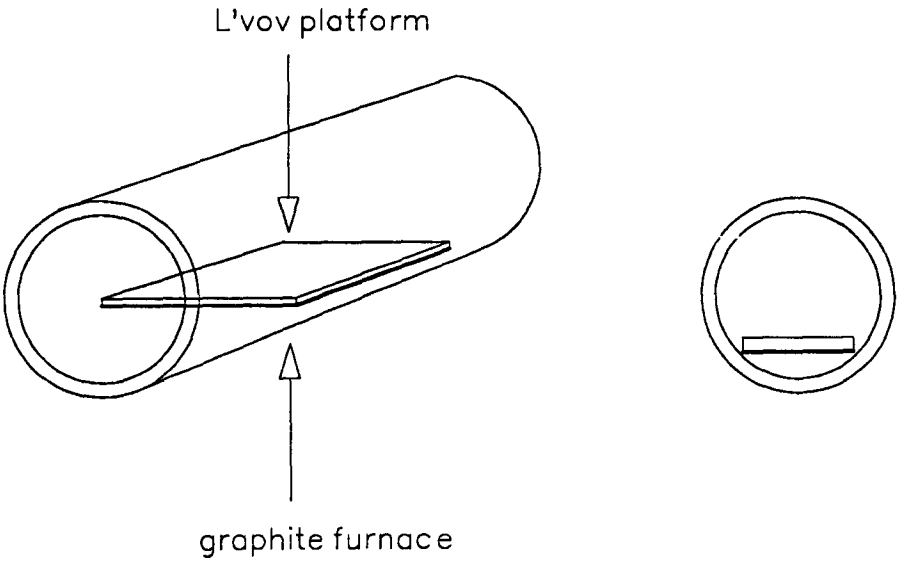

Figure 1.6. Schematic representation of the L'vov platform inside the graphite furnace.

1.3.3.2 Integrated Contact Cuvette

When a L'vov platform is used with conventional end-heated Massmann-type furnaces, temporal isothermality can be achieved. However, spatial non-isothermality of the furnace is not overcome. Spatial non-isothermality can be eliminated by employing a side-heated Integrated Contact Cuvette (ICC) [48]. In the ICC, the full length of the furnace starts to heat at the same time (transverse heating), and therefore, achieves spatial isothermality. It should be noted here that both the ICC and a platform should be employed to achieve spatial and temporal isothermality. The ICC

is the furnace type used for most of the work described in this thesis. A schematic diagram of the ICC is available in Figure 1.2.

1.3.4 Atomization Mechanisms

Atomization mechanisms are dependent on the nature of the analyte and the accompanying matrix, and are very complex in nature. Many studies on atomization mechanisms have been reported in the literature and various proposed mechanisms have been subjected to considerable debate over the years. Reference to these studies will be given, when appropriate, in Chapter 4 of this thesis. For an introduction to atomization mechanisms, the following discussion is warranted.

When the analyte sample is in a nitric acid solution, oxide of the analyte is formed from the nitrate during the ashing step or the atomization step.

Mechanism I. Reduction of Oxide by Carbon

$$MO_{(s)} \xrightarrow[\text{Reduction}]{\text{Carbon}} \begin{matrix} M_{(s,l)} \\ CO_{(g)} \end{matrix} \xrightarrow{\text{Vaporization}} M_{(g)}$$

In this process, analyte oxide is reduced by carbon in the furnace wall to form analyte atoms either in solid or liquid form, which are then vaporized to the gas-phase.

Mechanism II. Thermal Dissociation

$$MO_{(s)} \xrightarrow[\text{Dissociation}]{\text{Thermal}} M_{(s,l)} + 1/2O_2 \xrightarrow{\text{Vaporization}} M_{(g)}$$

In this mechanism, analyte oxide thermally dissociates on the furnace wall. The thermal dissociation follows the gas-phase appearance of the analyte atoms.

Mechanism III. Dissociation of Oxide Vapor

$$MO_{(s)} \xrightarrow{\text{Vaporization}} MO_{(g)} \xrightarrow[\text{Dissociation}]{\text{Thermal}} M_{(g)} + 1/2O_2$$

According to this mechanism, analyte oxide vaporizes from the furnace wall before dissociating in the gas-phase. The gas-phase dissociation equilibrium of the analyte may be affected by the amount of oxygen which, in turn, is determined by the amount of CO in the gas-phase (Sections 4.3.2 and 6.3.5).

Mechanism IV. Dissociation of Halide Vapor

$$MX_{(s)} \xrightarrow{\text{Vaporization}} MX_{(g)} \xrightarrow[\text{Dissociation}]{\text{Thermal}} M_{(g)} + X_{(g)}$$

Dissociation (or formation) of analyte halides in the gas-phase is important, especially when a chloride matrix is present in the sample.

The next section describes the analyte excitation in the plasma. Some characteristics of RF discharges at atmospheric pressure along with the excitation mechanisms of the analyte will be presented.

1.4 Analyte Excitation: The Plasma

Unlike low pressure RF gas discharges, atmospheric pressure capacitively coupled gas discharges appear to find no applications in plasma processing techniques. Therefore, these RF plasmas are rarely reported in the literature. However, the high frequency discharges at atmospheric pressure have been studied in a few occasions as discharges in the circuit breakers in high frequency power generators [49,50]. Some fundamental characteristics of RF (mainly 1 - 25 MHz) gas discharges at atmospheric pressure have been reported [51-54].

Recently, RF discharges at low pressure have been employed in mass spectrometry [55], and emission spectrometry [56]. Those interested in a detailed discussion on low pressure discharges (both d. c. and RF) may refer to Chapman [57]. Only a brief description leading to the nature of the RF discharge at atmospheric pressure is given in the next section.

1.4.1 The RF Discharge at Atmospheric Pressure

For the simplicity of the discussion, first consider two electrodes of equal area, at a certain distance apart at low pressure. When a sufficient d. c. voltage is applied, a discharge strikes between the electrodes. In this discharge, a cathode dark space and a glow space can be seen. A cathode fall of potential develops across the dark space, leaving the glow space nearly field free. For self-sustainment (current continuity) of the discharge, a steady state electron concentration must be maintained. In a d. c. glow discharge, this electron concentration is mainly caused by secondary emission through positive ion bombardment on the cathode.

If, instead of a d. c. voltage, a low frequency alternating voltage is applied, it can be observed that the discharge behaves as though it has two alternating cathodes. This system is a succession of short-lived d. c. discharges, because at low frequencies, there is ample time for the discharge to become fully extinguished. The discharge is extinguished when the cathode potential drops below the discharge sustain value because of the build up of a self-bias d. c. potential on the cathode.

The nature of the d. c. potential on the cathode of d. c. and alternating current discharges should be noted. In the case of a d. c. discharge, the potential at the cathode is equal to the applied potential difference between the two electrodes. In contrast, in an alternating current discharge, the d. c. potential at the electrodes is a self-bias voltage. This self-bias voltage arises because the electrons have much higher mobility than the heavier ions and so

are easily collected on an electrode whenever it becomes positive with respect to the glow space [58].

If the frequency of the applied voltage is increased, it is observed that the minimum pressure at which the discharge operates is reduced [59]. This reduction indicates that there is an additional source of ionization other than the secondary electron emission from the electrodes. This additional source of electrons arises when electrons, oscillating in the time dependent electric field, undergo collisions with the plasma gas atoms to cause ionization. Therefore, the high voltage electrode that is necessary in a d. c. glow discharge for the secondary electron emission is not required to sustain the RF discharge [60]. Furthermore, the cathode glow attached to each electrode is the same as in the d. c. case. The human eye cannot follow quick intensity changes and "sees" that the cathode glow is attached to both the electrodes. However, the cathode glow changes its position and is attached only to the electrode that acts as the cathode in any particular half-cycle [52].

In addition to the frequency of the discharge, the pressure is also an important parameter that affects the discharge characteristics. The pressure affects the discharge characteristics in two ways. Firstly, in a low pressure discharge, the mean free path of the electrons and ions is high. The electric field in the cathode dark space causes the acceleration of positive ions through the dark space toward the cathode. These accelerated positive ions impinge on the cathode, and cause the sputtering of the electrode material and the emission of secondary electrons. However, at atmospheric pressure,

the mean free path of the ions is short, and therefore, ions can be considered as stationary. Secondly, the high pressure discharge is essentially a low current glow discharge. Transition from glow to arc discharge can be produced by an increase in current under constant pressure (or by an increase in pressure at constant current), and a considerable fall in the discharge voltage, which is associated with a change in the electron emission mechanism from the cathode [61]. In the case of arc, electron emission from the cathode is mainly thermionic and field emission.

In atmospheric pressure discharges, a positive space-charge region is built up in front of the appropriate electrode in each negative half-cycle. At frequencies above 1 MHz, the length of this space-charge region does not exceed 5×10^{-3} cm (in air), neither does the mean free path of an ion [51]. Voltage of the RF discharge depends on the nature and the distance between the electrodes, and is 300 V or higher, and carries less than 1 A of current [54]. The time scale of the application of the RF voltage is such that frequencies in the order of 1 MHz and above resulting in a pseudo-continuous plasma. The reignition voltage in each half cycle is dependent on the electrode distance. It has also been shown that reignition voltage drops at a certain electrode distance [53]. This observed drop in the reignition voltage was attributed to the residual charge carriers at higher electrode distances and was not due to the space charge effect [53].

If the current density increases, an RF arc discharge with a brighter appearance than a glow can be observed [54]. An arc does not usually

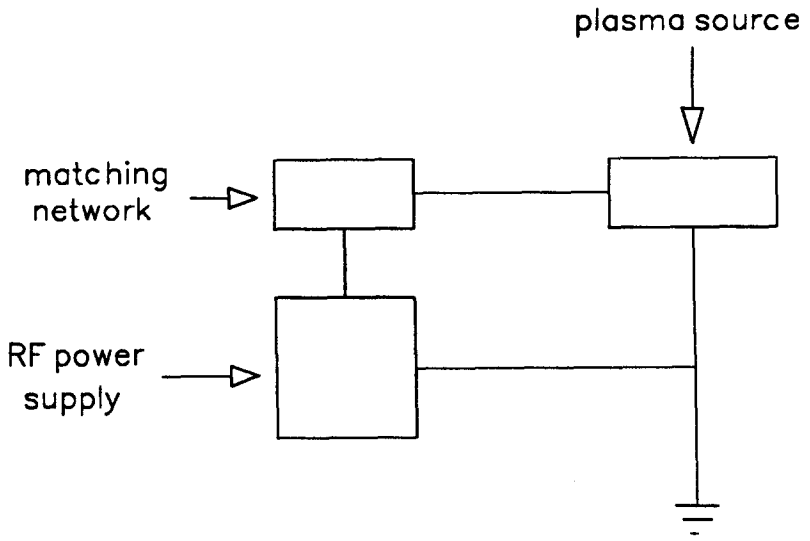

Figure 1.7. Schematic diagram of an RF discharge system.

maintain a stable position, but moves around on the electrode surface. The RF glow can turn temporary into an arc at any time. The transition to the arc is also favoured by conditions that facilitate electron emission, such as rough electrode surface and salt deposits [54].

Figure 1.7 depicts the main components of an RF discharge system. It consists of an RF power supply, a matching network, and the discharge. The RF power supply can be operated at the frequencies permitted by the United States Federal Communications Commission for industrial, scientific, and medical (ISM) equipments [62]. The purpose of the matching network is to

maximize the RF power coupled to the plasma and to protect the RF power supply.

1.4.2 The RF Discharge in FAPES

The atmospheric pressure RF plasma source within the graphite furnace has a bright region surrounding the RF electrode and a less intense plasma fills the remainder of the graphite furnace volume. It is also observed that when the RF power coupled to the plasma is increased, the bright region surrounding the electrode extends along the RF electrode beyond the length of graphite furnace. The appearance of the extended RF glow along the RF electrode marks the onset of arcing between the RF electrode and the furnace wall. This RF discharge inside the graphite furnace is not yet well-understood. The voltage-current characteristics are not known and a mathematical model describing the discharge has not been developed.

The atomic spectrometric utility of the RF discharge at atmospheric pressure should be noted. Firstly, the gas discharge inside the graphite furnace has been used only for analyte excitation process. Analyte introduction into the excitation volume is achieved during the high temperature atomization step of the analyte. Secondly, the discharge contains unequal electrode areas causing different current densities and electric field strengths on each electrode during each half-cycle. Therefore, this plasma source is not radially symmetrical along the furnace length. Finally, the discharge contains hot electrodes with varying temperatures up

to about 3000 K depending on the experimental conditions. However, depending on the RF power and the furnace temperature, the RF plasma appears to change into an RF arc with the evolution of the thermionic electrons.

1.4.3 Excitation Mechanisms

Although it is beyond the scope of this thesis to go into details of various excitation mechanisms in plasmas, a brief discussion is warranted. A more detailed discussion about excitation mechanisms is available elsewhere [63,64].

In the previous section, the term "gas discharge" is widely used. Gas discharge is a general term used to describe both glow discharges and plasmas. The glow discharge is the generic name for an extensive class of gas discharges with a cathode fall and a space charge. On the other hand, a plasma can be simply described as a partially ionized gas with an equal number of positive and negative charges. In such a plasma, the principal species present are neutral atoms, ions, and unbound or free electrons.

The collisional processes are assumed to be the most important mechanisms through which analyte excitation and ionization occur. Collisional processes can be of the elastic or inelastic type depending on whether the internal energies of the colliding particles are conserved. Particles usually have two types of energy: kinetic and potential energy. In

an elastic collision, there is interchange of kinetic energy only. In an inelastic collision, there is no such restriction and potential energies can also change. Therefore, kinetic energy of one particle may be lost to excite or ionize the second particle.

The following discussion is limited to the inelastic collisions (excitation) and radiative processes (de-excitation: characteristic line spectra) involving the analyte atomic species. The relevant species considered here are, M; ground state analyte atom (or ion), M^*; excited state analyte atom (or ion), He; ground state plasma gas, He^*; excited state plasma gas, $He^{*,m}$; excited metastable state, and e; free electron. The following are the important collisional radiative processes.

Mechanism I. Electron Impact Excitation

$$M + e \longrightarrow M^* + e$$

In the electron impact excitation, a fast moving electron collides with an analyte atom (or ion) in a lower energy state and the kinetic energy of the electron is taken up to excite the analyte atom (or ion). Excess kinetic energy is carried away by the primary electron. This process is assumed to be the most important mechanism for the excitation of analyte in the plasmas. The reverse process is called collisional de-excitation.

Mechanism II. Collisional ionization

$$M + e \longrightarrow M^+ + e + e$$

In this process, an atom is ionized by impact with a fast moving electron. The kinetic energy of the electron must be at least as large as the ionization potential of the atom (or greater than the binding energy of the ionizing electron in a particular excited state). The reverse process is called three-body recombination.

Mechanism III. Penning Excitation

$$M + He^{*,m} \longrightarrow M^* + He$$

Penning excitation (or ionization) of the analyte is caused by collision with metastable helium atoms. For such an energy transfer, resonance condition applies. In addition, in an atmospheric pressure plasma, the life time of the metastable species is very short. Therefore, this mechanism is assumed to be insignificant in atmospheric pressure plasmas.

Mechanism IV. Radiative Recombination

$$M + e \longrightarrow M^* + h\upsilon_{cont}$$

In this case, M is the analyte ion and M^* is an analyte atom in the excited state. The energy of recombination ($h\upsilon_{cont}$) produced in this reaction has a continuous range, because the colliding electrons posses a range of energies. The recombination of helium ions with electrons produces the continuum background emission.

Mechanism V. Radiative De-excitation

$$M^* \longrightarrow M + h\upsilon_{line}$$

In the radiative de-excitation, the excited analyte atom (or ion) relaxes to a lower state by emitting a quantum of radiation energy. Radiative de-excitation is the most important mechanism for emission spectrometry, because it creates characteristic line spectra. The reverse process is called absorption.

1.4.4 Plasma Temperature

The temperature of the plasma is an important consideration in atomic spectrometry. Relatively high temperature plasma sources such as ICPs give rise to intense line emission for the analyte and low matrix interference effects in analytical determinations. As such, high temperature plasma sources are considered to possess superior analytical merits compared with those of low temperature plasmas.

A unique temperature for a system can be specified only if the system is in a state of thermal equilibrium. However, for laboratory plasmas, temperature described by Planck distribution is not fulfilled. Furthermore, partially ionized gases like plasmas consist of heavy particles such as atoms and ions, as well as electrons. For such a system, one temperature can be considered when the heavy particles and electrons have the same kinetic energy. For most laboratory plasmas, existence of such an energy equilibrium is rare.

If thermal equilibrium is not established, a single temperature can not be assigned to the plasma. This non-thermal equilibrium leads to several different definitions of temperatures in the plasma depending on the species considered. These are electron kinetic temperature (T_e, from the Maxwell velocity distribution), gas kinetic temperature (Tg, from the Maxwell velocity distribution), excitation temperature (T_{exe}, from the Boltzmann energy state distribution) and ionization temperature (T_{ion}, from the Saha equation). However, when the source is in a state of local thermal equilibrium (LTE), a unique temperature can be defined for each point in the source but allowing for the possibility of different temperatures at different points. A more comprehensive description of plasma temperatures and the relevant distribution functions are available elsewhere [65,66].

1.4.5 Spectroscopic Temperature Measurements

Spectroscopic methods are popular for the measurement of plasma temperatures, especially in high temperature plasmas, because they are non-invasive. Measured temperatures can be used to compare different plasma sources with respect to their ability to atomize, ionize, and excite analyte species. The measurement of the excitation temperature using the Boltzmann distribution is described below.

The emission intensity of a spectral transition from a higher energy level (p) to a lower energy level (q) can be expressed by:

$$I_{pq} = (L/4\pi) \times A_{pq} \times N_p \times (h\upsilon_{pq}) \qquad (1.1),$$

where I_{pq} (erg cm^{-2} sr^{-1} s^{-1}) is the absolute intensity of the emission line, A_{pq} (s^{-1}) is the Einstein transition probability, Np (cm^{-3}) is the number density of atoms in the upper energy level p, L (cm) is the source length, h (6.6262×10^{-27} erg s) is the Planck constant, and υ_{pq} (s^{-1}) is the frequency (λ_{pq} is the wavelength) of the spectral line emitted [66].

The number density of particles in excited level p (N_p) is given by the Boltzmann distribution:

$$N_p = (Ng_p/Q(T)) \exp(-E_p/kT_{exe}) \qquad (1.2),$$

where N (cm^{-3}) is the total atom (or ion) density, g_p is the degeneracy of the upper level p, Q(T) is the partition function, E_p (erg) is the energy of the upper energy level p, k is the Boltzmann constant (1.3805×10^{-16} erg K^{-1}), and T_{exe} (K) is the excitation energy. One can combine equations (1.1) and (1.2) to obtain:

$$\ln(I_{pq}\lambda_{pq}/g_pA_{pq}) = \ln(k\,N) - E_p/(kT_{exe}) \qquad (1.3),$$

where k is a constant. Therefore, the excitation temperature, T_{exe}, can be determined by measuring the relative intensity of each spectral line and plotting $\ln(I_{pq}\lambda_{pq}/g_pA_{pq})$ as a function of E_p. The slope of the line ($-1/kT_{exe}$) then provides the T_{exe}. Alternatively, A_{pq} may be replaced by f_{qp} (the oscillator strength), and $\ln(I_{pq}\lambda_{pq}^3/g_qf_{qp})$ is plotted as a function of E_p. In this case, g_q is the degeneracy of the lower level q of the transition. This spectroscopic method of temperature determination is normally called the slope method.

For spectroscopic temperature measurements, the relative emission intensity measurements must not suffer from self-absorption and should be proportional to the absolute emission intensity. It should be noted that the value of $\ln(k\,N)$ will vary during the atomization step of the analyte, because the total atom density in the furnace varies, but will be a constant for all lines of an element at any specific instance.

Alternatively, for two upper energy levels, p and q, one can combine equations (1.1) and (1.2), and rearrange to:

$$\ln(I_p/I_q) = \ln[(g_pA_p / \lambda_p) / (g_qA_q / \lambda_q)] - (E_p-E_q)/kT_{exe} \qquad (1.4).$$

Therefore, by measuring the relative intensities of two lines at different energies, it is possible to calculate the excitation temperature as a function of time during the atomization step. This method of temperature determination is called the two line method.

The following considerations should be noted for spectroscopic temperature measurements. As stated previously, a unique temperature can only be used to describe the plasma if the plasma is in thermal equilibrium. With a non-thermal equilibrium, a variety of temperatures can be used to describe the plasma, depending on the statistical distribution and the thermometric species used for the measurement [67,68]. The accuracy of spectroscopically measured temperatures is dependent on the accuracy of the transition probabilities [67]. Furthermore, if the plasma is not in LTE, the experimental temperature is applicable only to the energy levels of the thermometric species used to drive it [69].

1.5 Overview of the Thesis

Furnace Atomization plasma excitation spectrometry (FAPES) is a new spectrometric method, and hence, the work described in this thesis is focused on the characterization of the RF plasma in FAPES as a spectrochemical source for elemental analysis. An effort has been made to distinguish the effects of the plasma on the analyte from those of graphite furnace without the plasma. The scope of the thesis is presented below.

A new experimental system, developed for the measurement of temporally and spatially resolved transient signals, is described in Chapter 2. This experimental system can be employed to acquire two data channels simultaneously. A complete software package is written to acquire and process the transient signals obtained from the FAPES source.

Spectral, spatial, and temporal emission characteristics of the RF plasma source are studied. To this end, time averaged Fe-excitation temperatures of this new plasma source are measured. Both atomic absorption and atomic emission are measured to study the effect of plasma on the temporal response of the analyte emission signal. Analyte atomization, vaporization and excitation characteristics are discussed. Moreover, the temporal behavior of the analyte emission signal is discussed with respect to physical and chemical phenomena. This work is described in Chapters 3 and 4 of this thesis.

Chapter 5 deals with the effect of RF power on the Pb emission characteristics and the plasma background emission. The time-resolved Pb-excitation temperature is measured to study the effect of the Pb-excitation process on the observed signal. Factors that affect the analytical figures of merit for a FAPES determination are also discussed.

Sodium chloride and $NaNO_3$ matrix interference effects in FAPES are investigated with the aim of understanding interference mechanisms and the effect of the RF plasma on the interference effects. The temporal behavior of the analyte and the interferent in the gas-phase is studied. Similarities and differences between NaCl and $NaNO_3$ interference effects on Ag and Pb emission intensities are also presented in Chapter 6.

CHAPTER 2

THE EXPERIMENTAL SYSTEM

As stated in the introduction, one of the objectives of this thesis was to setup an experimental system to characterize the atmospheric pressure helium plasma source at 13.56 MHz in FAPES. This chapter describes the experimental system developed for the characterization of this RF plasma source in FAPES. A description of this experimental system is also available elsewhere [70,71].

2.1 INSTRUMENTATION

Figure 2.1 presents a schematic block diagram of the experimental system employed for the acquisition of spatial and time-resolved signals. The main components of this experimental system were: an RF power supply, an RF matching network and the plasma source work-head for igniting and sustaining the plasma, and a furnace power supply for resistance-heating the graphite furnace. In addition, two lenses (L1 and L2), a monochromator, and a photomultiplier tube (PMT) were employed for the spectral isolation and detection, along with a current amplifier, an analog-to-digital converter (ADC), and a computer (PC/AT) for the data acquisition.

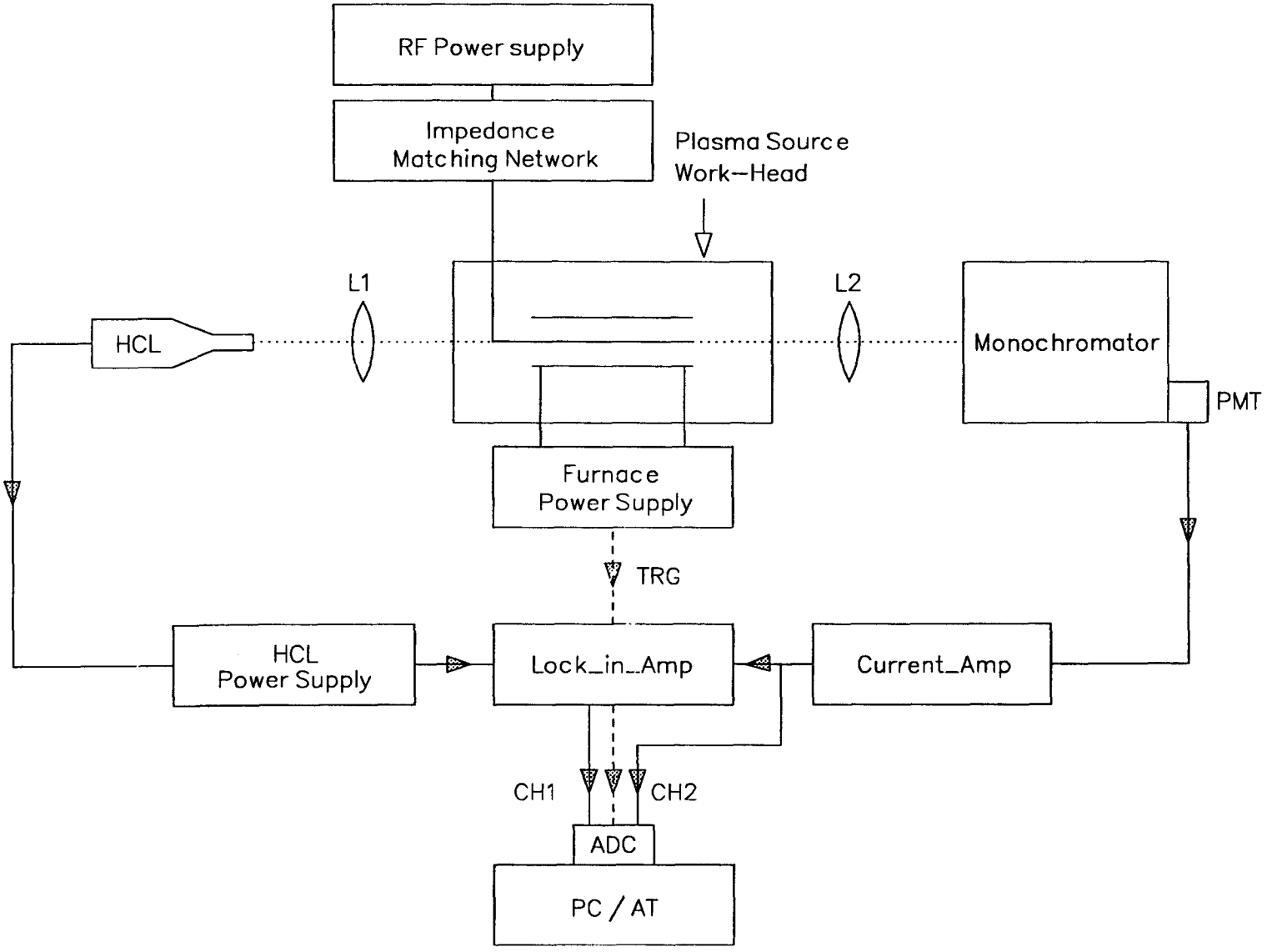

Figure 2.1 Schematic diagram of the experimental system.

The ADC data channels are labelled as CH1 and CH2 in Figure 2.1. When the atomic absorption signal was measured simultaneously with the atomic emission signal, a lock-in-amplifier was employed to detect the hollow cathode lamp (HCL) signal from the PMT output as depicted in Figure 2.1. For other experiments, CH2 was directly connected to the output from the corresponding signal transducer (for example, optical pyrometer) to acquire the data. The trigger channel for the ADC is labelled as TRG in Figure 2.1.

The sections that follow in this chapter, describe each of these components along with data acquisition, data processing, and the FAPES method.

2.1.1 The Plasma Source Work-Head

Figure 2.2. provides a schematic diagram of the plasma source work-head. The main components of this plasma source work-head were: a pyrolytic-graphite coated integrated contact cuvette (ICC) and a pyrolytic-graphite coated co-axial rod (Ringsdoff-Werke, BadGodesberg, Germany); and a high current furnace support structure, machined from copper and Macor™, contained in a five-way hollow cube machined from aluminium. The ICC was 19 mm long, 5.7 mm in internal diameter, and 7.1 mm in outer diameter. The co-axial rod was 0.9 mm in diameter, and extended the full length of the graphite furnace. The hollow five-way cube was $6 \times 6 \times 6$ inch with 5 inch diameter ports in five of the six sides. Each of these ports was fitted with a 5.5 inch diameter "O"-ring sealed aluminium flange. This five-way cube could be evacuated to about 1 mtorr, if necessary.

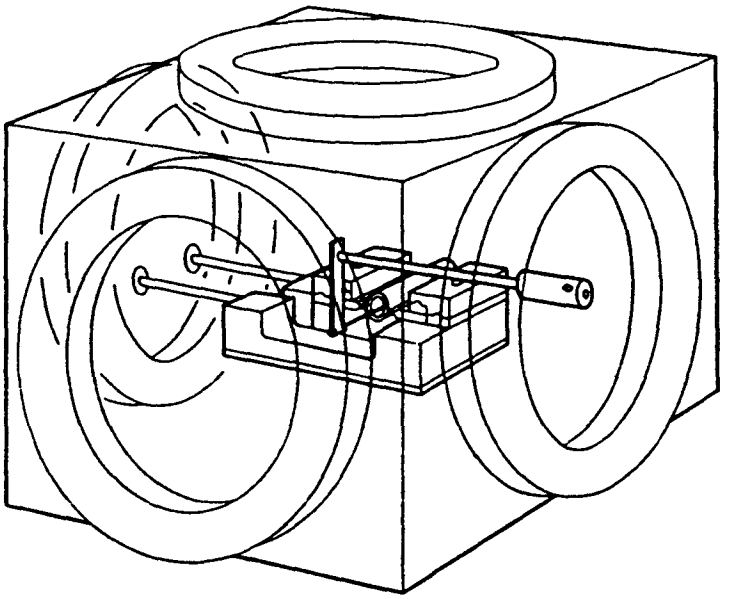

Figure 2.2. Schematic diagram of the plasma source work-head.

The furnace support structure and the water cooling system of the graphite furnace were designed similar to the method described by Ballou *et al.* [14]. The graphite furnace was resistance-heated by employing a furnace power supply (Model IL-555, formerly Instrumentation Laboratory; now Thermo-Jarrell Ash, Waltham, MA, USA), unless otherwise noted. The plasma gas entered the plasma source work-head from a small inlet on the flange with the furnace support structure. The plasma gas outlet was located on the flange opposite to the flange with the furnace support structure.

Thus, the plasma gas had no directed flow through the graphite furnace. For all experiments described in this thesis, a gas flow rate of 6 SCFH (the gas flow rate reading of the furnace power supply in units of standard cubic feet per hour of air) was used. Silver atomic absorption signals measured as a function of gas flow rate, from 4 to 20 SCFH, showed no significant effect on either peak height or peak area measurements.

The co-axial graphite rod was powered through an RF connector and two vertical metal blades, in the manner depicted in Figure 2.2, unless otherwise noted. This arrangement for the co-axial rod (as depicted in Figure 2.2), for the simultaneous measurement of absorption and emission signals, is called the " vertical-mount ". The alternative arrangement, when the co-axial rod is directly connected to the RF connector, is called the " horizontal-mount ". The end view of these two arrangements is depicted in Figure 2.3. In this thesis, the RF powered co-axial rod is called the " RF electrode ", unless otherwise noted.

The plasma was viewed through a 1 inch diameter quartz window on the front-side flange. A similar quartz window on the opposing backside allowed a light source to be directed through the graphite furnace so that an atomic absorption experiment can be carried out or the horizontal-mount can be installed instead of the quartz window. The analyte sample was deposited onto the inner furnace wall (or onto the RF electrode) through a small screw-top port mounted on the top flange. The plasma source work-head was

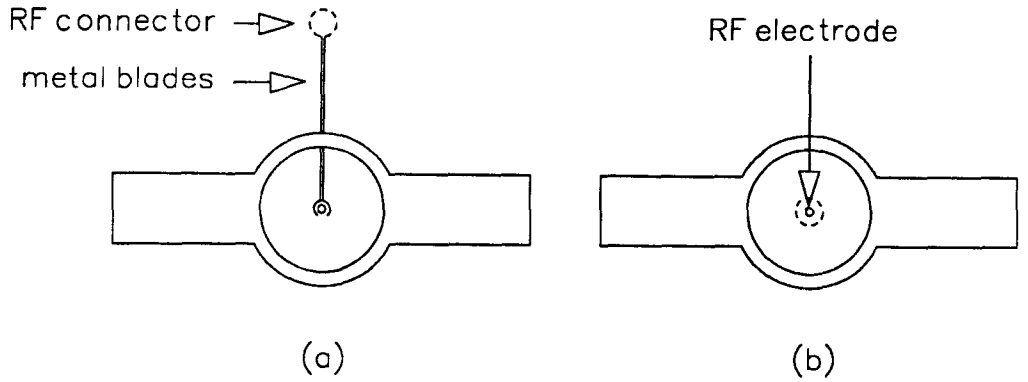

Figure 2.3. End view of the (a) vertical mount and (b) horizontal mount. The dash line represents the RF connector.

constructed in the mechanical services shop of the chemistry department at University of British Columbia.

2.1.2 The Atmospheric Pressure RF Discharge

A helium gas discharge was sustained inside the graphite furnace by employing a 13.56 MHz RF generator (Model RFX-600, Advanced Energy, Fort Collins, CO, USA), an automatic power tuner (Model ATX-600,

Advanced Energy, Fort Collins, CO, USA), and an impedance matching network (Model 5017-000-G, Advanced Energy, Fort Collins, CO, USA). The output of the impedance matching network was coupled to the RF electrode through a variable 1 - 10 μH inductor. This arrangement could be used to ignite and sustain a helium discharge over the RF power range between 12 and 25 W. At RF powers between 25 and 50 W, occasional arcing was observed between the RF electrode and the furnace wall. Although consistent arcing was observed, a gas discharge could be maintained at RF powers between 50 and 150 W.

When operating at RF powers below 75 W with an atomization temperature of about 2100 K, the reflected power was stable below 1 - 2 W throughout the atomization step. At RF powers higher than 75 W, the reflected power could be maintained below 1 - 2 W, except during the atomization step. At an RF power of 100 W, after about 3.5 s into the atomization step, the reflected power started to increase to a value as high as the applied RF power. Furthermore, under these conditions, the reflected power would stay at these high values, even after the completion of the atomization step. Thus, temperature of 2100 K sets the upper limit of the atomization temperature that can be used with this experimental setup. Moreover, reflected power increased frequently during the atomization step when the horizontal-mount was employed compared with the vertical-mount, probably due to arcing between the furnace wall and the base of the RF connector.

In addition, sufficient cooling of the furnace support structure made of copper during the atomization step and removal of the hot gases from the plasma source work-head after the atomization step were two important considerations for the usable atomization temperature with this experimental system. Once the atomization temperature was set, the heating rate was limited by the IL-555 furnace power supply.

2.1.3 Spatially Resolved Intensity Measurements

The plasma source work-head was mounted on a post which in turn was mounted on a crank-driven linear translation stage which allowed the work-head to be moved laterally relative to the detection system. For spatially resolved emission intensity measurements, the plasma source work-head was translated in increments of 0.1 mm. The movement of the platform was monitored using a precision displacement indicator gauge (Model 2047-11, Mitutoyo, Japan). For the spatially resolved experiments, emission intensities were recorded on a chart recorder. The plasma was viewed, 1.2 mm from the RF electrode (unless otherwise noted), on the opposite side of where the sample was deposited.

2.1.4 Spectral Isolation and Detection

A 0.35 m Czerny-Turner monochromator (Model 270, Schoeffel-MacPherson, MA, USA) with a holographic grating with 2400 lines/mm was employed, with an entrance slit of 70 μm wide and 2 mm high, unless otherwise noted.

For atomic absorption experiments, a 1 : 1 image of the hollow cathode light source (Hamamatsu, Japan) was formed at the center of the furnace by employing a 20 mm diameter, 75 mm focal length fused silica lens: L1 (Melles Griot, Irvine, CA, USA). The 1 : 1 image of the plasma was formed at the entrance slit of the monochromator by employing a 35 mm diameter, 100 mm focal length fused silica lens: L2 (Melles Griot, Irvine, CA, USA). Signals were detected by employing a PMT (Model R955, Hamamatsu, Middlesex, NJ, USA). The PMT was operated at - 600 V. The output of the PMT was amplified by employing a current amplifier (Model 427, Keithley, Middlesex, NJ, USA). The rise time of the current amplifier was 0.3 ms, unless otherwise noted. The image of the plasma source was aligned with the entrance slit of the monochromator by employing a HeNe laser (Miles Griot, Irvine, CA, USA).

2.1.5 Atomic Absorption Measurements

For atomic absorption measurements, output of the current amplifier was divided and one of the channels (CH2) was selectively detected by a lock-in-amplifier (Model 121, PAR, Princeton, NJ, USA) with a 30 ms time constant. The HCL source used for the atomic absorption experiments was modulated at 200 Hz by employing a pulsed power supply (Electrical Services Shop, Department of Chemistry, UBC). This pulsed power supply can modulate up to 500 Hz and can deliver up to 100 mA of current. The HCL output was saved, and absorbance was calculated, when necessary.

2.1.6 Graphite Furnace Temperature Measurements

The radiation emitted from the graphite furnace during the atomization step was monitored using an optical pyrometer (Ircon Series 1100, Model 11 × 30, IL, USA) which viewed the sample introduction hole (without the RF electrode) through a 1 inch diameter quartz window on the top flange. The optical pyrometer was mounted on a support-arm which in turn was fixed to the plasma source work-head by a vertical post. The optical pyrometer could be slid along the support-arm which in turn could be rotated 360^0 around the vertical post. This arrangement allowed the optical pyrometer to be focused onto a selected position on the graphite furnace.

The output from the pyrometer was amplified by an amplifier (Electrical Services Shop, Department of Chemistry, UBC), and then digitized. The digitized data were converted into absolute temperature by using the calibration data provided by the pyrometer manufacturer and fitted to a 8^{th} order polynomial least square fit. The graphite furnace was assumed as a grey body radiator with an emissivity of 0.7. The temperature below the range of the optical pyrometer was determined by extrapolating furnace temperature back to the ash temperature. The ash temperature was measured using a thermocouple (Model 80TK, John Fluke, Everett, WA, USA). The atomization temperature was the maximum temperature reached by the graphite furnace during the atomization step of the analyte.

The appearance temperatures of analytes were calculated based on their appearance times and the temperature-time profile of the graphite furnace.

The appearance time was defined as the time taken for the absorbance or the emission signal to reach the average base line plus two standard deviations of the base line noise. The peak temperature was defined as the temperature at which maximum absorption or emission occurs.

2.2 Data Acquisition

The data acquisition was started when the ADC was triggered by a trigger signal from the graphite furnace power supply at the start of the atomization step. The input from single channel or two channels was digitized with a 12-bit resolution by employing a sixteen channel ADC (Model ADM12-10, Quatech, Akron, OH, USA) capable of operating at a maximum sampling rate of 30 KHz, and stored by using a 12 MHz IBM PC/AT compatible computer.

The data acquisition software facilitated two signals: analyte and background, to be acquired, and along with the background corrected signal, to be stored in the computer. The rate of data acquisition (maximum of 250 Hz) and the number of data points per channel (maximum of 2000 points) were software selectable, and were limited by the free conventional memory allocated by the Ver. 4.0 of MS-DOS™. The ADC was addressed by incorporating the software provided by Quatech Co.

2.3 Data Processing

The data processing software was written in Turbo Pascal (Borland International, CA, USA), and facilitated the calculation of diagnostic information, such as peak height, peak area, and the peak width of the temporal response of the emission signal. The other options included were background correction, signal averaging, smoothing, displaying, and generating plots for HP™ plotters.

All graphs and curve fittings shown in this thesis were completed with the aid of Axum: Technical Graphics and Data Analysis program (TriMetrix, WA, USA).

2.4 The FAPES Method

The analyte sample was deposited onto the inner furnace wall (or onto the RF electrode), and was subjected to the thermal treatment. The duration of these heating steps could be selected and furnace temperature program was in auto mode. Within the next 10 s lag time, RF power was applied to the RF electrode and the plasma was ignited. This lag time allowed sufficient time to ignite and to stabilize the plasma before the start of the atomization step. After this lag time, the atomization step was started. Data acquisition was automatically triggered at the start of the atomization step. The duration of the atomization step was limited to a minimum of 5 s by the

furnace power supply. All signals were acquired for 8 s. The next step was the cooling step of the graphite furnace. After the cooling step, the system was ready for the next sample. The sample throughput was 4 to 6 samples per hour.

It should be noted that this chapter describes only the experimental system developed. The specific experimental methods along with the experimental parameters will be presented with each study. The next chapter will present some basic characteristics of the RF plasma.

CHAPTER 3

SPECTRAL AND EXCITATION CHARACTERISTICS OF THE ATMOSPHERIC PRESSURE HELIUM PLASMA SOURCE IN FAPES

3.1 INTRODUCTION

Spectral characteristics of a plasma are among the most important considerations for the successful utilization of a plasma source in emission spectrometry. Spectral characteristics may affect the background and noise in the background in a spectrochemical determination. Signal-to-background ratio (SBR) and noise in the background are two important characteristics that affect the detection limit of an analytical method [72,73]. Spectral characteristics of plasma sources are also useful when studying the fundamental properties of plasmas.

In addition to spectral characteristics, it is well known that the excitation temperature is an important fundamental property which is closely associated with the analyte excitation and ionization. In high temperature plasmas, analytes produce intense atomic (or ionic) line spectra which can be used for analytical determinations. The emission intensity of an analyte depends on the total number of atoms (or ions) in the volume from which the signal is collected and the fraction of atoms (or ions) that are in the excited

state. The population of a given excited state is proportional to the Boltzmann factor: $e^{-E_p/kT_{exe}}$ (Section 1.4.5). For example, for an excited state with an energy of 4.3 eV, the Boltzmann factor is 25 times higher at 4500 K than at 3000 K. If the number of atoms per unit volume remains constant, emission intensity should increase by a factor of 25 when the temperature changes from 3000 to 4500 K. The more intense analyte emission provides a higher sensitivity in analytical determinations.

Furthermore, many excited states are populated in a high temperature plasma, so that an alternative line can be used when a spectral interference occurs by an emission feature in the background or another interfering line in a multi-elemental analysis. Moreover, high temperature plasmas provide an excitation environment relatively free from matrix interferences.

In this study, some of the basic characteristics of the helium plasma source at 13.56 MHz in FAPES were investigated. Spectral, spatial, and temporal profiles of the plasma emission features, and the excitation temperature measured by using iron as a thermometric species are presented in this chapter. Furthermore, the importance of these plasma properties to FAPES will be discussed. The work described in this chapter has been previously published by Hettipathirana and Blades [70].

3.2 EXPERIMENTAL

The experimental system described in Chapter 2 and a horizontal-mount for the RF electrode were employed in the present study. The following experimental methods and parameters should also be noted.

The plasma source work-head, employed for the collection of background spectra depicted in Figure 3.1, was an IL-455 (formerly Instrumentation Laboratory, now Thermo-Jarrel Ash, Waltham, MA, USA) Massmann-type furnace work-head fitted with a pyrolytic-graphite coated RF electrode [15]. This furnace work-head could be quite effectively purged and sealed, allowing spectra to be collected without ingress of atmospheric pressure gases. This helium plasma source was operated at 27 MHz and at an RF power of about 20 W.

3.2.1 Plasma Background and Iron Emission Spectra

A 1 m Czerny-Turner monochromator (Model 2061, Schoeffel-McPherson, MA, USA) was used for the measurement of plasma background spectra, and iron spectra for excitation temperature measurements. This monochromator was equipped with a holographic grating with 1200 lines/mm (Model AH-3264, Schoeffel-McPherson, MA, USA). The image of the plasma was formed at the entrance slit of the monochromator by employing a 150 mm focal length, 50 mm diameter plano-convex fused silica lens (Oriel, Stratford, CT, USA). For the Fe-excitation temperature measurements, the

image of the plasma was taken from a distance of 1 mm from the RF electrode using a slit height of 2 mm and a slit width of 70 μm such that the area of the discharge sampled had the same dimensions (1 : 1 imaging).

The source of Fe for the temperature measurement was from a micro-pipette deposition of 5 μL of a 10 ppm Fe solution. Iron solutions in 1 % (v/v) HNO_3 were prepared by dissolving analytical grade $FeSO_4.7H_2O$ (BDH, Toronto, Canada). Five replicate depositions were made at each RF power setting. The sample was dried at about 390 K for 1 min, with a 1 min thermal pre-treatment step at about 770 K (during which the plasma was ignited). The temperature was then ramped to 2100 K. Emission spectra were recorded by integrating the signal for 7.5 s. This integration time is longer than is actually required because the signal only lasts for a period of about 1 - 2 s. However, difficulties in synchronizing the timing of the graphite furnace atomization step and the beginning of an array integration period precluded the use of a shorter integration time.

The detector employed was a linear photodiode array (LPDA: Model RL-2048S, Reticon, Sunnyvale, CA, USA). The array integration period and readout were controlled by employing a satellite controller board (Model RC1021, Reticon, Sunnyvale, CA, USA). Using an entrance slit of 70 μm, the LPDA spectrometer provided a resolution of 0.06 nm while allowing the simultaneous measurement of a spectral window about 40 nm wide. The wavelength *vs* diode calibration was carried out by measuring emission lines of Cd, Pb, and Fe. A thermoelectric cooler

(Model CP14-71-10L, Melcor, Trenton, NJ, USA) mounted on the backside of the LPDA allowed it to be cooled to -20 ^{o}C.

Data acquisition was carried out by interfacing the LPDA to a 12-bit ADC (Model ISC-16, RC Electronics, Santa Barbara, CA, USA) which was interfaced to a 12 MHz IBM PC/AT compatible computer which also was used to set the integration time for the LPDA. In-house software for acquisition of the LPDA spectra was available.

3.2.2 Spatially and Temporally Resolved Spectra

A 0.35 m Czerny-Turner monochromator (Model 270, Schoeffel-McPherson, MA, USA) equipped with a holographic grating with 1200 lines/mm was employed for spatial and temporal emission measurements. The 1 : 1 image of the plasma was formed at the entrance slit of the monochromator by employing a 100 mm focal length, 35 mm diameter fused silica lens (Melles Griot, Irvine, CA, USA). The entrance slit was 50 μm wide and 1 mm high.

The detector employed was a PMT (Model R955, Hamamatsu, Middlesex, NJ, USA). The PMT output was amplified by employing a current amplifier (Model 427, Keithley, Middlesex, NJ, USA). Output from the current amplifier was converted to digital form by employing an ADC (RC Electronics, Santa Barbara, CA, USA) and, stored in a 12 MHz IBM PC/AT compatible computer for further processing. The data acquisition

was accomplished by the software provided by RC Electronics Co. For temporally resolved measurements, 4000 points were taken at 500 Hz.

3.3 Results and Discussion

3.3.1 Background Emission Spectra

Typical background emission spectra for a 20 W helium plasma source are provided in Figure 3.1; for the spectral regions, 220 - 300 nm (Figure 3.1.a), 300 - 400 nm (Figure 3.1.b), and 400 - 520 nm (Figure 3.1.c). In general, the wavelength range, 200 - 500 nm, is considered as the analytically useful wavelength range in atomic emission spectrometry. The most prominent spectral features in the background emission spectrum are: CO^+ (First negative system of CO), OH, NH, N_2 (second positive system of N_2), and N_2^+ (first negative system of N_2). These spectral features are listed in Table 3.1. Reference data on molecular spectra are available [74].

These spectra were collected when the furnace was at room temperature and the plasma source work-head was continuously purged with helium. The composite spectra were constructed by integrating 12 different photodiode array spectral windows, each 40 nm wide, into a single background emission spectrum. Integration times ranging from 2 to 10 s were used. Figure 3.1 allows a comparison of the relative intensities of the spectral features. However, it should be noted that the spectra have not been corrected for the spectral response of the measurement system.

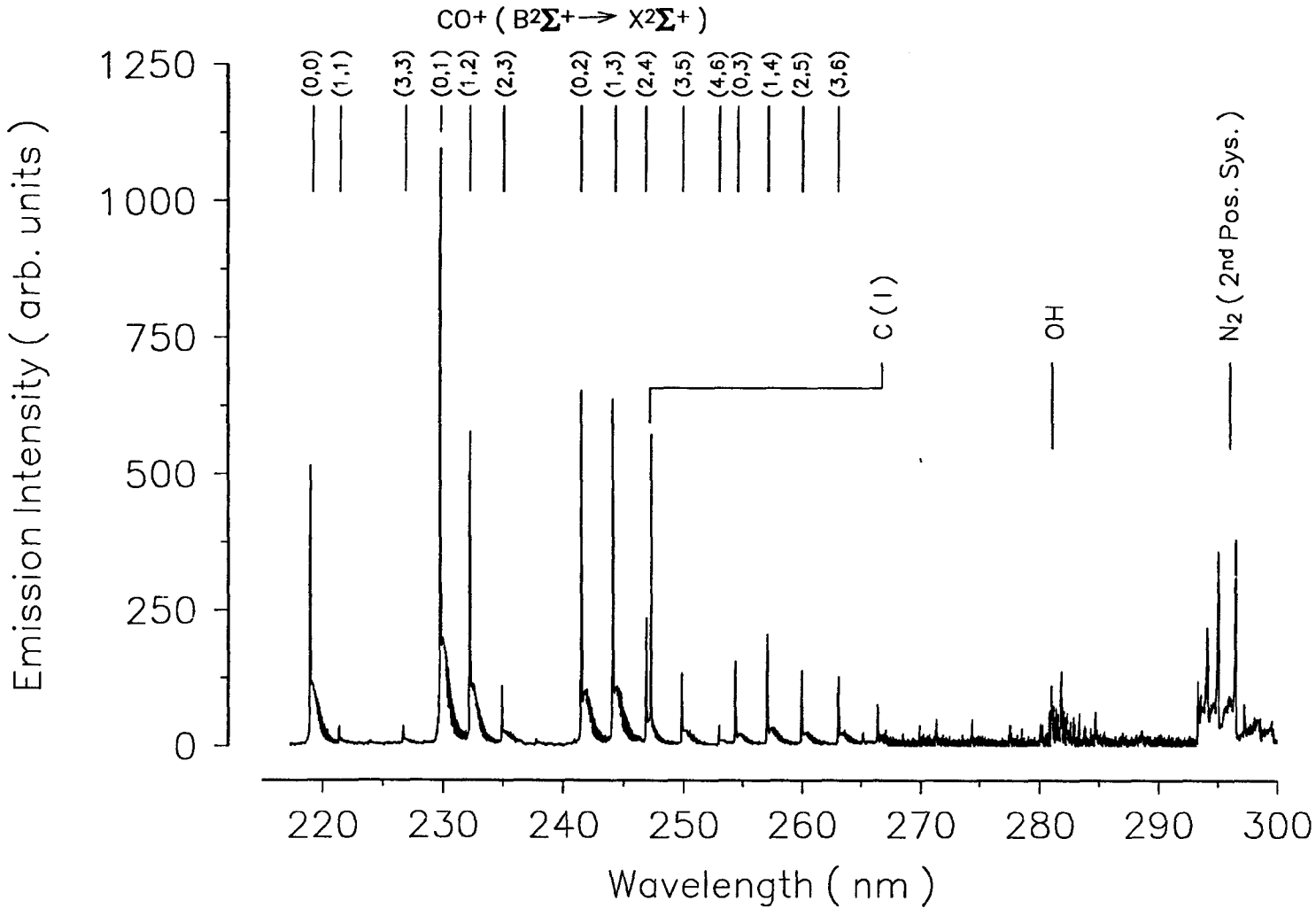

Figure 3.1.a. (continued on page 56)

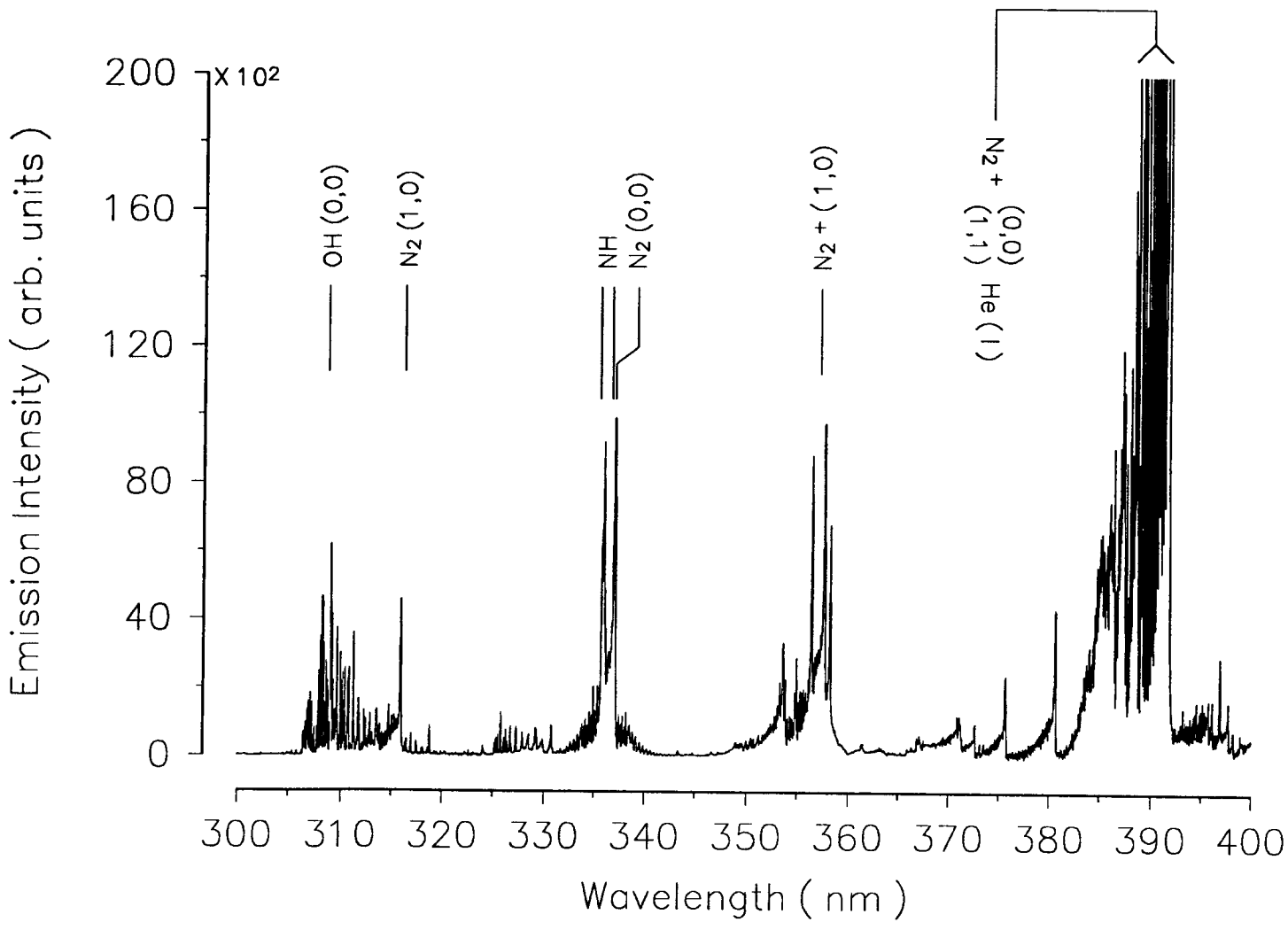

Figure 3.1.b. (continued on page 57)

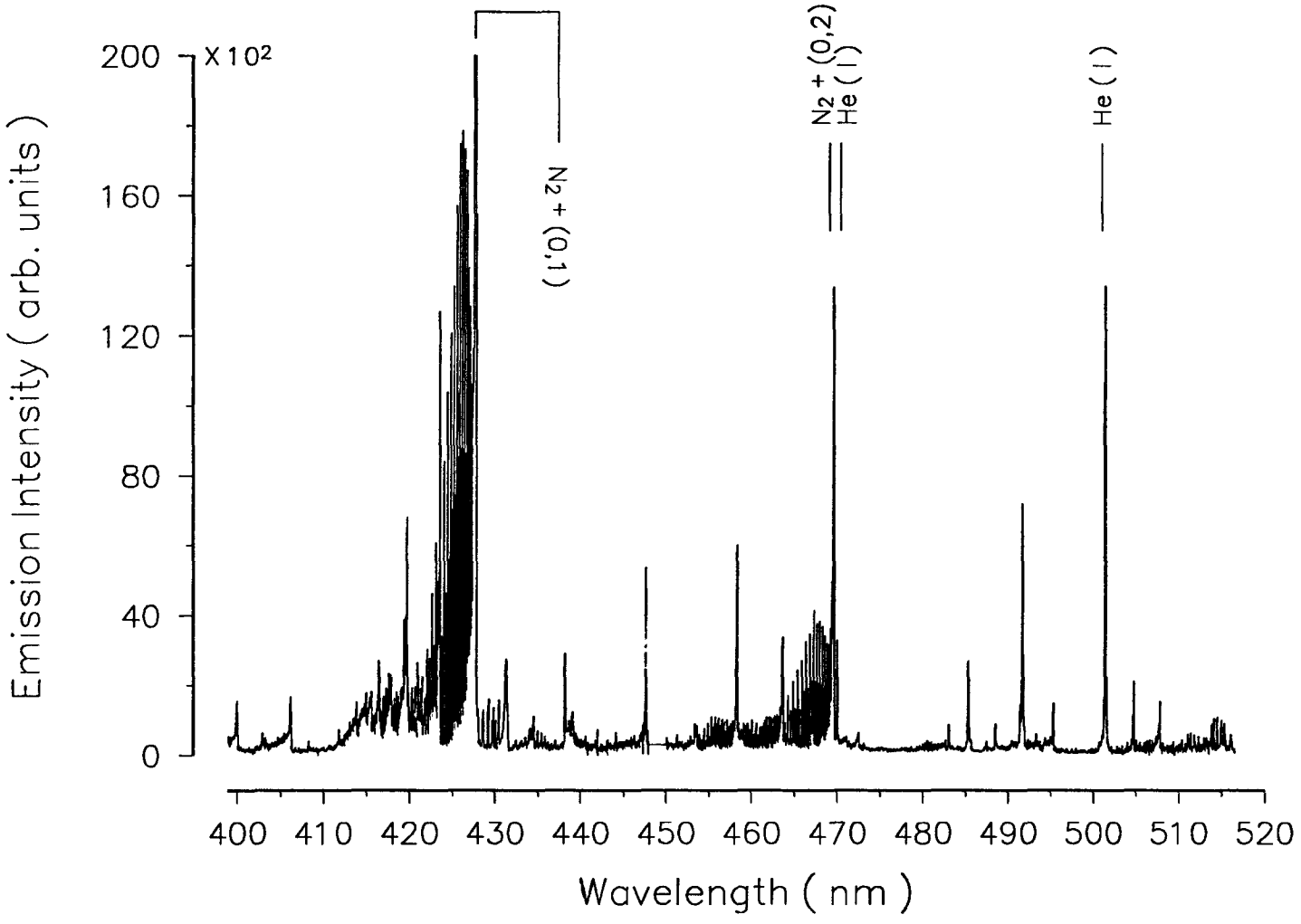

Figure 3.1. Background Spectra of helium plasma. (a) 215 - 300 nm, (b) 300 - 400 nm, and (c) 400 - 515 nm.

Table 3.1. Transitions of species observed in helium plasma at atmospheric pressure in 215 - 515 nm range.

Emitting species	Transition	Line wavelength or (0,0) Band-Head (observed range)
C (I)	$^1P_1 - {}^1S_0$	247.8
He (I)	$^1P_1 - {}^1S_0$	501.5
He (I)	$^3P_0 - {}^3S_1$	388.8
First negative system of CO	$B^2\Sigma^+ - X^2\Sigma^+$	219 (215 - 280)
OH	$A^2\Sigma^+ - X^2\Pi$	306 (280 - 320)
Second positive system of N_2	$C^3\Pi_u - B^3\Pi_g$	337 (295 - 400)
NH	$A^3\Pi - X^3\Sigma^-$	336 (336 - 337)
First negative system of N_2	$B^2\Sigma_u^+ - X^2\Pi_g^+$	391 (330 - 470)

These prominent emission features in the 27 MHz helium plasma (see Section 3.2) are also observed in the 13.56 MHz helium plasma operating at an RF power of 20 W. For the RF power range between 20 and 50 W, no frequency dependence on the background emission features is noted. Furthermore, during an atomization step of 1800 K, all prominent background emission features observed in the 27 MHz plasma are observed in the 13.56 MHz plasma. At both frequencies, an increasing continuum background beyond 450 nm is also observed because of the black-body emission from the furnace wall.

In the 220 to 270 nm region, the spectra are dominated by emission bands of CO^+ (Figure 3.1.a). However, these CO^+ bands are not observed when Ar is used as the plasma gas (Section 3.3.4). It is well known that CO^+ is readily excited in helium discharges as a result of selective excitation of the $B^2\Sigma^+$ state of CO^+, according to the following reactions [75,76];

$$He_2^+ + CO \longrightarrow CO^+(B^2\Sigma^+) + 2He \qquad (3.1),$$

and $$He(2^1S, 2^3S) + CO \longrightarrow CO^+(B^2\Sigma^+) + He(1^1S) + e \qquad (3.2).$$

The variable potential energy of He_2^+ (18.3 - 20.3 eV) primarily accounts for the excitation of $CO^+(B^2\Sigma^+)$ state by the resonant charge-transfer mechanism [76]. The presence of these CO^+ bands in FAPES suggests that the helium plasma source could be quite effective for the selective excitation of analyte atoms and molecular species in cases where the energetics are

favorable. The other dominant feature is the emission from the different vibrational bands of N_2^+. The excitation of the N_2^+ system is also by charge-transfer from He_2^+, which selectively populates the $B^2\Sigma_u^+$ electronic level leading to intense (B-X) band emission [76].

The occurrence of these molecular bands presents a relatively intense plasma background upon which analytical signals must be measured. Most of these background spectral features arise from traces of impurities in the plasma gas and molecular species desorbed from the furnace wall (Section 3.3.3). The approximate concentration of impurities in the bottled helium used in these experiments were: $H_2 < 1$ ppm, $O_2 < 3$ ppm, $N_2 \approx$ 5 - 25 ppm, $CO_2 < 1 - 2$ ppm, $H_2O < 5$ ppm, and total hydrocarbons < 5 ppm. However, in graphite furnace methods, the sample matrix is usually the main source of contaminants in the gas-phase. In an analytical determination, the gas-phase within the graphite furnace may be dominated by various sample matrix decomposition products as well as water vapor and acid decomposition products. These species can be readily adsorbed on the furnace wall and desorbed during the atomization step of the analyte [77]. Therefore, in a real analysis, the plasma background is likely determined by the composition of the sample matrix. The intensities of background emission features are also dependent on the RF power.

Sturgeon *et al.* reported emission features for the spectral region 190 - 430 nm: CO, OH, CN, NH, and He (I) at 388.9 nm for a 50 W plasma (frequency was not given) [16]; and for the spectral region 200 - 510 nm: NO,

CO, N_2, OH, and He (I) lines at 388.8, 447.1, 471.3, 492.2, and 501.6 nm for a 50 W plasma at 13.56 MHz [78]. In a subsequent publication, the presence of CO^+ was reported for a 50 W helium plasma at 40 MHz [79]. Some He (I) lines (447.1, 471.3, and 492.2 nm) observed at 13.56 MHz helium plasma [78], were also absent in the helium plasma at 40 MHz [79]. The absence of CO^+ emission features in the 13.56 MHz helium plasma source employed by the Sturgeon group is probably due to a spatial difference or RF power coupling efficiency difference between the plasma sources employed by two groups, or both. The CO^+ emission intensity is low in the intermediate region between the RF electrode and the furnace wall (Section 3.3.2).

3.3.2 Spatially Resolved Background Emission Intensities

Figure 3.2 is a plot of the spatial distribution of emission from CO^+ at 20 W, observed by translating an image of the plasma source laterally in increments of 0.1 mm. There are some features of the CO^+ spatial distribution which should be noted. The spatial profile peaks at the center of the plasma source adjacent to the RF electrode and also near the wall of the graphite furnace. Most intense CO^+ emission is observed adjacent to the RF electrode than near the furnace wall. In addition, a more luminous region surrounding the RF electrode and a less luminous plasma filling the remainder of the graphite furnace volume can also be seen in this atmospheric pressure helium RF plasma in FAPES.

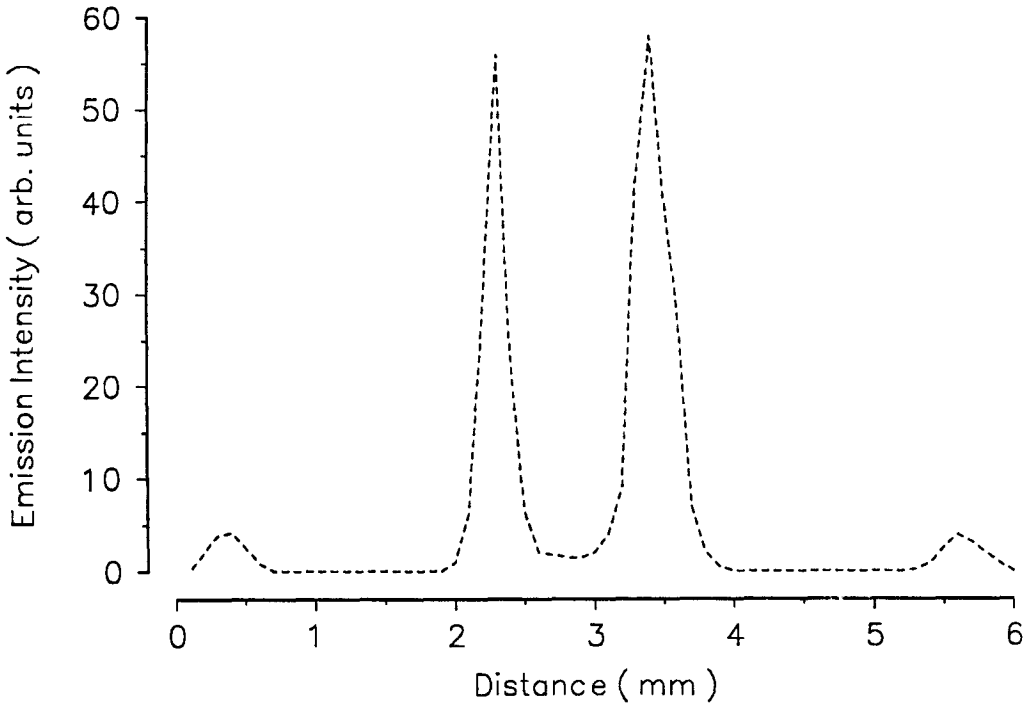

Figure 3.2. Emission spatial profile for CO^+.

The intense CO^+ emission near the RF electrode is likely due to a difference in RF field strengths at the RF electrode and at the furnace wall. This difference in the RF field strengths arises as a result of the differences in the surface area of electrodes: RF electrode and furnace wall. The higher RF field strength at the RF electrode leads to a high energetic excitation region adjacent to the RF electrode compared with that adjacent to the furnace wall. The low excitation region between the RF electrode and the furnace wall can be evidenced by very low emission intensity of CO^+ observed between the RF electrode and the furnace wall. Sturgeon *et al.* also reported

a He-excitation temperature difference of 400 K or more between the sheath adjacent to the RF electrode and the rest of the plasma [80]. Furthermore, in low pressure RF discharges, a higher field strength appeared at the smaller electrode [60].

At this time, it is not known whether the major source of CO is from the oxidation of the carbon surface on RF electrode and furnace wall, or sputtering of carbon from the RF electrode (and from the furnace wall) to oxidize in the gas-phase. However, in an atmospheric pressure helium plasma, it is most likely that CO^+ is mainly formed from the precursor CO, formed from the oxidation of carbon on the RF electrode and the furnace wall. The high reactivity at the RF electrode can also be evidenced by the gradual degradation of the RF electrode. This CO formation, in the presence of the plasma, is an additional source of CO which is absent in GFAAS.

Similar spatial behavior is observed for the He (I)† and N_2^+, although the profiles for OH and NH show significant emission in the intermediate region between the RF electrode and the furnace wall. Significant emission observed between the RF electrode and the furnace wall for OH and NH compared with that of CO^+ is likely due to differences in excitation mechanisms, high radiative life times, or both. The exciting species for both

---

† Spatial distribution of the Ar (I) emission line at 415.85 nm, when plasma source work-head described in Chapter 2 is employed as a low pressure hollow anode d. c. discharge, is similar to that of He (I) from the atmospheric pressure plasma in FAPES. For the low pressure plasma source, a cathode voltage of 460 V and pressure of 1.2 torr were used.

OH and NH is He^+ [75]. The radiative life times for OH and NH are 0.69 and 0.43 μs, respectively [81]. The radiative life times for CO^+ and N_2^+ are 0.05 and 0.06 μs, respectively. Regardless, spatial behavior of the molecular species is indicative of a strong excitation region adjacent to the RF electrode in this plasma source.

The spatial distribution of analyte emission is not measured because the transient nature of the signal makes this a time consuming measurement prone to error. The use of a slitless spectrograph combined with an imaging detector, similar to the system used by Gilmutdinov *et al.* for the collection of absorption shadow-grams [82], is one possible method for acquiring this information.

3.3.3 Temporally Resolved Background Emission Intensities

The variation of emission intensity for He (I), CO^+, N_2^+, and OH was measured during a dry (no aqueous sample was deposited) atomization step in order to examine the effect of furnace wall temperature on the emission intensity for these species. The results are given in Figure 3.3.a for He (I), Figure 3.3.b for CO, Figure 3.3.c for N_2^+, and Figure 3.3.d for OH, at RF powers of 14, 18, 22, 26, and 30 W, as marked on each figure. The time-resolved emission intensity profiles given in Figure 3.3 (a - d) show the variation of the intensity of a band-head during the atomization step. The atomization temperature profile corresponding to these figures is given in Figure 3.3.e.

For He (I) (Figure 3.3.a), there is an increase in the emission intensity at the beginning of the atomization step with increasing RF power and the emission intensity is relatively stable throughout the atomization step. The increase in the helium emission intensity, at the beginning of the atomization step, is due to the increase in excitation when the RF power is increased. The relatively stable helium emission intensity shows that the RF power coupling efficiency to the plasma is stable during the atomization step and not affected by the thermionic electrons at these furnace temperatures. Moreover, the helium emission signal shows a small increase during the peak atomization step. This small increase in emission intensity may be due to a change in the He-excitation temperature. However, Sturgeon *et al.* reported that, for a 100 W plasma, the He-excitation temperature was unaffected by the furnace wall temperatures between 500 and 2500 K [80].

For CO^+ (Figure 3.3.b), there is a dramatic increase in the emission intensity during the atomization step, followed by a depression at the peak atomization temperature, and a plateau as the furnace cools. This increase during the atomization step is most likely due to an increase in the amount of CO in the plasma as a result of increased desorption of CO from the RF electrode and the furnace wall. The depression at the peak atomization temperature could be attributed to recombination of CO^+ with the thermionic electrons liberated from the heated RF electrode to form CO. The thermionic electron emission from the RF electrode can also account for the time lag between the depression and the peak atomization temperature, as well as the

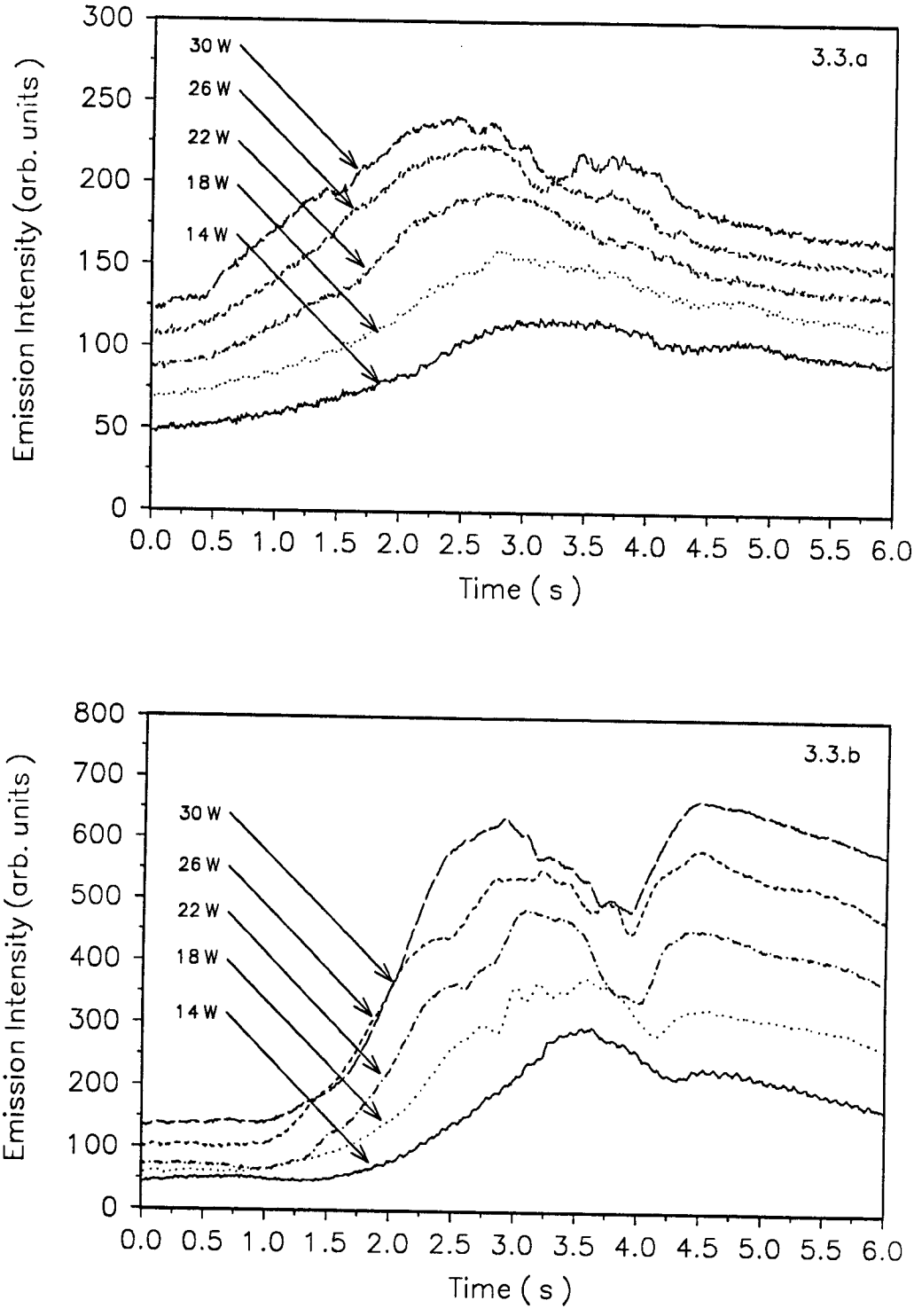

Figure 3.3.a and 3.3.b. **(continued on page 67)**

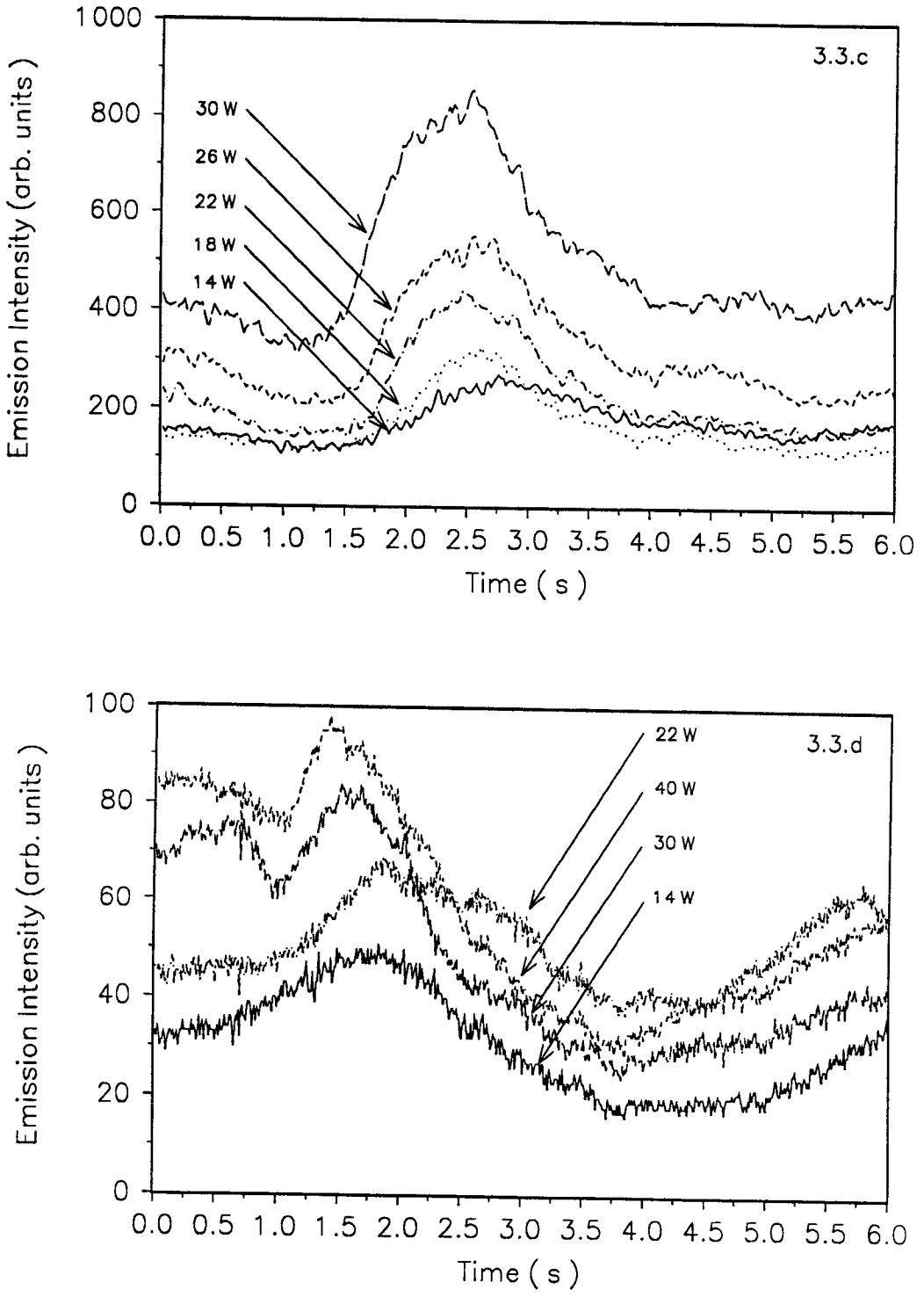

Figure 3.3.c and 3.3.d. (continued on page 68)

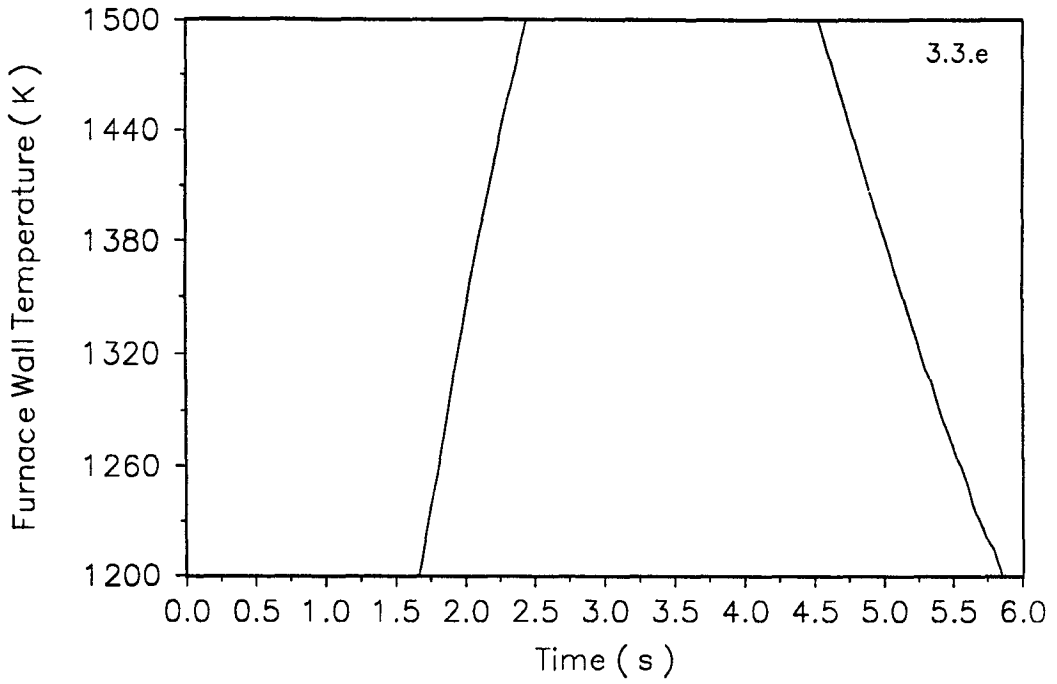

Figure 3.3. Temporal emission behavior for (a) He (I), (b) CO^+, (c) N_2^+, and (d) OH at RF powers of 14, 18, 22, 26, and 30 W; (e) furnace temperature corresponding to these diagrams*.

shift in the depression to earlier times with an increase in RF power. This observed depression may also be due to the recombination of He_2^+ with thermionic electrons, and hence, change in the excitation characteristics for CO^+.

---

* The X-axis in Figure 3 can be compared with similar figures in the rest of this thesis by adding 1.4 s.

If recombination of the thermionic electrons with molecular ions is the case, these molecular ions could act as a buffer, minimizing the effect of thermionic electrons on the total electron density in the discharge. The data for N_2^+ (Figure 3.3.c) support this suggestion because the temporal behavior at the atomization step for N_2^+ is similar to that observed for CO^+, and the depression appears near the temperature maximum. In addition, the temporal behavior for CO^+ and N_2^+ are dependent on both the incident RF power and the furnace temperature. In general, as the RF power is increased, at a given point in the atomization step, the emission intensity is increased as a result of the increase in excitation.

For OH (Figure 3.3.d), there is an initial increase, then a decrease in emission during the atomization step. Most probably, the temporal profile is the result of initial desorption of H_2O and OH, and subsequent dissociation, or increase in electron recombination with exciting species He^+.

3.3.4 Fe-Excitation Temperatures

The time-averaged Fe-excitation temperatures were evaluated by using six Fe (I) emission lines in the 370 - 377 nm spectral region, which were recorded by employing the photodiode array spectrometer described in the experimental system. The background subtracted emission intensities were substituted into the Boltzmann distribution and the Fe-excitation temperatures were evaluated from the slope method (Section 1.4.5). Because the lines used for the Fe-excitation measurement are all in close

Table 3.2. Fe (I) lines used for the temperature measurement and relevant spectral data [83].

Wavelength (nm)	E_p (cm^{-1})	$\log g_q f_{qp}$
372.256	27560	-1.28
373.486	33695	0.31
373.713	27167	-0.57
375.823	34329	0.00
376.379	34547	-0.19
376.719	34692	-0.34

wavelength proximity, no spectral response correction was applied for the measurement system. The Fe lines that were used along with their spectral data are listed in Table 3.2. These spectral data were taken from Bridges and Kornblith [83]. The error in these *gf* values is about 10 %.

There are several advantages to the use of a photodiode array spectrometer. One is that the blank background can be recorded and spectrally stripped from the analyte spectrum, ensuring the removal of interfering background lines. This procedure was used for the measurement of temperatures reported in this thesis. A second advantage is that the

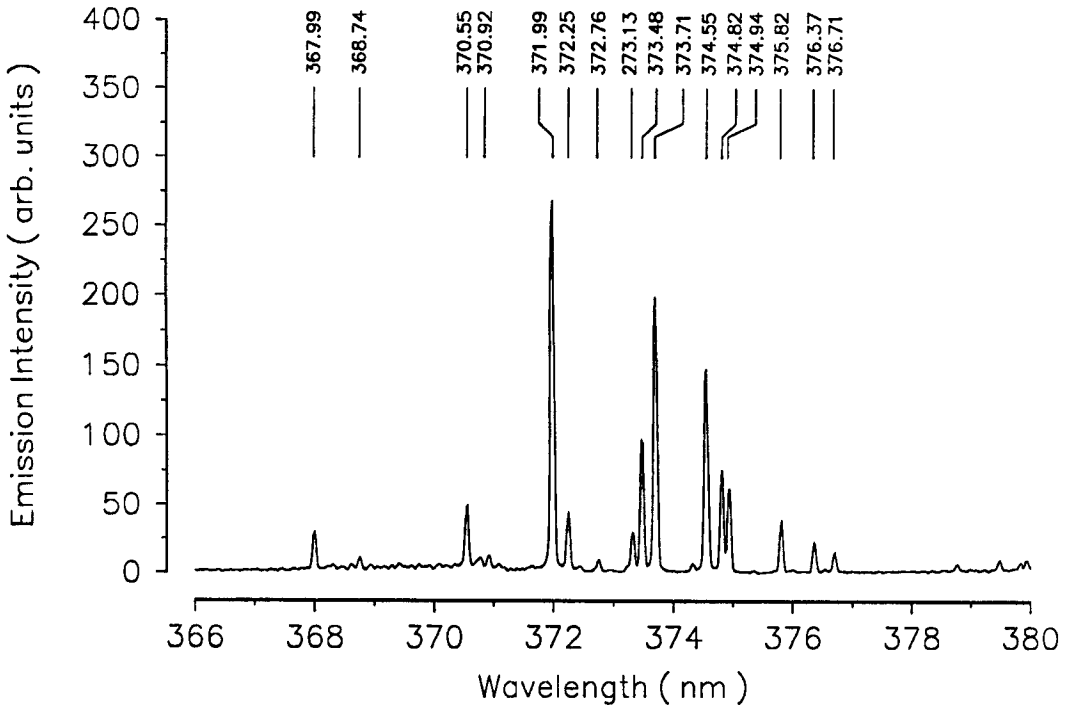

Figure 3.4. Emission spectrum for 50 ng of Fe at an RF power of 20 W.

emission from all lines is recorded simultaneously, for a single sample deposition, which significantly improves the precision, particularly for a transient signal obtained from graphite furnace methods. A typical emission spectrum of Fe at an RF power of 20 W is provided in Figure 3.4.

The variation of the Fe (I) excitation temperature with RF power is presented in Figure 3.5, which covers the RF power range 15 to 50 W. The temperatures measured, from a distance of 1 mm from the RF electrode, range from 3100 to 4200 K. The data in Figure 3.5 also demonstrate that the

temperature increases linearly with an increase in RF power over the RF power range studied. For comparison, a temperature of about 4500 K corresponds to a low flow Ar-ICP operating at a power of about 600 W [68]. It is clear that either the radiative and convective heat losses from the plasma source in FAPES are much lower than those from a ICP or the RF field strength is much higher in this RF plasma source in FAPES, or both. An excitation temperature of 2600 K was reported for thermal excitation in CFAES [84]. At an RF power of 50 W, excitation temperature of FAPES is 1600 K higher than that of CFAES. For FAPES, the Fe-excitation temperature was also measured at a different position, closer to the furnace wall. The measured temperature is 3100 ± 90 K at an RF power of 45 W. As mentioned earlier, the difference in temperature near the RF electrode relative to the furnace wall also shows that the plasma is hotter adjacent to the RF electrode. Based on the Fe-excitation temperatures, this plasma source in FAPES clearly has the potential to be a potent excitation source for atomic spectrometry.

Sturgeon *et al.* also reported several different temperatures for a 13.56 MHz helium plasma in FAPES, including Fe and He-excitation temperatures. The Fe-excitation temperature was measured using $Fe(CO)_5$, which was continuously introduced into the furnace work-head and the furnace was maintained at 970 K in order to dissociate the iron pentacarbonyl. The Fe-excitation temperature was measured only at an RF power of 100 W. Measurement at lower RF powers was not possible as a result of poor signal-to-background ratio, attributed to partial quenching of

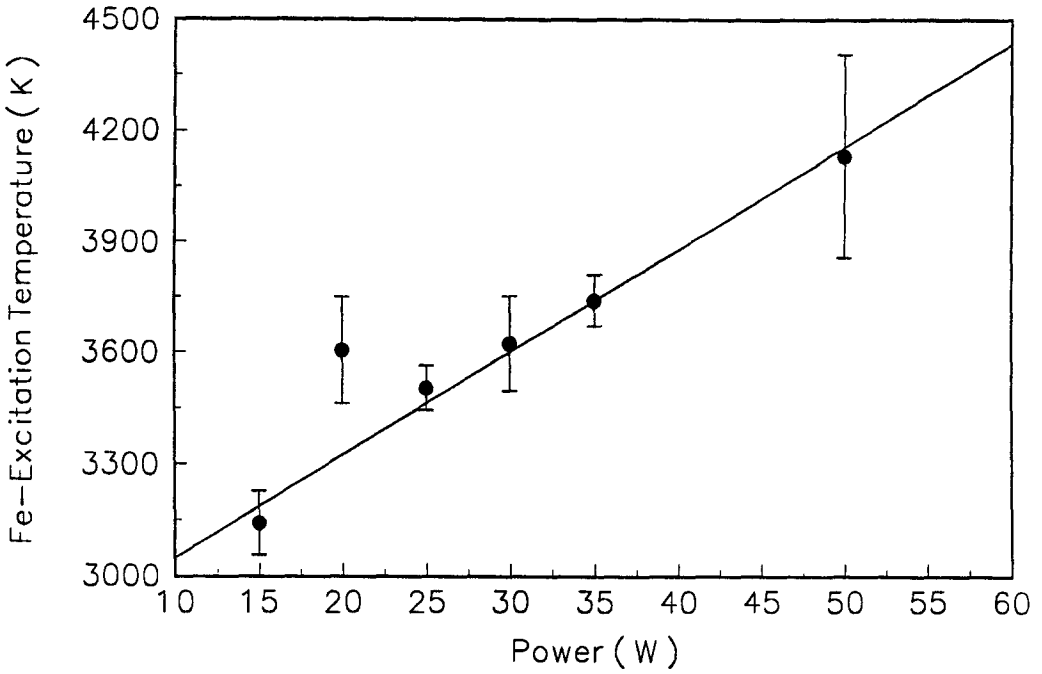

Figure 3.5. Iron excitation temperature as a function of RF power.

the plasma due to $Fe(CO)_5$ and its decomposition products. However, the He-excitation temperatures were measured at RF powers between 25 and 100 W.

The Fe-excitation temperature reported by Sturgeon *et al.* was 2920 K for a 100 W plasma [80]. For the RF plasma source described in this thesis, this temperature would correspond to an RF power of 10 W. It is unclear at this time whether the difference in Fe (I) temperature is due to variability in sources, spatial differences, or differences in the RF power coupling

efficiency. It should also be noted that the energy levels used by Sturgeon *et al.* for the Fe-excitation temperature measurements were different from those used in this thesis. In addition, the effect of the presence of excessive amounts of $Fe(CO)_5$ or CO on the excitation characteristics of the plasma source in FAPES is not known. Nevertheless, considering these differences in the temperature evaluation, the Fe-excitation temperature reported by Sturgeon *et al.* is in reasonable agreement with those reported in this thesis.

3.3.5 Atmospheric Pressure Ar Plasma

A discussion on some experimental observations of the Ar plasma source in FAPES is presented in this section.

An Ar discharge at 13.56 MHz could be ignited at powers exceeding about 30 - 40 W but would not operate in a stable manner at higher powers. If, after ignition, the power was rapidly reduced to 8 - 10 W, a diffuse Ar plasma could be maintained at 13.56 MHz. However, it has been found that it is much easier to ignite and operate an Ar plasma at 27 MHz. The ease of operation of the helium plasma can be attributed to the higher electron ionization rate of helium compared with that of Ar.

The difference in background spectral features in helium and Ar should be noted. Figure 3.6 presents the 40 nm wide wavelength window around 236 nm for the Ar plasma at 27 MHz. The intense emission from CO^+ in the

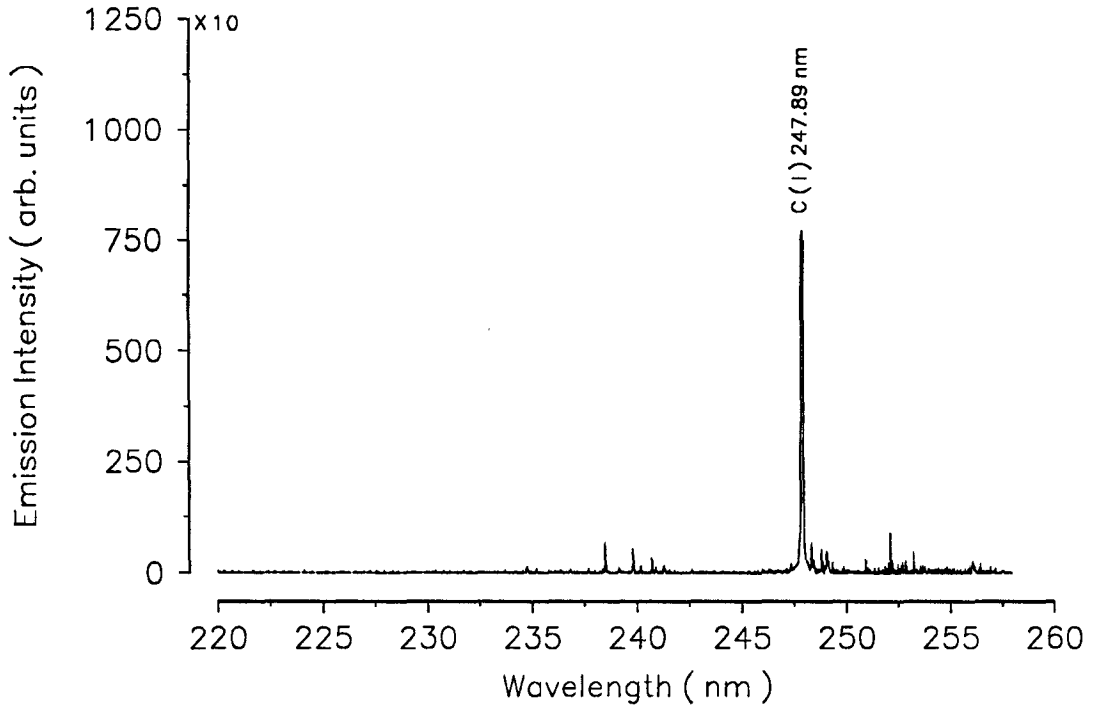

Figure 3.6. Background spectrum of the Ar plasma for the spectral region, 220 - 260 nm.

helium plasma is absent in the Ar plasma at 27 MHz. Furthermore, intense emission from C (I) at 247.89 nm can be observed in the Ar plasma compared with that in the helium plasma. This intense emission from C (I) in Ar plasma compared with that of helium plasma is likely due to the heavy Ar ion bombardment on the RF electrode, higher temperature of the Ar plasma, or both. Sturgeon *et al.* also reported the presence of C (I) line at 247.85 nm in the Ar plasma, but not in the helium plasma [78,79].

3.4 SUMMARY

Some basic characteristics of the atmospheric pressure helium plasma source at 13.56 MHz in FAPES are presented and discussed in this chapter. Background emission spectra for the wavelength region, 200 - 500 nm, are dominated by emission features from CO^+, OH, NH, N_2^+, and N_2. The emission features of CO^+ and N_2^+ indicate that this plasma source is capable of exciting energy levels as high as 20 eV, and the energy transfer mechanism in this case is near-resonant charge transfer.

Background emission is most intense near the RF electrode and less intense near the furnace wall. The intense emission near the RF electrode is likely due to a difference in RF field strengths at the RF electrode and at the furnace wall. The higher RF field strength at the RF electrode leads to a high energetic excitation region adjacent to the RF electrode compared with that adjacent to the furnace wall.

Time-resolved studies show complex emission characteristics for plasma emission features during the atomization step. This complex emission behavior of the molecular species is indicative of the evolution of thermionic electrons from the RF electrode during the high temperature atomization step. The time-averaged Fe (I) excitation temperature for the 13.56 MHz helium plasma source is in the range, 3100 - 4200 K, for RF powers between 15 and 50 W. The Fe-excitation temperatures also show a spatial dependence and a higher temperature is observed adjacent to the

RF electrode. These Fe-excitation temperatures show that the FAPES source has the potential to be a potent excitation source for atomic spectrometry.

As is the case with most spectrochemical plasma sources, this RF plasma source is spatially non-homogeneous and shows a strong excitation region near the RF electrode. Because the plasma source is spatially non-homogeneous, care must be exercised in the measurement and comparison of fundamental and analytical characteristics as they may be spatially dependent.

CHAPTER 4

TEMPORAL EMISSION AND ABSORPTION CHARACTERISTICS OF SILVER, LEAD, AND MANGANESE IN FAPES

4.1 INTRODUCTION

The temporal response of the analyte absorption signal is an important diagnostic tool in GFAAS, and has often been combined with kinetic and thermodynamic calculations to determine the analyte atomization mechanisms during the high temperature atomization step of the analyte [85-88]. Under temporally non-isothermal conditions, temporal response of the analyte signal is also an important factor that affects the figures of merit and matrix effects for analytical determinations by GFAAS [44,89].

The temporal response of the analyte signal in FAPES is likely different from that in GFAAS due to three primary reasons. Firstly, the atomization characteristics of analytes in FAPES may be different from those in GFAAS because of the plasma inside the graphite furnace. The plasma may affect atom-formation processes through participation in the equilibria for condensed and gas-phase species. Gas-phase concentrations of different species that affect the atomization characteristics of analytes may be

different with the plasma inside the graphite furnace compared with those without the plasma. Secondly, the vaporization characteristics of analytes in FAPES may be different from those in GFAAS because of the RF electrode inside the graphite furnace. The RF electrode can act as a second-surface, where analytes can condense and then vaporize to form a second peak. Thirdly, if the excitation characteristics change during the high temperature atomization step of the analyte, then the temporal response of the analyte signal in FAPES would be different from that in GFAAS. In this case, the temporal response of the analyte signal is determined not only by atomization and vaporization characteristics of the analyte but also by excitation characteristics of the analyte in the plasma.

Smith *et al.* reported double peaks for Ag at high analyte amounts and low RF powers, and speculated that the appearance of double peaks was due to the atomization characteristics of Ag in FAPES [17]. Sturgeon *et al.* reported the appearance of double peaks for Cd at low RF powers in FAPES [16]. In addition, an early shift in the position of peak maximum for Cd, Cu, Ni, and Be, and no shift for Fe, Pb, P, and Bi were observed with increasing RF power [78]. Sturgeon *et al.* suggested that these observed shifts were due to the increased plasma volume and density which occur with increasing RF power, more efficient excitation *via* electron collision, possible changes in the actual observation zone, and reduced self-absorption in the larger, hotter plasma [78]. For HA-FANES, Riby *et al.* reported two unresolved peaks for Cr, and suggested that Cr condensation on the electrode was the origin of these two peaks [90].

In an effort to understand the temporal response of the analyte signal in FAPES, a study of time-resolved atomic absorption and atomic emission was undertaken. This chapter presents the results of this study for Ag, Pb, and Mn. Effects of the plasma and the RF electrode on analyte atomization and vaporization characteristics are discussed. In addition, effects of the plasma excitation process on the temporal response of analyte signal during the analyte atomization and vaporization are presented. The work described in this chapter has been previously published by Hettipathirana and Blades [71].

4.2. EXPERIMENTAL

A complete description of the experimental system employed to acquire simultaneous atomic absorption and atomic emission signals is given in Chapter 2 of this thesis. This experimental system and a vertical-mount for the RF electrode were employed. The following experimental methods and parameters should be noted.

4.2.1 Signal Presentation

Four replicate measurements were averaged and subjected to a 25-point Savitzky-Golay smoothing procedure [91]. Analytical parameters, such as absorbance, peak area, and peak width, were calculated for each sample deposition.

4.2.2 Appearance and Peak Temperatures

The appearance temperatures of analytes were calculated based on their appearance times and the temperature-time profile of the graphite furnace (also see Section 2.1.6). The appearance time was defined as the time taken for the absorbance or the emission signal to reach the average base line plus two standard deviations of the base line noise. The repeatability in determining the appearance temperature was less than 1.5 %. The peak temperature was defined as the temperature at which maximum absorption or emission occurs.

4.2.3 Reagents

All analyte solutions in 1 % (v/v) HNO_3 were prepared from serial dilution of 1000 mg L^{-1} stock solutions prior to analysis. Silver, Pb, and Mn solutions were prepared by dissolving analytical grade $AgNO_3$ and $Pb(NO_3)_2$ (both, BDH, Toronto, Canada), and reagent grade $MnSO_4.H_2O$ (MCB, Ohio, USA). Nitric acid solutions were prepared by using the analytical grade reagent (BDH, Toronto, Canada).

4.2.4 Procedure

A 5 μL aliquot of analyte solution was deposited onto the furnace side wall or on the RF electrode by employing an Eppendorf 0.5 - 10 μL UltraMicro pipette. The plasma source work-head was purged with helium (Union Carbide, Toronto, Canada). The furnace temperature was increased to 470 K

in 45 s to dry, and was maintained at 470 K for another 45 s to ash the sample. This total time interval was sufficient to exclude the water vapor inside the plasma source work-head before plasma ignition. Within the next 10 s lag time, the plasma was ignited. After this lag time, the furnace temperature was ramped to 2050 K in 5 s for all determinations. After each sample atomization step, a dry (without deposition) atomization step was carried out to clean the graphite furnace. Four replicate measurements were carried out for each determination. The blank determinations were carried out by depositing the same amount of 1 % (v/v) HNO_3 solution.

All determinations were carried out by using atomic resonance lines of Ag (328.07 nm), Pb (283.30 nm), and Mn (279.28 nm).

4.3 Results and Discussion

Experiments where atomic absorption is measured without the plasma, are referred to as " AA at an RF power of 0 W " in this chapter. For those experiments, the RF electrode is referred to as the " co-axial rod ". When atomic absorption is measured with the plasma, the corresponding RF power will be specified. The RF electrode is a graphite rod unless otherwise noted. It should also be noted that all specified masses of analytes are from their corresponding salts dissolved in 1 % HNO_3.

4.3.1 Silver

The effect of a graphite co-axial graphite rod on the atomic absorption signal was studied by depositing the analyte sample on the furnace wall and the temporal response was recorded with and without the co-axial graphite rod installed (AA at an RF power of 0 W). The results of this experiment, when 0.5 ng of Ag is deposited on the furnace wall, are given in Figure 4.1.

When the sample is deposited on the furnace wall without the co-axial graphite rod, a peak with an appearance temperature of 1130 K and a peak temperature of 1430 K is observed (solid line). When the sample is deposited on the furnace wall with the co-axial graphite rod installed (dash line), two peaks are observed. The first is a very small peak with an appearance temperature of 1240 K and a peak temperature of 1400 K. The second more intense peak has an apparent peak temperature of 1680 K. Different amounts of sample deposited on the wall result in a constant peak ratio for these two peaks. These observations suggest that the co-axial rod acts as a condensation site for species vaporized from the furnace wall with subsequent " second-surface " vaporization from the co-axial rod. The small size of the initial peak as compared with the second peak shows that the condensation is essentially instantaneous. The delay in the onset of the larger absorbance signal when the co-axial rod is installed is the result of delayed heating of the co-axial rod relative to the furnace wall, somewhat similar to the situation encountered during the radiant heating of a L'vov platform.

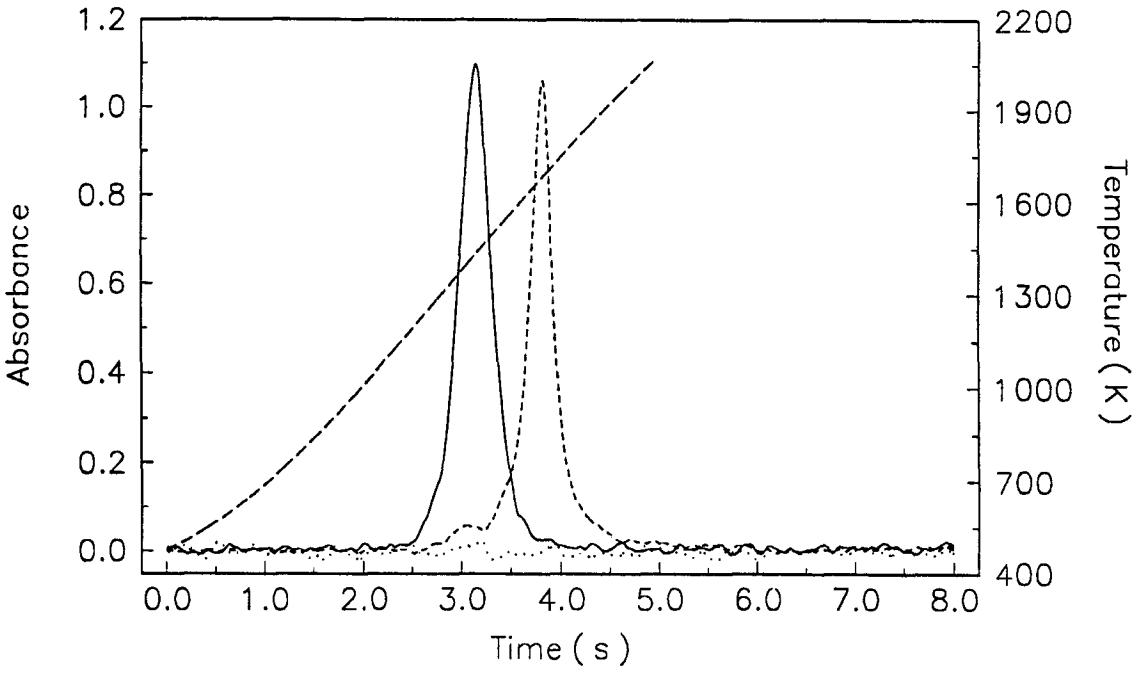

Figure 4.1. Temporal response of the Ag atomic absorption signal at an RF power of 0 W for 0.5 ng of Ag deposited on the furnace wall with (- - -) and without (——) the graphite co-axial rod; background (• • •); and the temperature profile of the furnace wall (— — —).

The process in which the cooler surfaces inside the graphite furnace act as condensation sites for analytes vaporized from the furnace wall is consistent with recent studies reported for GFAAS [92,93]. L'vov *et al.* observed double peaks when the sample was deposited on the furnace wall with a platform inside the furnace [92]. Hocquellet employed a " second-surface trap " inside the furnace to condense the analyte vaporizing from the furnace wall and

then to vaporize later in the atomization step to achieve the temporal isothermality [93].

The temperature difference between the furnace wall and the co-axial rod, and the effect of graphite on the atomization process for Ag were studied by depositing 0.5 ng of Ag on co-axial rods of graphite and tungsten (AA at an RF power of 0 W). The results of this experiment for deposition on the graphite rod (solid line) and tungsten rod (dash line) are given in Figure 4.2. Except for the small difference in the appearance temperatures (and the peak temperatures), identical peak shapes are observed for samples deposited on graphite and tungsten rods. These differences in temperatures are probably due to the difference in radiant heating rates for these two types of co-axial rods.

The time difference of 1.2 s in the appearance of the atomic absorption signal for the sample deposited on the furnace wall without the graphite co-axial rod (solid line, Figures 4.1) and that for the sample deposited on the graphite co-axial rod (solid line, Figure 4.2) demonstrates that there is an appreciable temperature difference in the temperature-time profiles for the furnace wall and the co-axial rod. In addition, there is a difference in the peak time for the Ag signal from the second-surface vaporization (dash line, Figure 4.1) and the direct deposition of Ag on the graphite co-axial rod (solid line, Figure 4.2). Silver deposited directly on the co-axial rod appears later in time. This time difference is likely due to a difference in the temperature-time characteristics between second surface vaporization sites

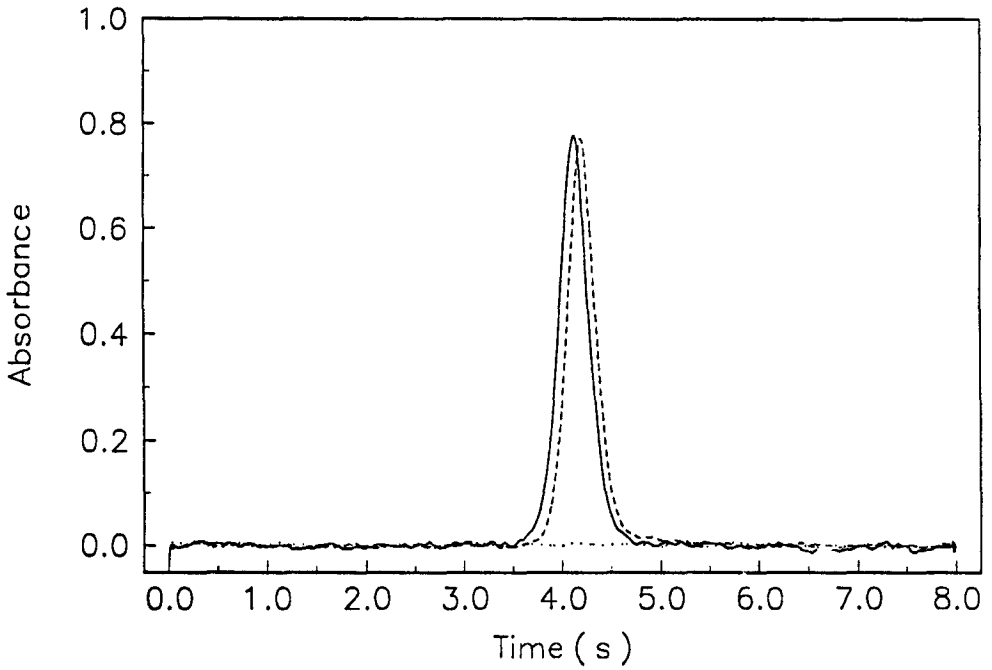

Figure 4.2. Temporal response of the Ag atomic absorption signal at an RF power of 0 W for 0.5 ng of Ag deposited on the graphite co-axial rod (———) and tungsten co-axial rod (- - -); and background (· · ·).

on the co-axial rod and the sample deposition site on the co-axial rod. There is no doubt that the co-axial electrode does not heat uniformly and it is likely that the RF connector end of the co-axial rod is cooler than the rest. Unfortunately, getting an accurate spatially resolved measurement of the co-axial rod temperature by itself without collecting scattered radiation from the furnace wall is very difficult.

The identical peak shape of signals, from the deposition on both graphite and tungsten rods (Figure 4.2), is consistent with the atom-formation mechanism for Ag in GFAAS. The accepted mechanism of Ag atom-formation in GFAAS is the direct thermal dissociation of the oxide and volatilization of the metal [94]. The calculated distribution of species as a function of temperature shows that, Ag exists primarily as metallic Ag on the furnace wall at temperatures below 1075 K, and sublimes to form gas-phase Ag above 1075 K [94]. Thermogravimetric studies indicate that $AgNO_3$ decomposes at 880 K to form the oxide [95]. Silver oxide decomposes at about 615 K to form metallic Ag [95].

Figure 4.3 provides the results of a FAPES study in which 0.5 ng of Ag is deposited both on the furnace wall (solid line) and on the RF electrode (dash line) at an RF power of 20 W. The emission peak for the sample deposited on the furnace wall (peak width of 500 ms) has an appearance temperature of 1170 K and a peak temperature of 1410 K. The sample deposited on the RF electrode results in a broader peak (peak width of 750 ms) with an apparent appearance temperature of 1160 K and a peak temperature of 1460 K. The early appearance of the emission signal when the sample is deposited on the RF electrode indicates that the temperature of the sample deposition site of the RF electrode may be slightly hotter than the furnace wall. The emission profile for the sample deposited on the RF electrode has more signal after the initial appearance, which could result from a difference in the temperature-time characteristics of the RF electrode or the initial vaporization of Ag into the more energetic excitation region

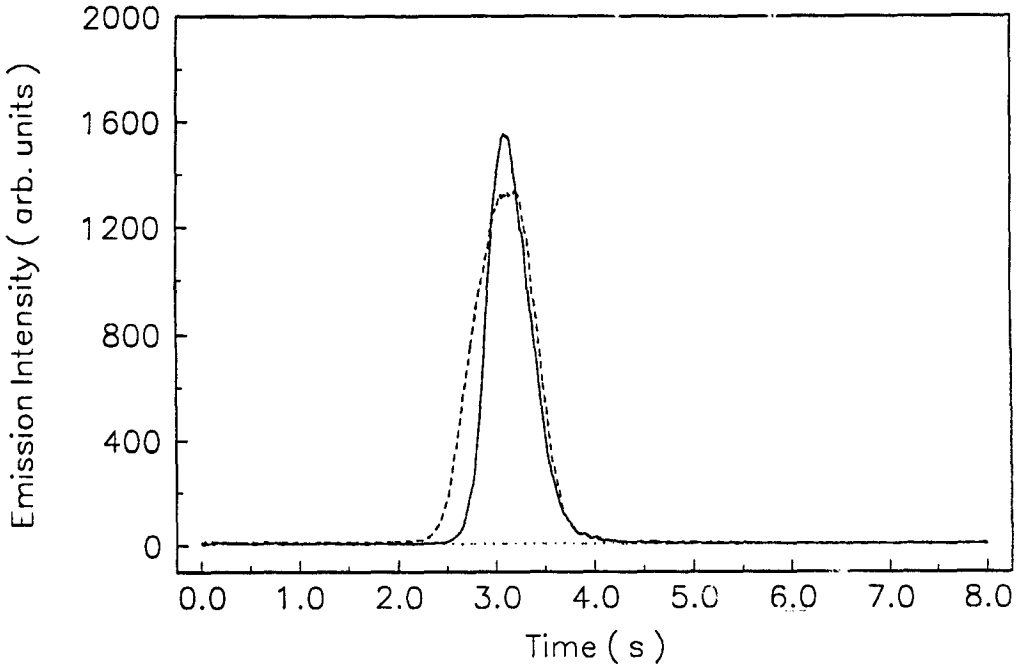

Figure 4.3. Temporal response of the Ag atomic emission signal at an RF power of 20 W for 0.5 ng of Ag deposited on the furnace wall (——) and RF electrode (- - -); and background (· · ·).

adjacent to the RF electrode. The tailing edges of the two peaks in Figure 4.3 are identical, indicating similar atom dissipation processes.

The difference in appearance time between the atomic absorption signal when the sample is deposited on the co-axial rod (solid line, Figure 4.2) and the atomic emission signal when the sample is deposited on the RF electrode (dash line, Figure 4.3) is about 1.4 s, indicating that the temperature of the RF electrode is higher when compared with that without

the plasma. The difference in appearance time between the atomic absorption signal (solid line, Figure 4.1) and the atomic emission signal (solid line, Figure 4.3) when the sample is deposited on the furnace wall, is 100 ms and indicates that there is probably no appreciable difference in the temperature of the inside furnace wall with and without a plasma at 20 W.

The effect of the amount of Ag on the emission signal for FAPES is provided in Figure 4.4. As the amount of Ag increases from 0.05 to 0.5 ng, the peak temperature increases by about 120 K, the appearance temperature decreases by about 60 K, and the peak width increases from 400 to 610 ms. However, the peak for 5 ng (long-dash line) is shifted to higher peak and appearance temperatures compared with those for 0.05 ng, and its peak width is 360 ms. With the exception of the signal for 5 ng Ag, these observations are consistent with those observed for Ag in GFAAS [96,97]. The most significant difference in temporal behavior as a function of the amount of Ag is that the deposition of 5 ng of Ag resulted in a second peak at a later time. However, this peak disappeared when the RF power coupled to the plasma was increased from 20 to 30 W. The formation of a second peak at a higher deposited amount can be attributed to the second-surface vaporization of Ag which condenses on the cooler areas of the RF electrode. As pointed out earlier, the RF electrode may not heat uniformly and it is likely that the RF connector end of the electrode is cooler than the rest.

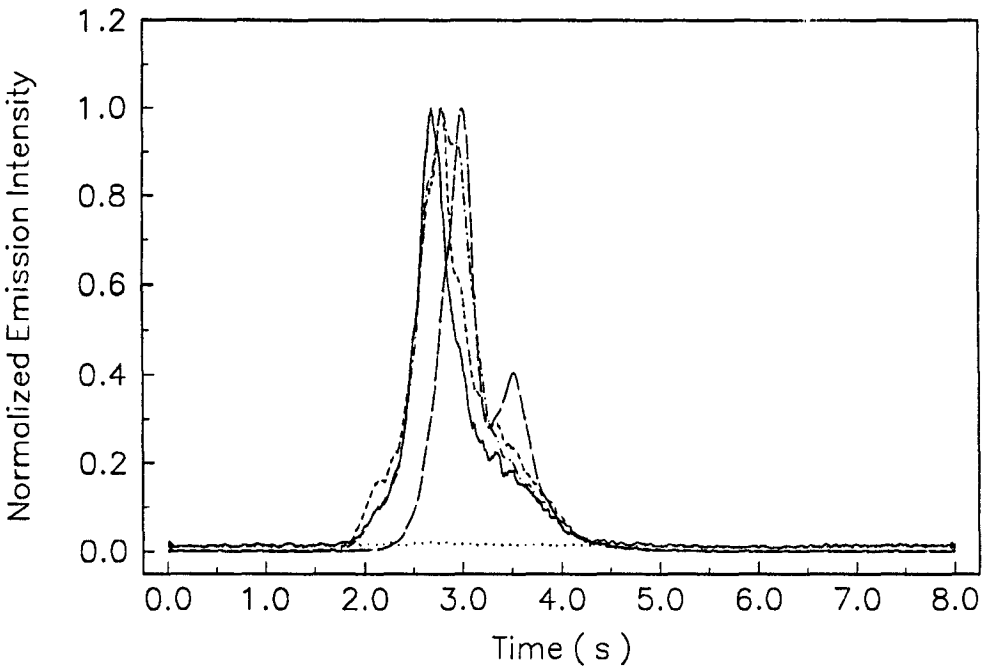

Figure 4.4. Temporal response of the Ag atomic emission signal at an RF power of 20 W for Ag deposited on the furnace wall. Analyte amounts: 0.05 (———), 0.25 (- - -), 0.50 (- · - · -), and 5.0 ng (— — —); and background (· · ·) at 20 W.

The results of a study on the effect of changes in RF power on the emission signal for 0.5 ng of Ag deposited on the furnace wall is provided in Figure 4.5. The most significant observations are: (a) the apparent appearance temperature decreases from 1220 K at 14 W to 940 K at 38 W, (b) the peak temperature decreases by about 130 K as the RF power is increased, (c) the peak area increases as the RF power is increased, and (d) the peak width increases from 480 ms at 14 W to 670 ms at 38 W.

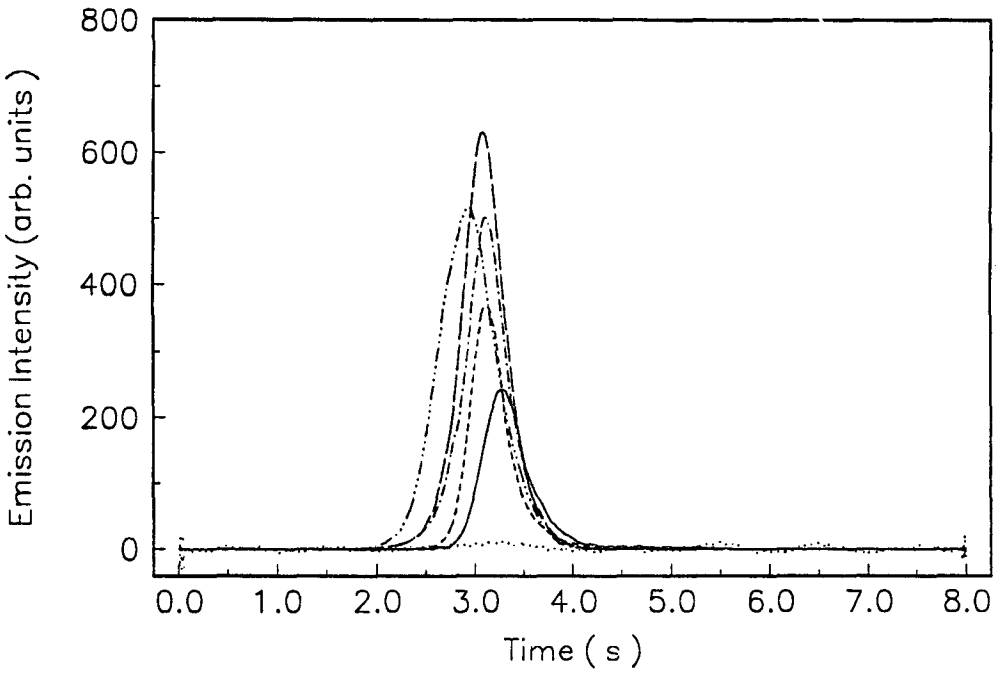

Figure 4.5. Temporal response of the Ag atomic emission signal for 0.5 ng of Ag deposited on the furnace wall at an RF power of 14 (——), 20 (- - -), 26 (- • - • -), 32 (— — —), and 38 W (- ··· - ···); and background at 20 W (· · ·).

These emission characteristics shown in Figure 4.5 were investigated by simultaneous measurement of atomic absorption and atomic emission signals. The temporal response of the atomic absorption signal for 0.5 ng of Ag, measured at an RF power of 20 (solid line) and 40 W (dash line), is given in Figure 4.6. For clarity, only absorption signals are given. The most significant observation is that not only the emission signal but also the atomic absorption signal is shifted to earlier times when the RF power is

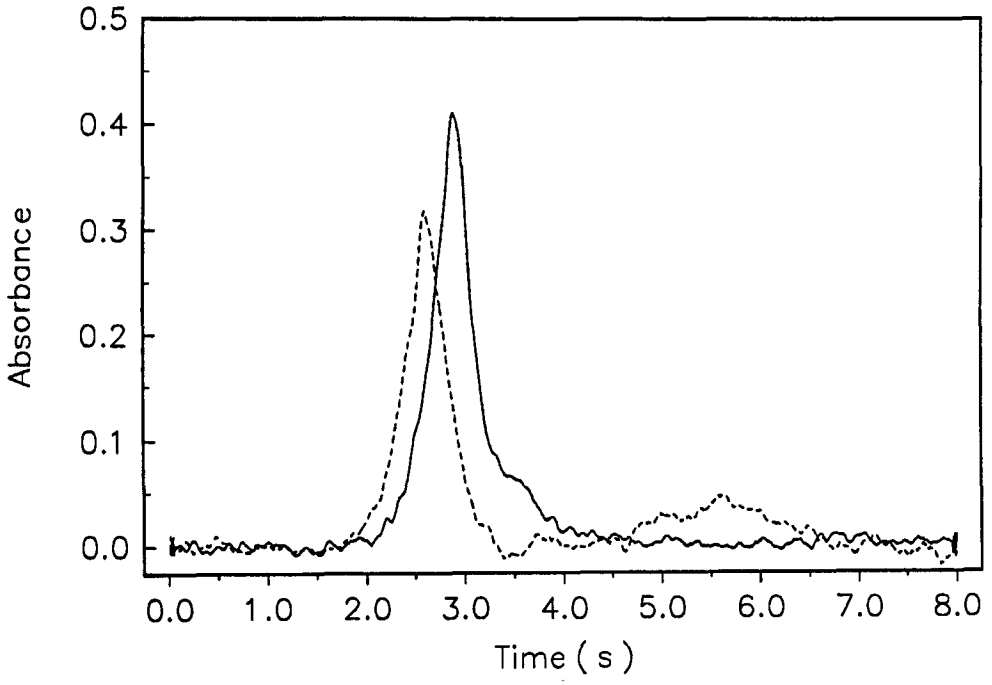

Figure 4.6. Temporal response of the Ag atomic absorption signal for 0.5 ng of Ag deposited on the furnace wall at an RF power of 20 (—) and 40 W (- -).

increased. In contrast to peak area of the atomic emission signal (Figure 4.5), that of the atomic absorption signal (Figure 4.6) decreases when the RF power is changed from 20 to 40 W. However, peak width of the atomic absorption signal increases only marginally (about 50 ms).

The observed shifts in both atomic emission (Figure 4.5) and atomic absorption (Figure 4.6) signals as the RF power is increased may be due to an increased evaporation rate of Ag from the furnace wall when the plasma is

present [98]. It is also possible to have some plasma-assisted heating of the surface of the furnace wall at high RF powers. However, it should be noted here that Pb (Section 4.3.2) and Mn (Section 4.3.3) do not show a significant change in the peak temperature as RF power is increased within the same range. The decrease in peak area of the Ag absorption signal is probably due to an increase in evaporation loss of Ag. However, this effect cannot be seen from the emission signal because of the increase in excitation when the RF power is increased.

4.3.2 Lead

Lead has been widely studied and, judging by reports in the literature, has been the subject of some controversy. Double peaks and temporal shifts of the absorbance signal for Pb in GFAAS in the presence of sample contaminants and different gaseous contaminants have been reported by many authors. These double peaks and temporal shifts have been attributed to different chemical forms [99], condensation and vaporization from the furnace wall [43,100], effects of chemisorbed oxygen on the furnace wall [101], gas-phase dissociation of the oxide [102], and formation of a pyrolytic-graphite layer on non-pyrolytic graphite furnace wall [103].

In order to study the effect of the graphite co-axial rod on the atomic absorption signal for Pb, 5 ng of Pb was deposited on the furnace wall and the response was recorded with and without the co-axial rod installed, an experiment analogous to Ag experiments (AA at an RF power of 0 W). The

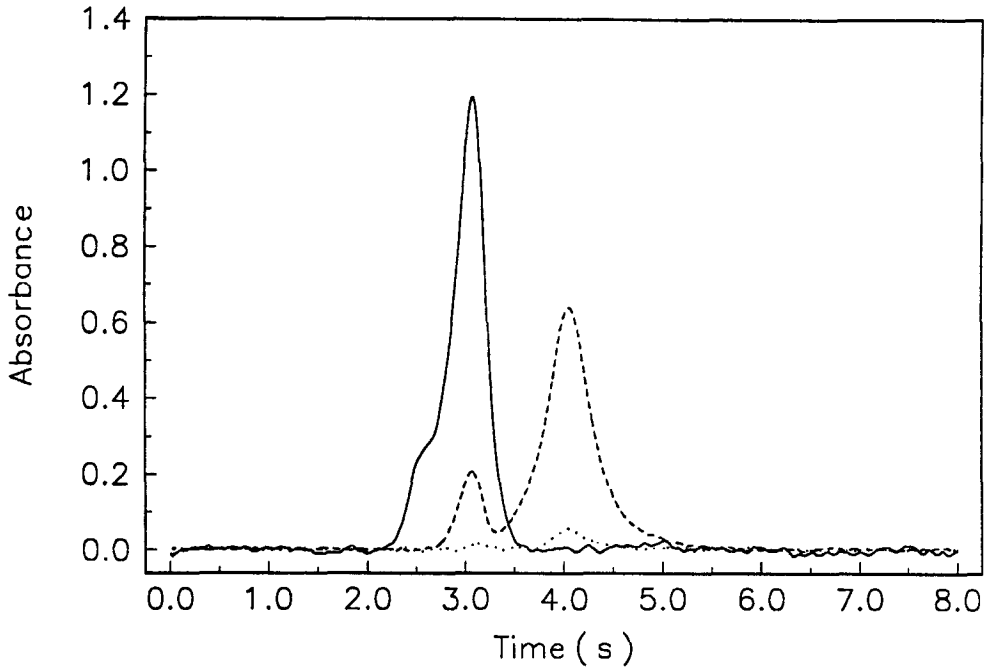

Figure 4.7. Temporal response of the Pb atomic absorption signal at an RF power of 0 W for 5 ng of Pb deposited on the furnace wall with (- - -) and without (——) the co-axial rod; and background (• • •).

results are shown in Figure 4.7. The atomic absorption signal of the sample deposited on the furnace wall without the co-axial rod (solid line) is a composite of two closely spaced peaks, a smaller peak that appears on the leading edge of the signal that has an appearance temperature of 1080 K, and a much larger peak with a peak temperature of 1400 K. The atomic absorption signal of sample deposited on the furnace wall with the co-axial rod installed (dash line), shows two peaks with an appearance temperature

of 1220 K for the first peak. The first, less intense peak has a peak temperature of 1400 K and the second, more intense peak has an apparent peak temperature of 1770 K. This, broad, second peak has a width of 500 ms. The response for Pb with the co-axial rod installed is consistent with the process involving initial vaporization from the furnace wall, condensation on the co-axial rod, and subsequent second-surface vaporization from the co-axial rod as it heats with a time lag relative to the furnace wall. The relative intensity of the early peak to that of the latter peak is quite different from that observed for Ag. This is probably the result of different values of sticking coefficients for Ag, Pb, and PbO on graphite.

Currently it is believed that Pb can be produced through either reduction of PbO by carbon to form gas-phase Pb and CO, or through direct vaporization of PbO and subsequent dissociation to form Pb and O_2. For GFAAS, Campbell and Ottaway calculated an appearance temperature of 1000-1100 K based on the reduction of PbO by carbon, and observed an appearance temperature of 1000 K [104]. The combined thermodynamic and kinetic calculations carried out by Sturgeon *et al.* showed reduction of PbO by carbon and dissociation of gas-phase Pb_2 to form Pb [105]. The experimental appearance temperature reported by these authors was 1040 K [105]. Frech *et al.* calculated the distribution of Pb as a function of temperature and showed the existence of both gaseous Pb and PbO at temperatures around 900 K [94]. Suzuki *et al.* calculated the atomization energies for Pb in a molybdenum microtube atomizer and suggested gas-phase thermal dissociation of PbO to form Pb with an appearance temperature of

1270 K [106]. The gas-phase dissociation of PbO was also reported by Gilchrist *et al.* [102,107]. The presence of PbO and Pb during the atomization of GFAAS was established by mass spectral studies [108,109]. In a mass spectrometric study to determine the dissociation energy of PbO, gas-phase PbO was observed at 1000 - 1150 K from the vaporization of PbO [110]. Regardless of the diverse atom-formation mechanisms suggested, the average appearance temperature reported by five authors was 1060 K [43].

It is possible that the initial peak shown in Figure 4.7, when the sample is deposited on the furnace wall without the RF electrode (solid line), is the result of Pb formed from PbO reduction by carbon and the latter, more intense peak, results from direct vaporization and subsequent dissociation of PbO in the gas-phase. Some supporting evidence for this hypothesis is provided in Figure 4.8 which provides the results of an atomic absorption experiment (AA at an RF power of 0 W) in which 5 ng of Pb is deposited on both graphite (solid line) and tungsten (dash line) co-axial rods. The apparent appearance time was shifted later in time by about 400 ms (about 115 ms for Ag) when the sample was deposited on the metal rod relative to the graphite rod. However, the difference in peak times is about 70 ms (about 60 ms for Ag). The peak width of the sample deposited on the metal rod (360 ms) is less than that on the graphite rod (480 ms). It should be noted that it is quite probable that the heating rates for the two co-axial rods are different and the differing peak times are a reflection of this effect. Nevertheless, the signal for deposition on the graphite co-axial rod appears to be a composite of two peaks, similar to the shape seen in Figure 4.7 when the

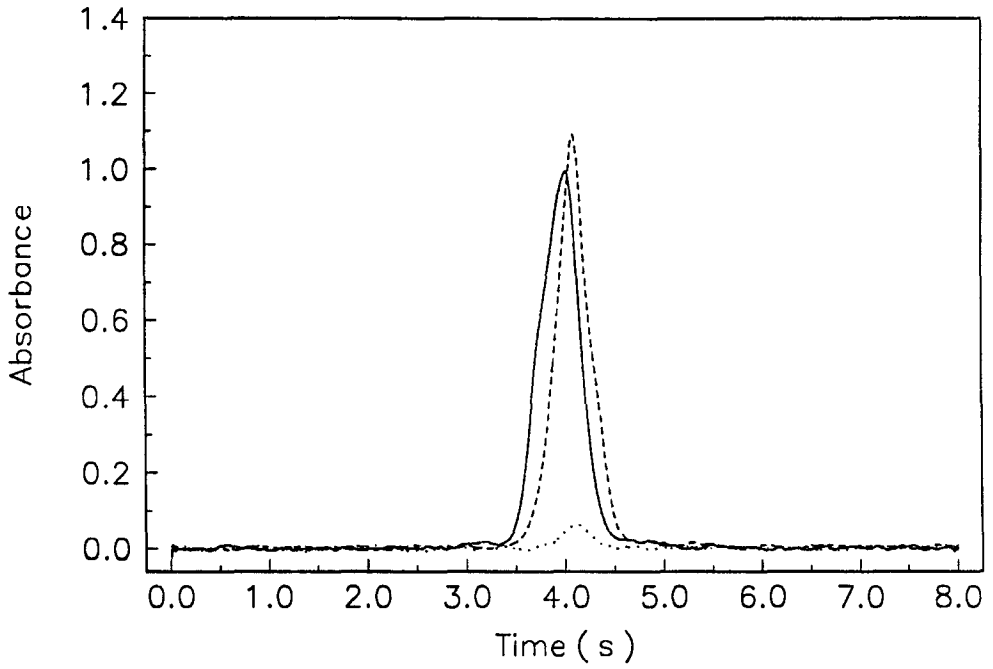

Figure 4.8. Temporal response of the Pb atomic absorption signal at an RF power of 0 W for 5 ng of Pb deposited on the graphite co-axial rod (——) and tungsten co-axial rod (- - -); and background (• • •).

sample is deposited on the furnace wall (solid line), although much less well defined. In contrast, the signal from the metal rod appears to be a single well-defined peak. The falling edges of the two peaks are identical.

The appearance of a shoulder on the rising edge of the Pb signal from the graphite surface (solid line, Figures 4.8) also shows that atomization from the graphite surface is due to more than one mechanism. However, the mechanism of early Pb release is absent for the tungsten rod (dash line,

Figure 4.8). This observation is consistent with an initial release of Pb through reduction of PbO by carbon to form the gas-phase Pb and CO. The larger peak, obtained from the tungsten rod, corresponds to direct vaporization and subsequent dissociation of PbO in the gas-phase.

The second peak in Figure 4.7 (with the co-axial rod installed, dash line) has a slowly rising edge compared with the peak from the furnace wall without the co-axial rod (solid line). This difference in the rising edge shows a difference between initial vaporization from the first-surface (furnace wall) and subsequent vaporization from the second-surface (co-axial rod). If the initial slow reduction of PbO by carbon on the furnace wall at the appearance temperature (shoulder in the rising edge of the signal) and the vaporization of PbO with subsequent dissociation in the gas-phase (the peak with the maximum absorbance) take place, then second-surface vaporization from the co-axial rod is most probably in the form of PbO rather than Pb. Lead oxide vaporized from the co-axial rod should undergo rapid dissociation in the gas-phase because the temperature of the gas-phase at this time is high compared with initial vaporization from the furnace wall. However, condensation of PbO on the co-axial rod should produce an increase in the surface coverage compared with initial deposition of the sample on the furnace wall and a concurrent increase in the graphite-PbO interaction. This increased surface coverage and the temperature non-uniformity of the co-axial rod may be the reason for the broad peak width and slowly rising and falling edges of the Pb signal for the second-surface vaporization from the co-axial rod. Furthermore, the similar shape of the rising and falling edges of

the second peak when the sample is deposited on the furnace wall with the co-axial rod indicates the continued generation of Pb even after the peak temperature is reached.

Figure 4.9 provides the emission signal for 5 ng of Pb deposited on the furnace wall (solid line) and on the RF electrode (dash line), and 0.5 ng of Pb deposited on the furnace wall (dash-dot line). The signal for 0.5 ng of Pb is plotted at 10 times the actual peak height. Compared with Ag, Pb shows quite complex temporal behavior in FAPES. With respect to the emission signal for 0.5 ng of Pb deposited on the furnace wall, the appearance time is much earlier than the atomic absorption signal without the co-axial rod (solid line, Figure 4.7). This is in contrast to the results obtained for Ag. In addition, the emission signals in Figure 4.9 show a close similarity of peak times for samples deposited on the furnace wall and on the RF electrode. Another feature of the data shown in Figure 4.9 is that, when 5 ng of Pb is deposited, a second broad peak is observed between 2.5 and 4 s and this peak appears whether Pb is deposited on the furnace wall or on the RF electrode. It seems that the temperature of the sample deposition site of the RF electrode and that of the furnace wall are similar at this instance, and hence, Pb species can condense on the cooler areas of the RF electrode regardless of the initial sample deposition site. As mentioned earlier (Section 4.3.1), the RF connector end of the electrode can be cooler than the rest, even in the presence of the plasma.

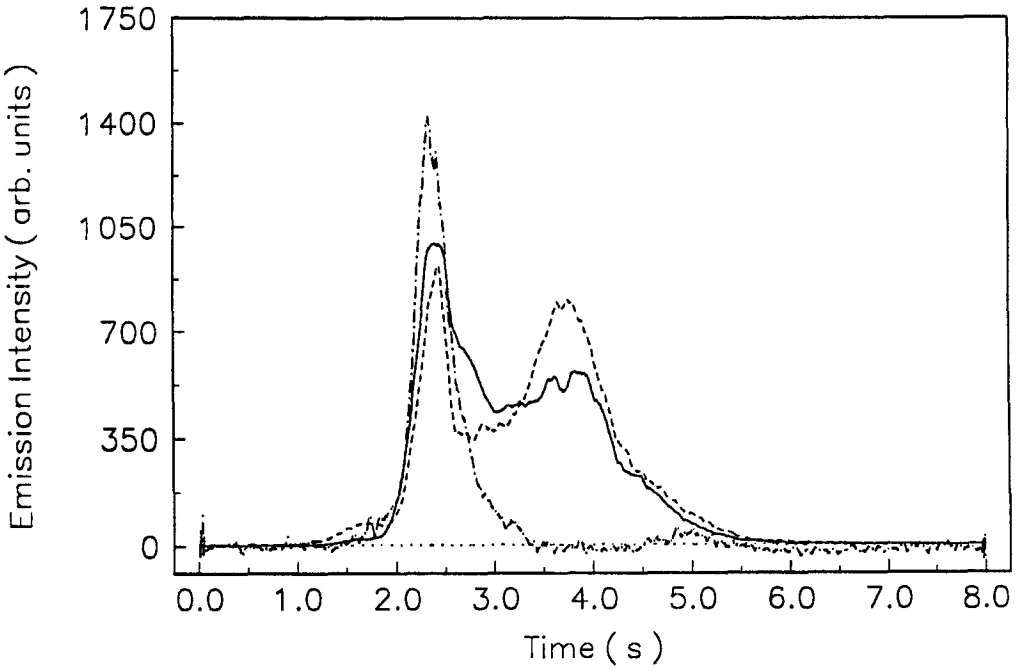

Figure 4.9. Temporal response of the Pb atomic emission signal at an RF power of 20 W for 5 ng of Pb deposited on the furnace wall (——) and RF electrode (- - -), 0.5 ng of Pb deposited on the furnace wall (-·-·-, × 10); and background at 20 W (· · ·).

Some supporting evidence for the condensation of Pb species on the RF electrode is given in Figure 4.10, where absorbance is plotted as a function of RF power. The total absorbance for both peaks (1 - 5 s) does not change significantly, but the absorbance for the first peak (1 - 3 s) increases as the RF power increases. The increase in absorbance for the first peak, and hence, a decrease in absorbance for the second peak are due to reduced condensation PbO on the RF electrode when the RF power is increased. A

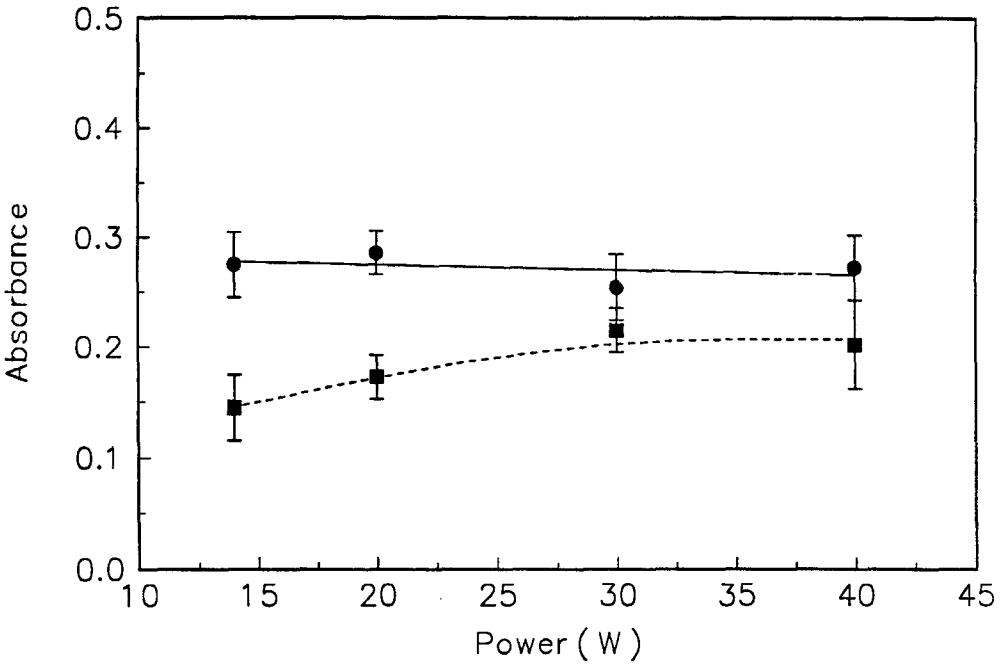

Figure 4.10. Atomic absorbance for 5 ng of Pb deposited on the furnace wall as a function of RF power: for 1 - 5 (●), and 1 - 3 s (■).

similar situation cannot be seen from the emission experiment (see Figure 4.11) because of the increased excitation with increasing RF power.

The lowering or increasing appearance temperature of Pb has been well-documented in GFAAS literature. McLaren and Wheeler [99] and Imai and Hayashi [103] reported peak doubling in the presence of 1% (w/v) ascorbic acid and the appearance of an early peak. In the latter study, no significant difference in appearance temperatures was observed when pyrolytic-graphite-coated graphite was used, but the appearance temperature

decreases from 1130 to 1030 K when 1% (w/v) ascorbic acid was present (corresponding peak temperatures are 1510 and 1250 K, respectively). Salmon *et al.* [101], and Sturgeon and Berman [111] observed a late time shift of Pb signal when O_2 was added to the sheathing gas. Cendergren *et al.* reported an early time shift and doubling of Pb signal when CO was used as the purge gas [112]. A mass spectral and atomic absorption study by Bass and Holcombe showed that the early appearance of Pb from oxygenated surface was due to increased CO concentrations in the gas-phase [113]. Bass and Holcombe attributed the effect of CO to the heterogeneous equilibrium of PbO on the surface and the gas-phase Pb, CO and CO_2 [113]. A study by Gilchrist *et al.* showed appreciable amounts of CO when ascorbic acid was used with slow heating rates [114]. In another study, Gilchrist *et al.* reported an early time shift of signal by adding H_2 and CO to the purge gas [102]. They reported a decrease in appearance temperature of Pb from 1110 to 840 K when 2.1 % (v/v) CO was added to the purge gas. This was attributed to the gas-phase equilibrium involving dissociation of PbO to form Pb and O_2. In summary, these GFAAS studies show that the atomization of Pb is strongly affected by the gas-phase composition, especially by the amount of CO in the gas-phase.

It is quite possible that the presence of higher amounts of CO in the plasma shifts the appearance temperature of Pb in FAPES (Figure 4.9) compared with that without the plasma (Figure 4.7). At present, calculated or experimentally determined partial pressures of CO and O_2 have not been reported for FAPES. However, Sturgeon *et al.* reported the presence of CO in

the RF plasma source at 13.56 MHz [78]. In addition, CO^+ emission is observed for the 13.56 MHz plasma in FAPES (Section 3.3.1). Time-resolved studies during a dry atomization step showed an increase in emission intensity for CO^+ in FAPES (Section 3.3.3). This increase in CO^+ intensity during the atomization step is due to increased desorption of CO from the furnace wall and from the RF electrode. In FAPES, loss of carbon from the RF electrode is observed and this loss is an additional source of carbon and CO which is absent in GFAAS. Furthermore, presence of $NaNO_3$ (effect of O_2 concentration, Section 6.3.3) and ascorbic acid (effect of CO and CO_2 concentrations, Section 6.3.5) shows pronounced effects on the emission signal for Pb in FAPES.

Carbon monoxide has been shown to affect the atomization of Pb because it is involved in a variety of homogeneous and heterogeneous equilibria including;

$$2PbO_{(g)} \rightleftharpoons 2Pb_{(g)} + O_2 \qquad (4.1),$$

$$O_2 + 2CO \rightleftharpoons 2CO_2 \qquad (4.2),$$

$$PbO_{(s)} + C_{(s)} \rightleftharpoons Pb_{(g)} + CO_{(g)} \qquad (4.3),$$

$$\text{and } PbO_{(s)} + CO_{(g)} \rightleftharpoons Pb_{(g)} + CO_2 \qquad (4.4).$$

The early release of Pb (Figure 4.9) can be due to the combined effects of equilibria (4.1) and (4.2). The presence of CO in the plasma could act as a sink for O_2 (equilibrium 4.2) such that the equilibrium (4.1) is shifted to the

right leading to an earlier appearance temperature for Pb when the plasma is present. The equilibrium (4.3) indicates that the initial generation of Pb by the reduction of PbO by carbon (in atomic absorption experiments without the plasma) should be shifted to a later appearance temperature as CO in the gas-phase increases.

Sturgeon and Willie reported a coincident appearance of PbO emission (at 286.62 nm) and Pb (at 217.0 nm), when 1 μg of Pb (as nitrate in 1 % v/v HNO_3) was deposited on the furnace wall at an RF power of 100 W [115]. The atomization temperature was 1600 K with a heating rate of about 0.2 K ms^{-1}. This simultaneous appearance of PbO and Pb is in contrast to the graphite furnace - mass spectral studies where PbO^+ signal precedes the Pb^+ signal [108,109]. However, for FAPES, the simultaneous appearance of Pb and PbO is consistent with the experimental observations provided in this thesis.

Figure 4.11 gives the effect of the RF power on the emission signal from 5 ng of Pb deposited on the furnace wall. The appearance temperature of Pb when the sample is deposited on the furnace wall at 14 W is 1010 K and at 40 W is 770 K, although an additional early peak can be seen at RF powers above 30 W. The cause of this early peak is not known at this time; however, it could arise from the reduction of PbO by CO according to the equilibrium (4.4). The temporal response of the emission signal of Pb in FAPES is complex because at least four peaks are observed at high RF powers, indicating a number of atomization or vaporization mechanisms.

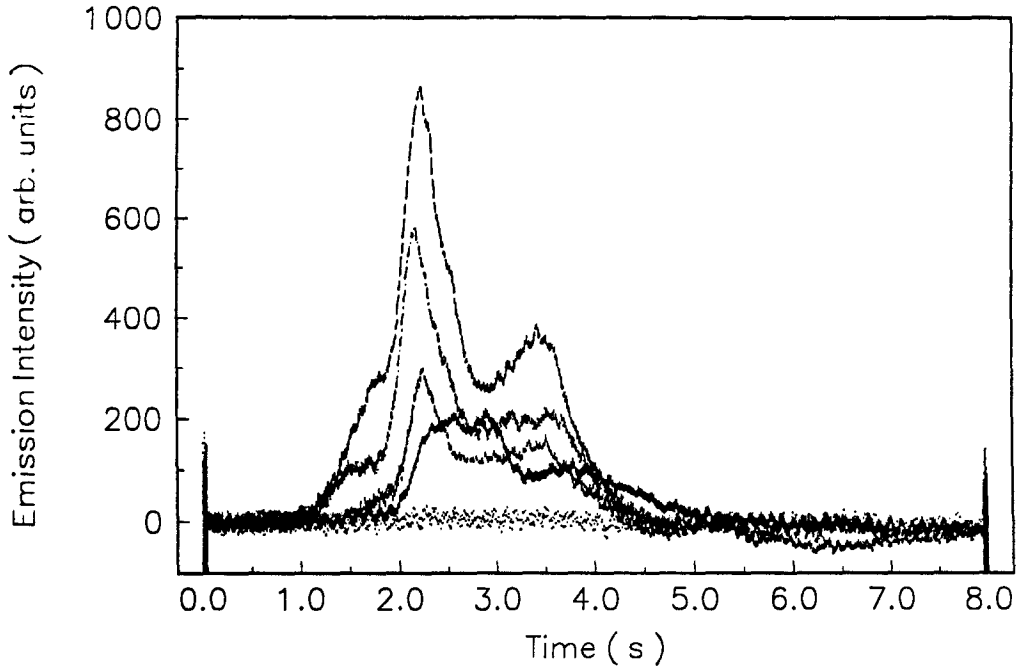

Figure 4.11. Temporal response of the Pb atomic emission signal for 5 ng of Pb deposited on the furnace wall at an RF power of 14 (——), 20 (- - -), 30 (- · - · -), and 40 W (— — —); and background at 20 W (· · ·).

Compared with Ag, there is no significant shift in peak temperature of the major peak as the RF power is increased from 20 to 40 W. This offers support for the notion that, for FAPES, the atomization of Pb is controlled by gas-phase chemistry rather than direct thermal desorption.

The effect of the excitation process on the temporal response of the emission signal is studied by simultaneously measuring atomic emission and atomic absorption signals. Figure 4.12 gives the results of this experiment at

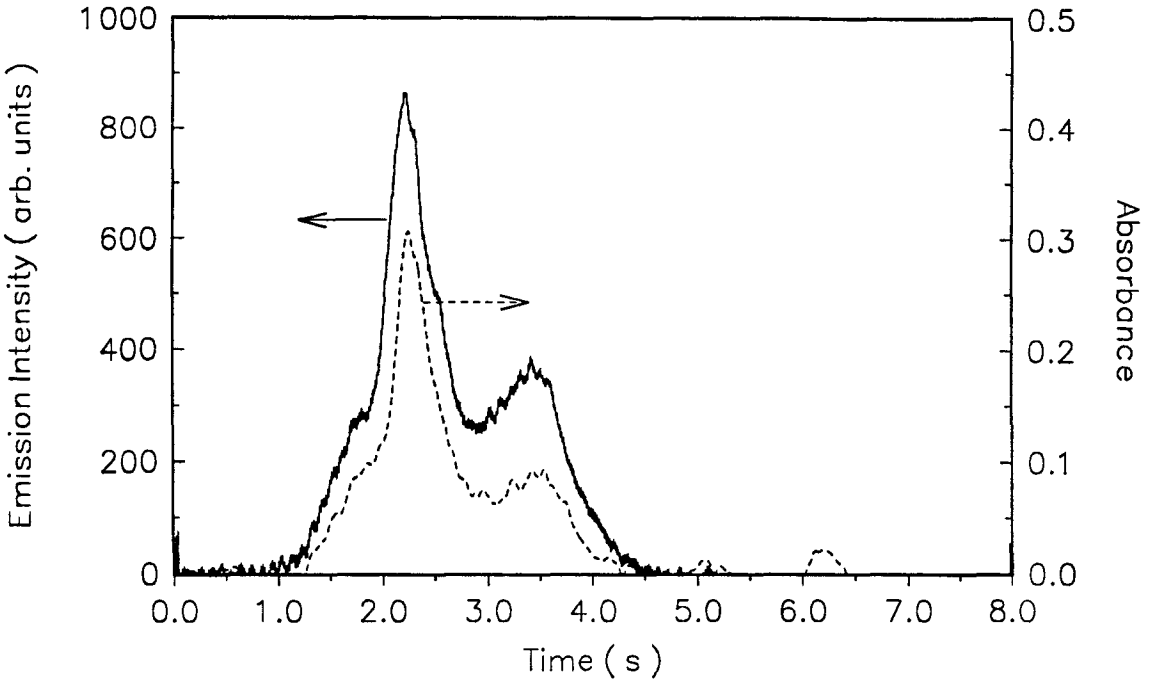

Figure 4.12. Temporal response of the Pb signal for 5 ng of Pb deposited on the furnace wall at an RF power of 40 W: emission (———) and (- - -) absorbance.

an RF power of 40 W. Similar to Ag, the temporal response of the emission signal is similar to that of the absorbance signal. This similarity in temporal response of both absorption and emission is most likely due to the dominance of atomization and vaporization characteristics of Pb in the plasma. The similar temporal responses also show no significant effect of plasma excitation process on the emission signal for Pb in FAPES.

4.3.3 Manganese

The results of an atomic absorption (AA at an RF power of 0 W) study in which 1.25 ng of Mn was deposited on the furnace wall with (dash line) and without (solid line) the co-axial rod installed are provided in Figure 4.13. The appearance temperature of the signal for the sample deposited on the furnace wall without the co-axial rod is 1470 K and the peak temperature is 1700 K. This absorption signal has a sharp rising edge compared with the falling edge, and has a peak width of 800 ms. The appearance temperature of the signal with the co-axial rod installed is 1380 K with the two peak maxima at 1560 and 1950 K. These results are similar to those for Ag and Pb; *i.e.*, with the co-axial rod, condensation and subsequent second-surface vaporization from the co-axial rod are observed.

The results of an atomic absorption (AA at an RF power of 0 W) experiment in which 1.25 ng of Mn was deposited on graphite (solid line) and tungsten (dash line) rods are given in Figure 4.14. There is a noticeable difference between appearance times and peak absorbance for Mn deposited on the two different materials. The signal from the sample deposited on the graphite rod is an overlap of two closely spaced peaks. When the sample is deposited on the tungsten rod, the apparent appearance temperature is observed at a higher value. Although these results suggest that the predominant mechanism for the formation of Mn in the graphite furnace is MnO reduction by carbon rather than MnO vaporization and thermal dissociation, some differences between the two traces should be expected as a result of the difference in heating rates and thermal conductivity of the

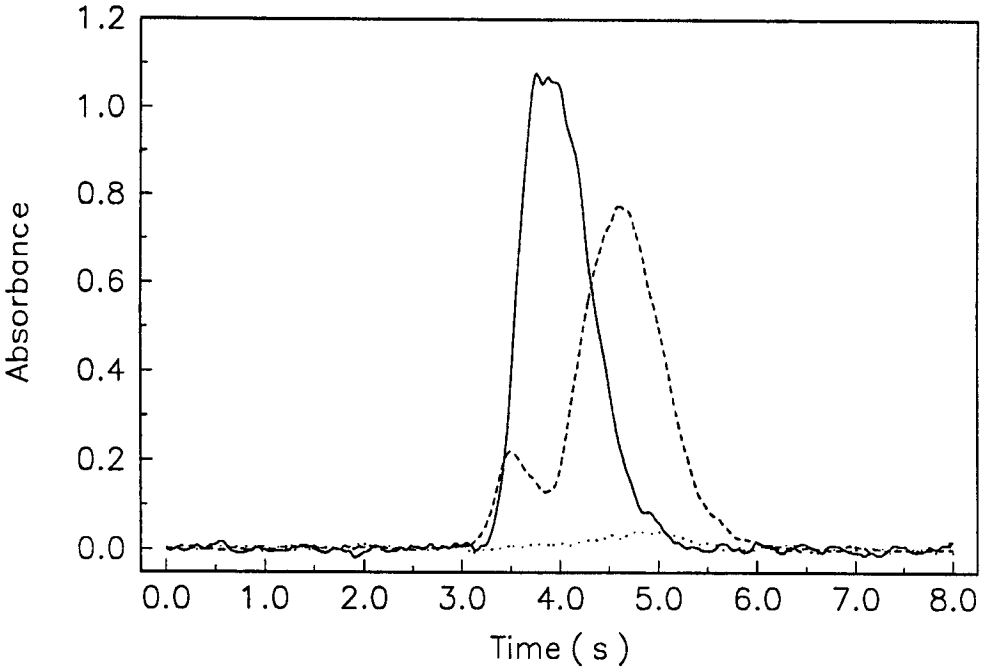

Figure 4.13. Temporal response of the Mn atomic absorption signal at an RF power of 0 W for 1.25 ng of Mn deposited on the furnace wall with (- - -), and without (——) the co-axial rod; and background (· · ·).

tungsten *vs* the graphite rods. It should also be noted that the bond energy of MnO is 4.1 eV (that of PbO is 3.8 eV) [81].

The atomization mechanisms for Mn in GFAAS have been studied in a few occasions. A study by Smets has suggested that carbon reduction of MnO as the mechanism of atom-formation in GFAAS [116]. In contrast, Aggett and Sprott studied Mn atom-formation on a tungsten strip and suggested that thermal dissociation of the oxide is the atom-formation mechanism [117].

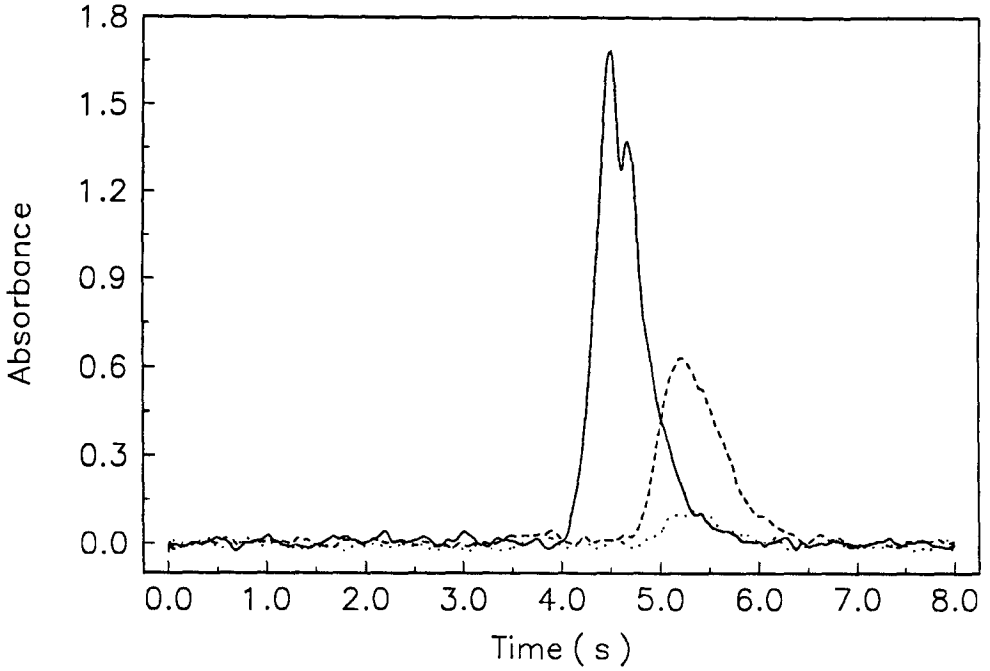

Figure 4.14. Temporal response of the Mn atomic absorption signal at an RF power of 0 W for 1.25 ng of Mn deposited on the graphite co-axial rod (——), tungsten co-axial rod (- - -); and background (···).

Frech *et al.* proposed the thermal dissociation of MnO as the mechanism of atom-formation [94]. McNally and Holcombe suggested that Mn was formed *via* desorption of molecular aggregates of MnO from the surface of the graphite furnace [118].

The most interesting observation in the data provided in Figure 4.14 is, when the sample is deposited on the tungsten rod, the absorption peak maximum appears 200 ms after the furnace wall reached its maximum

temperature. This observation may be attributed to a continued increase in the temperature of the tungsten rod even after the furnace wall reached its maximum temperature, or a time lag between initial vaporization of MnO from the tungsten rod and thermal dissociation in the gas-phase.

The results of a FAPES study in which 1.25 ng of Mn was deposited on the furnace wall (solid line) and on the RF electrode (dash line) at 20 W is given in Figure 4.15. The appearance temperature of the emission signal from the sample deposited on the furnace wall is 1340 K and on the RF electrode (apparent appearance temperature) is 1420 K. The emission signal for the sample deposited on the furnace wall is a composite of two peaks. The peak temperature of the sample deposited on the furnace wall is 1920 K and that of sample deposited on the RF electrode is 1870 K. The delayed appearance of Mn signal when the sample is deposited on the RF electrode, indicates a temperature lag in the sample deposition site of the RF electrode compared with the furnace wall. Furthermore, compared with the atomic absorption signal for the sample deposited on the furnace wall (solid line, Figure 4.13), atomic emission signals have a sharp falling edge and a narrower peak width of about 650 ms (Figure 4.15).

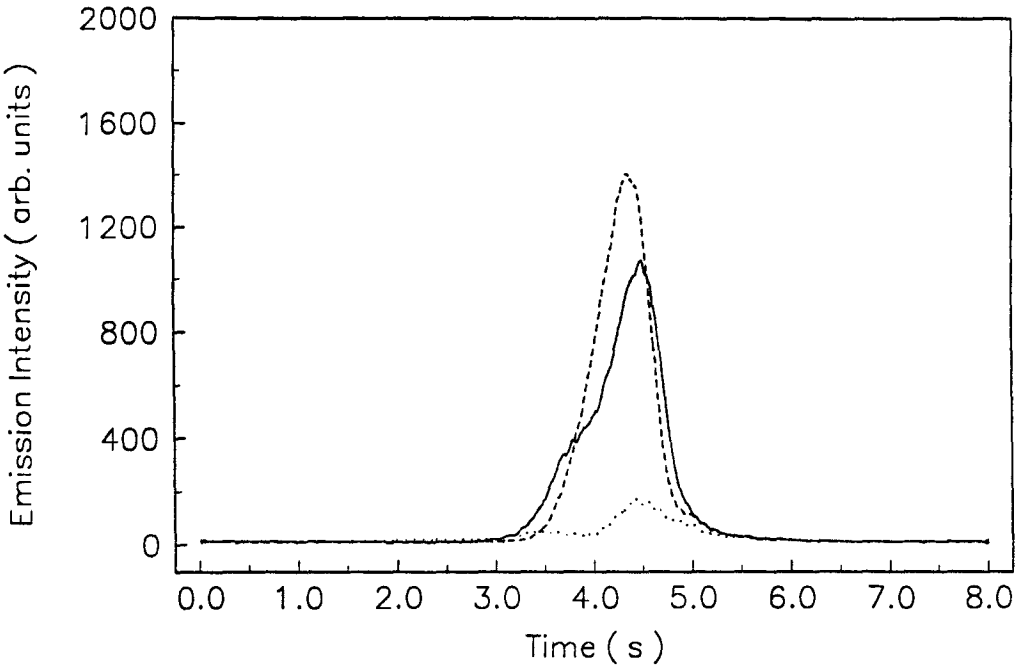

Figure 4.15. Temporal response of the Mn atomic emission signal at an RF power of 20 W for 1.25 ng of Mn deposited on the furnace wall (——) and RF electrode (- - -); and background at 20 W (• • •).

It is apparent from the comparison of the data in Figures 4.13 and 4.15 that Mn condenses on the RF electrode when deposited on the furnace wall and then vaporizes as the electrode heats radiatively. Because of this condensation, major peaks shown in Figure 4.15 (solid line and dash line) originate from the RF electrode regardless of the sample deposition site. These results suggest that after 3 s into the atomization step, the temperature of the RF electrode lags compared with that of the furnace wall.

However, this " time limit " most likely depends on the heating rate of the graphite furnace. The narrow peak width of the emission signals is likely due to Mn vaporization from the RF electrode at a instance when the gas-phase and furnace wall temperatures are high compared with that of the RF electrode. In atomic absorption experiments, when the sample is deposited on the furnace wall, analyte vaporizes into a gas-phase where the temperature lags compared with that of the furnace wall. The difference in the rising edge of the atomic absorption signal for the sample deposited on the graphite rod (solid line, Figure 4.14) compared with that for the sample deposited on the RF electrode at 20 W (dash line, Figure 4.15) is likely due to the difference in the heating characteristics of the graphite rod with and without the plasma. The falling edge of the emission signals has similar shapes (Figure 4.15) indicating similar atom dissipation processes from the graphite furnace because both peaks are from Mn vaporized from the RF electrode regardless of the sample deposition site.

The results of a FAPES study in which the RF power is increased from 14 to 40 W for 1.25 ng of Mn deposited on the furnace wall are provided in Figure 4.16. The effect of RF power on the sample deposited on the furnace wall shows that the maximum peak intensity (and peak area) of the main peak increases about five times when power changes from 14 to 40 W and a small pre-peak is observed that also increases in intensity in proportion to the larger peak. There is a small shift in the peak temperature to a lower value as the RF power is increased. The increase in intensity for both first

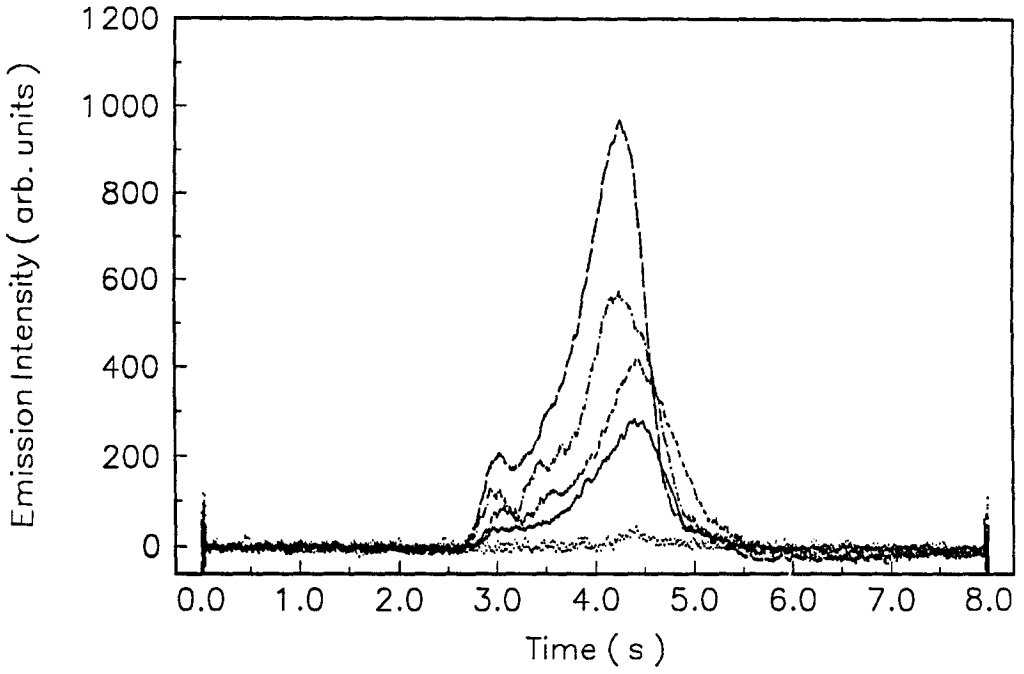

Figure 4.16. Temporal response of the Mn atomic emission signal for 1.25 ng of Mn deposited on the furnace wall at an RF power of 14 (——), 20 (- - -), 30 (- · - · -), and 40 W (— — —); and background at 20 W (. . .).

and second peaks also indicates no significant effect of RF power on the temperature of the RF electrode after 3 s into the atomization step.

Some supporting evidence for the effect of RF power on the temperature of the RF electrode can be seen from the atomic absorption measured as a function of RF power. The results of this experiment are provided in Figure 4.17. The integrated areas for both the composite peak (2.8 to 5.5 s) and the second peak (3.5 to 5.5 s) decrease with increasing RF power. If the

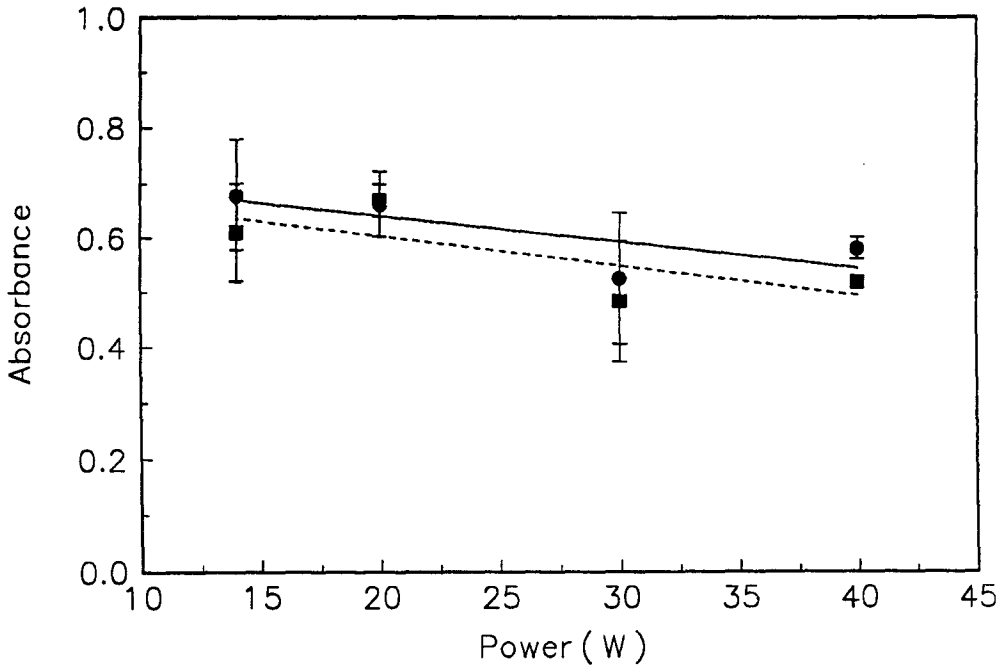

Figure 4.17. Atomic absorbance for 1.25 ng of Mn deposited on the furnace wall as a function of RF power: for 2.8 - 5.5 (●), and 3.5 - 5.5 s (■).

RF power affects the temperature of the RF electrode after 3 s into the atomization step, then the intensity of the first peak should increase and the intensity of the second peak should decrease (a similar situation to Pb).

Figure 4.18 depicts simultaneously measured atomic emission and absorption signals for Mn deposited on the furnace wall at an RF power of 40 W. As observed for Ag and Pb, the temporal response of the emission signal is similar to that of the absorption signal. This similarity in the emission and absorption signals can probably be attributed to the dominance

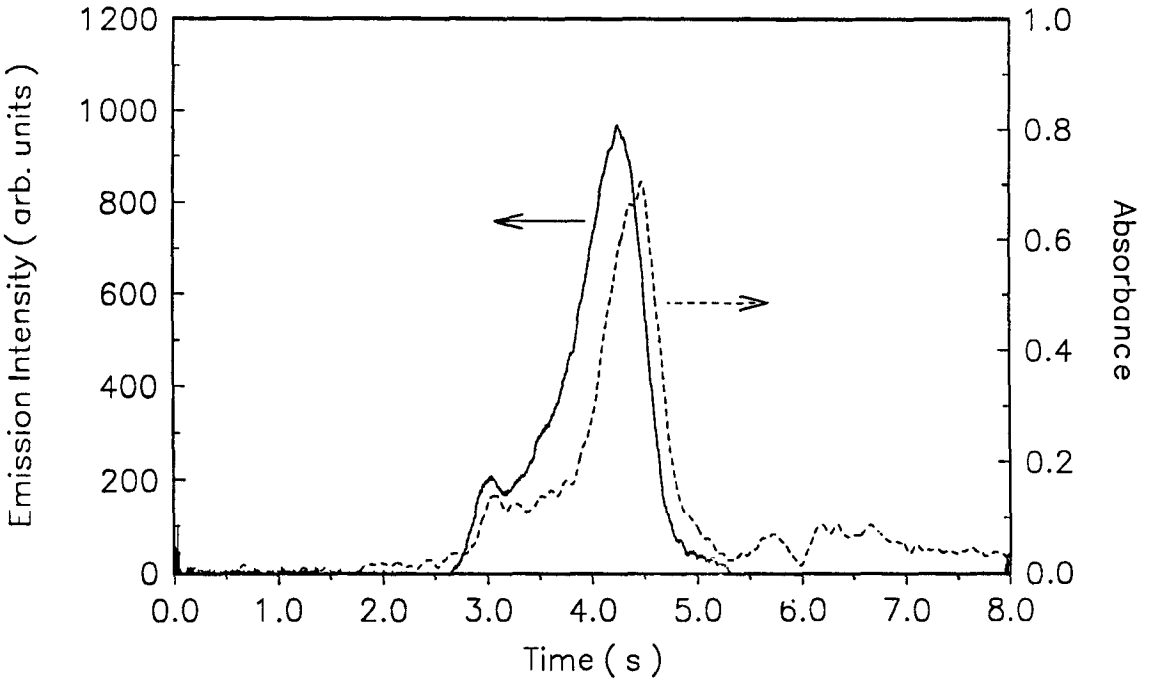

Figure 4.18. Temporal response of the Mn signal for 1.25 ng of Mn deposited on the furnace wall at an RF power of 40 W: emission (——) and absorbance (- - -).

of atomization and vaporization characteristics of Mn on the temporal response of emission signal rather than excitation characteristics. However, the peak time of the second more intense peak of the emission signal shows an early shift compared with that of simultaneously measured atomic absorption signal (both peaks originate from the RF electrode). This shift in the peak time of Mn emission signal may be due to the early appearance of Mn atoms in the more energetic excitation (temperature) volume adjacent to the RF electrode relative to the absorption volume (also see Section 5.3.1).

4.4 SUMMARY

The temporal response of the analyte emission signal in FAPES has been studied for Ag, Pb, and Mn by using both atomic absorption and atomic emission spectroscopy. The analyte sample was deposited on the furnace wall and on the RF electrode, and atomic emission and absorption profiles are compared with and without the RF plasma.

Without the plasma inside the graphite furnace, the co-axial rod is heated by radiation emitted from the furnace wall during the high temperature atomization step. Because of this radiative-heating, the temperature of the co-axial rod lags compared with that of the furnace wall. Therefore, without the plasma inside the graphite furnace, the co-axial rod acts as a condensation site for atoms and oxides that subsequently vaporize (second-surface vaporization) at higher furnace temperatures. With the plasma inside the furnace, the co-axial rod (RF electrode) is additionally heated by contact with the plasma. The temperature-time characteristics of the RF electrode with the plasma are different from those without the plasma. The RF electrode does not heat uniformly and it is likely that the RF connector acts as a heat-sink.

With the plasma inside the graphite furnace, the RF electrode heats such that for Ag and Pb, condensation is not observed except at high analyte amounts and low RF powers. For Ag and Mn, the appearance temperatures and peak temperatures are not significantly affected by the plasma relative

to the response obtained in atomic absorption experiments without the plasma. However, for Pb, the appearance and peak temperatures are shifted significantly earlier. This early appearance of Pb in the RF plasma is likely due to the presence of CO in the gas-phase, generated from oxidation of graphite on the furnace wall and RF electrode.

During the later stages into the atomization step, it appears that the temperature of most parts of the RF electrode lags compared with that of the furnace wall. It is during this time that Mn, which has a relatively high appearance temperature, vaporizes from the furnace wall. This temperature lag results in Mn condensation on the RF electrode and second-surface vaporization. The results obtained for Ag, Pb, and Mn suggest analyte condensation on the RF electrode which results in the appearance of two peaks, the more intense peak determined by the RF power. At present, the effect of the heating rate of the graphite furnace on the temporal response of the emission signal in FAPES is not known. However, it is likely that the heating rate of the graphite furnace affects the temperature-time characteristics of the RF electrode, and hence, analyte condensation and second-surface vaporization characteristics from the RF electrode.

The temporal response of the simultaneously measured atomic absorption and atomic emission signals shows similar leading and falling edges for both Ag and Pb. These results suggest that the temporal response of these elements in FAPES is determined by the atomization and vaporization characteristics of the analytes rather than by the excitation characteristics.

CHAPTER 5

EMISSION CHARACTERISTICS AND FIGURES OF MERIT FOR LEAD IN FAPES

5.1 INTRODUCTION

Analytical figures of merit such as (1) the sensitivity of the method, which corresponds to the slope of the calibration graph, (2) precision (relative standard deviation: RSD), which is the reciprocal signal-to-noise ratio (SNR), and (3) the detection limit (DL), which is the lowest amount (or concentration) of analyte which gives a signal (X_{dl}) significantly different from the background signal (X_{bl}), determine the success of an analytical method. The DL can be expressed by:

$$DL = \frac{X_{dl} - X_{bl}}{S} = \frac{k\sigma_{bl}}{S} \qquad (5.1),$$

which relates the detection limit to the standard deviation of the background (σ_{bl}) and sensitivity (S). A value of $k = 3$ is recommended for 99.86 % confidence level. Noise in the background is normally taken to be the standard deviation of the background. Therefore, both the intensity of the analyte signal and noise in the measurement (*i.e.*, in both analyte and

background signals) affect the sensitivity, precision, and the DL for an analyte in a spectrochemical determination. The DL is sometimes stated as the analyte concentration which provides a SNR of 3. This definition for the DL should be interpreted with caution because it assumes that the noise in the background and analyte signal are the same at low analyte signal levels. Furthermore, DLs are not measured directly, but rather are extrapolated from measurements made at higher concentrations, where the higher signal-to-background ratio (SBR) permits easier measurement of the analyte signal.

The intensity of the analyte emission signal depends on the concentration of analyte, particular electronic transition, the excitation temperature, and hence, on the RF power applied to the plasma. On the other hand, noise in the measurement is due to the (1) shot-noise, which is proportional to the square root of the signal intensity (2) flicker noise, which is proportional to the signal intensity, and (3) detector noise, which is independent of the signal intensity [119]. Shot-noise is due to the random arrival of photons at the detector whereas flicker noise is the low frequency fluctuations and drift. The major sources of flicker noise involve random drift of light sources, analyte atom-formation, and detection. However, the cause of flicker noise is not known [119]. Detector noise is due to the random thermal motion of charge carriers. Both shot and detector noise are distributed at all frequencies, and are referred to as " white noise ". For a shot-noise limited signal, SNR is proportional to the square root of the signal intensity, whereas for a flicker noise limited signal, SNR is independent of the signal intensity.

A more detailed review of SNR in analytical spectrometry is available elsewhere [120].

The dominant noise in an atomic absorption signal, in the analytical range (absorbance between 0.2 and 1) in GFAAS, comes from the analyte absorption fluctuations (flicker or drift) [120]. However, for graphite furnace - plasma methods, such as FAPES and FANES, additional sources of noise may be present in the signal. These additional sources of noise in the signal are the plasma background flicker and shot-noise that arise during the atomization step and the analyte emission flicker and shot-noise that arise during the excitation. At the analytical wavelength, there may be a structured background by emission from molecular species. In the atmospheric pressure plasma source in FAPES, about 80 % of the analytically useful wavelength region (200 - 500 nm) is dominated by emission from molecular species such as CO^+, N_2, and OH. Variations of the excitation temperature during the analyte excitation and condensation of the analyte on the RF electrode may also contribute to a poor precision in the measurement.

For FAPES, effects of the RF power on the emission characteristics of the analyte or on the background have not been studied. Smith *et al.* employed a plasma at an RF power of 20 - 30 W [17], whereas Sturgeon *et al.* employed one at 50 W [78], during the determination of figures of merit for FAPES. Sturgeon *et al.* reported a highly structured background in the vicinity of the analytical lines: NO band near lines for Cd, Fe, and Be; CO bands near Ni;

and OH bands near Bi and Pb [78]. Sturgeon *et al.* also reported an optimum SBR for Cd (228.2 nm) at 50 W and for Pb (217.0 nm) at 75 W [121], but a detailed study has not been reported. For HC-FANES, Falk *et al.* reported that the limiting noise, and consequently, the DLs, were determined not by the recombination continua but by extraneous background molecular emission bands [13]. For HA-FANES, Riby *et al.* reported emission from CN and NH in the plasma background, and employed wavelength modulation to correct the background at 357.9 nm for the determination of Cr [90]. Hollow cathode-FANES and HA-FANES are normally operated at forward powers between 20 and 60 W.

In an effort to understand the emission characteristics of analytes in FAPES, the effect of RF power on the analyte emission intensity and noise in the measurement was investigated. Lead was examined as the test analyte in this study. Lead is one of the few elements which requires detection of ultra trace levels for the analysis of biological and environmental samples, and appears to be the most widely determined element by GFAAS. The time-resolved Pb-excitation temperature was also measured as a function of RF power, to study the effect of analyte excitation process on the temporal response of the Pb emission signal.

5.2 Experimental

A complete description of the experimental system employed to acquire atomic emission signals is given in Chapter 2 of this thesis. This

experimental system and a vertical-mount for the RF electrode were employed. The following experimental methods and parameters should be noted.

5.2.1 Signal Presentation

Four replicate measurements were averaged and subjected to a 25-point Savitzky-Golay smoothing procedure [91]. Analytical parameters, such as peak height, peak area, and peak width, were evaluated for each sample deposition.

5.2.2 Reagents

All Pb solutions in 1 % (v/v) HNO_3 were prepared from serial dilution of a 1000 mg L^{-1} stock solution prior to analysis. Lead and HNO_3 solutions were prepared by dissolving analytical grade $Pb(NO_3)_2$ and HNO_3 (both, BDH Toronto, Canada).

5.2.3 Procedure

A 5 μL aliquot of solution was deposited onto the furnace side wall with an Eppendorf 0.5 - 10 μL UltraMicro pipette. The plasma source work-head was purged with helium (Union Carbide, Toronto, Canada). The furnace temperature was increased to 400 K for 60 s to dry, and was maintained at 650 K for another 20 s to ash the sample. This total time interval is

sufficient to exclude the water vapor inside the plasma source work-head before the plasma ignition. Within the next 10 s lag time, the plasma was ignited. After this lag time, the furnace temperature was ramped to 2000 K in 5 s for all determinations. The blank determinations were carried out by depositing the same volume of 1 % (v/v) HNO_3 solution. After each sample atomization step, a dry atomization step (without deposition) was carried out to clean the graphite furnace.

Four replicate measurements were carried out for each determination and integrated for 3 s: from 0.5 to 3.5 s into the atomization step (unless otherwise noted).

All determinations were carried out by using an atomic resonance line of Pb (283.30 nm) and a spectral bandwidth of 0.06 nm (unless otherwise noted).

5.3 Results and Discussion

5.3.1 Time-resolved Pb-excitation temperature

The time-resolved Pb-excitation temperature was evaluated by using the two line method (Section 1.4.5). The two lines of Pb (I) used in the excitation temperature measurement were 280.1 and 283.3 nm. Spectral characteristics of these two Pb lines are given in Table 5.1. Transition

Table 5.1. Wavelengths, Excitation energies, and Spectral characteristics for the two Pb lines used for the Pb-excitation temperature determination [122].

Wavelength (nm)	E_p (eV)	g_pA_p (s^{-1})
280.19	5.7439	4.3×10^9
283.30	4.3749	1.8×10^8

probabilities were obtained from Corliss and Bozman [122]. At each wavelength, four replicates of 0.5 ng of Pb in 1 % HNO_3 (four replicates of 1 % HNO_3 for blank) were measured and the averaged temporal emission profile was calculated. From this averaged temporal emission profile, the time-resolved Pb-excitation temperature was evaluated as a function of RF power.

Figure 5.1 depicts the time-resolved Pb-excitation temperature (solid line) during the atomization of Pb at an RF power of 50 W. The variation of the wall temperature of the graphite furnace (dash line) is also given. The peak-to-peak averaged Pb-excitation temperature for a 50 W plasma (Figure 5.1) is 4560 ± 100 K (from 1 - 3.5 s). At 20 and 100 W, the Pb-excitation temperatures are 3990 ± 80 K (from 1 - 2 s), and 4840 ± 110 K (from 1 - 2.5 s), respectively. The calculated Pb-excitation temperature was

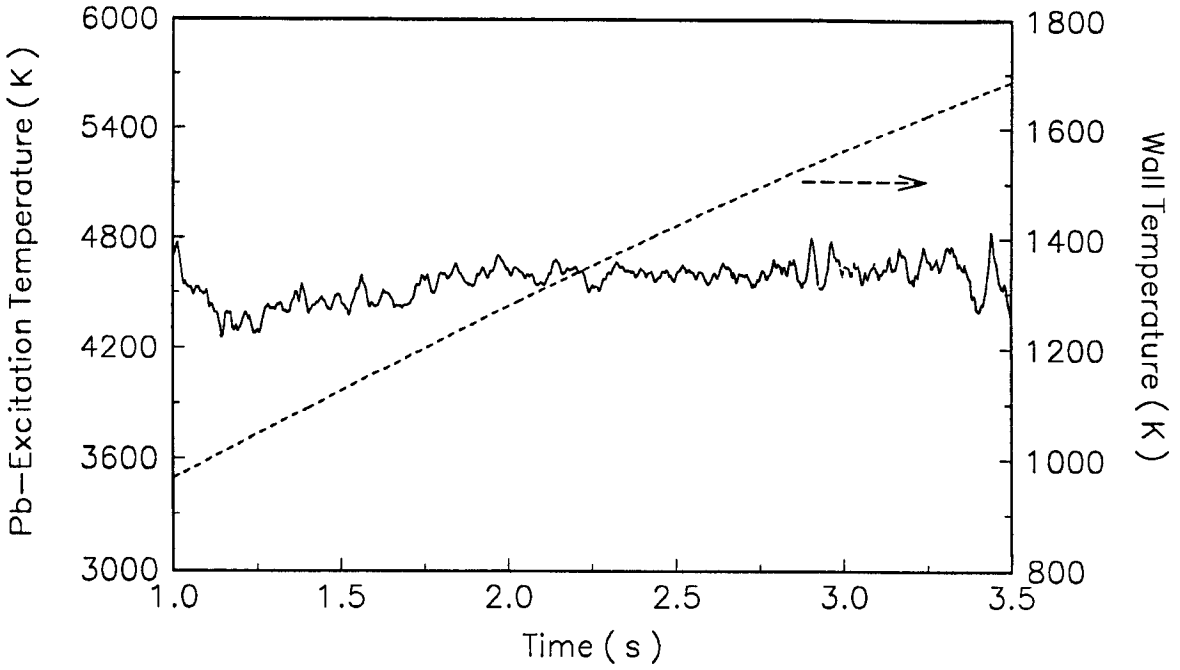

Figure 5.1. Time-resolved Pb-excitation temperature (——) at an RF power of 50 W and the corresponding graphite furnace temperature (- - -) during the atomization step of Pb.

limited to a specific time duration due to the transient nature of Pb emission intensity and the background correction error.

The time-resolved Pb-excitation temperature provided in Figure 5.1 shows some random rather than systematic fluctuations within the precision of the measurement. This time-resolved temperature measurement also shows that the Pb-excitation temperatures are not affected by the thermionic electrons when the furnace temperature is below 1800 K at 50 W, because the

thermionic electron concentration is too low to be significant for the furnace temperature range in which Pb is present in the plasma. However, at an RF power of 100 W, the reflected power starts to increase just after the emission signal of Pb reaches that of the background; after 3.5 s into the atomization step. This increase in the reflected power is probably due to a significant increase in the evolution of thermionic electrons from the RF electrode at higher RF powers.

Sturgeon *et al.* also reported that the He-excitation temperature was not influenced by the furnace wall temperatures up to about 2700 K [80]. The measured He-excitation temperature was about 3450 K at 50 W and 3650 K at 100 W. For the measurement of He-excitation temperatures, the higher furnace temperature range, 1670 - 2650 K, was accessed by recording the transient response of helium (I) lines with a preset upper temperature, and the lower furnace temperature range, 300 - 1330 K, was accessed under steady state conditions. For FAPES, Sturgeon *et al.* used an atomization temperature of 2700 K [16,78,79,123]. They also reported an increase in the reflected power with increasing furnace temperatures above 1800 K [16,79,123].

To date, for FANES sources, neither the time-resolved nor the peak excitation temperatures for analytes have been reported. For HC-FANES, Falk *et al.* also reported no significant change in the helium or Ar excitation temperatures although the electron density decreases significantly when the furnace temperature exceeds 1700 K limit [124]. However, Falk *et al.*

reported a significant decrease in the cathode voltage (about 85 % of the initial voltage of 300 V) at a constant current when the cathode (graphite furnace) temperature was increased above 1700 K [124]. This change in the electrical characteristics has been attributed to the thermionic electrons from the graphite furnace wall. For HA-FANES, the maximum atomization temperature reported is 2200 K. At furnace temperatures above 1800 K, changes in the current-voltage characteristics due to the evolution of thermionic electrons have been reported [125].

With reference to the previously observed shifts in the absorption and emission maxima (Section 4.3), a brief discussion is warranted. For an atomic absorption measurement, absorbance is proportional to the number of free atoms: N, in the gas-phase at a given instance [43,126], hence, the maximum absorption (A_{max}) at N_{max} (maximum number of free atoms in the gas-phase). In the case of simultaneous atomic absorption and atomic emission measurements, the maximum emission (I_{max}) appears early compared with A_{max}. This early shift indicates that I_{max} occurs at a time when the number of free atoms in the gas-phase is increasing. However, if the excitation temperature (T_{exe}) is decreasing at this time, then the emission intensity can decrease because the emission intensity is proportional to N_p: the number of excited atoms in the gas-phase, and hence, the Boltzmann factor: $e^{-E/kT_{exe}}$ (Section 1.4.5).

The early shift observed for the Mn emission maximum is 200 ms relative to the absorption maximum (Figure 4.18). This observation is in contrast to

the pronounced late shifts in I_{max} from A_{max} reported for CFAES [10,127], where thermal excitation of the analyte is solely dependent on the graphite furnace temperature. Although the observed shift for Mn may be explained by a decrease in Mn-excitation temperature while the furnace temperature is increasing, both emission and absorption profiles show similar falling edges. Therefore, possible changes in Mn-excitation temperature do not explain the early shift of peak emission relative to peak absorption. It should be noted here that Mn atomizes at a medium graphite furnace temperature.

However, at higher furnace temperatures, the effect of thermionic electrons may be significant. The excitation characteristics may change due to the thermionic electrons emitted from the RF electrode (and from the furnace wall). However, it is difficult to evaluate the effect of thermionic electrons at higher furnace temperatures on the excitation temperature, because the thermionic electrons can also affect the plasma impedance, and hence, the net energy coupled to the plasma.

5.3.2 Effect of RF power

Figure 5.2 depicts the net emission intensity of 0.5 ng of Pb as a function of RF power. Also plotted in Figure 5.2 is the Boltzmann factor: $e^{-E/kTexe}$ (dash line), for Pb as a function of RF power. The Pb-excitation temperatures at 20, 50, and 100 W were used to calculate the Boltzmann factor. Although Boltzmann distribution predicts an exponential increase in emission

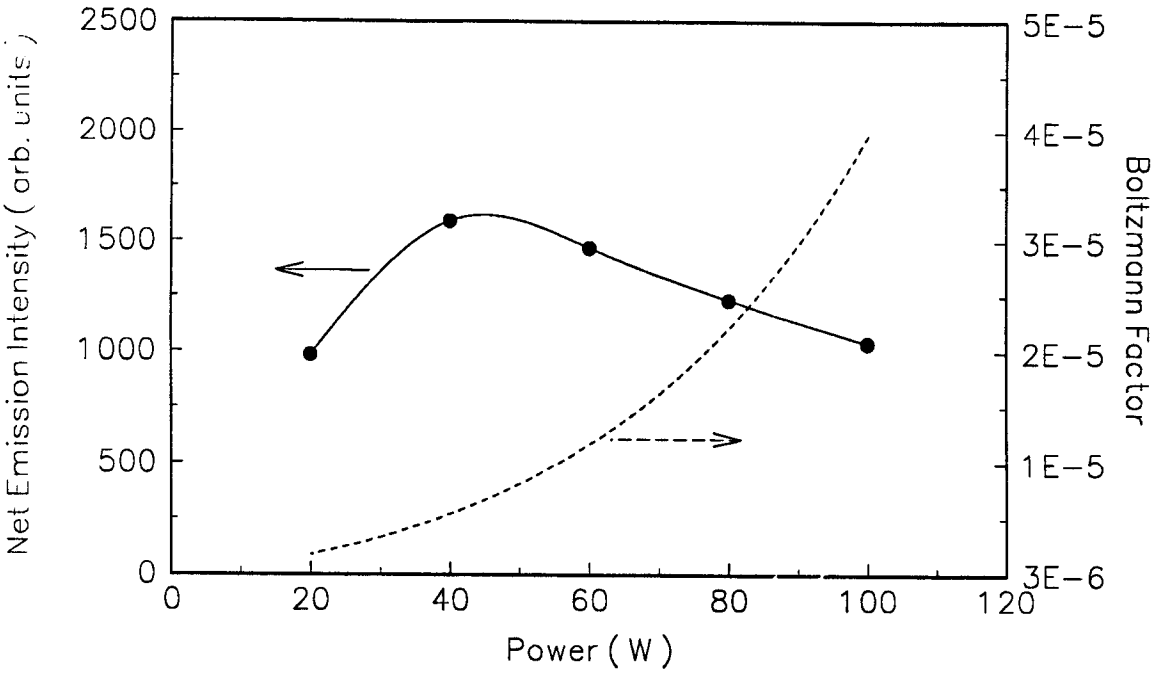

Figure 5.2. Effect of the RF power on the net emission intensity of Pb (●) and on the Boltzmann factor (- - -).

intensity with increasing RF power, the emission intensity for Pb increases up to about 50 W and then decreases. This decrease in emission intensity for Pb may be due to losses during the pre-atomization or atomization steps, changes in the excitation characteristics, or an increase in ionization of Pb with increasing RF power.

The pre-atomization and atomization losses in the graphite furnace methods are due to the high volatility of the analyte molecular species, and a slow heating rate of the graphite furnace coupled with a lower atomization

temperature. For GFAAS, it has been shown that Pb can be ashed up to about 800 K without loss of analyte [128,129]. However, during the slow atomization step employed in the experiments described in this chapter, some Pb may be lost as undissociated PbO before the gas-phase temperature is high enough. The atomization losses may also be significant due to the increased diffusion with increasing temperature at high RF powers. RF sputtering may also cause a loss of analyte from the furnace wall prior to atomization. However, Sturgeon *et al.* reported no measurable decrease in the Ag emission signal even during an extended 2 min period of plasma operation prior to the atomization step [79].

The Pb-excitation temperature shows an increase with increasing RF power (Section 5.3.1), and therefore, the decrease in the Pb emission signal intensity at high RF powers cannot be due to a change in the excitation temperature. However, it is possible that the excitation characteristics are affected by the presence of thermionic electrons at high RF powers. The possible changes in the excitation characteristics are decreased collisional excitation rate (as a consequence of changes in the electron number density for excitation in the plasma) and increased collisional de-excitation rate (due to the low energy thermionic electrons). Although no changes in the reflected power are observed before 3.5 s into the atomization step, some temporal characteristics of ionic species such as CO^+ and N_2^+ are attributed to the evolution of thermionic electrons (Section 3.3.3). Furthermore, the He-excitation temperature measurement for FAPES by Sturgeon *et al.* [80], and Ar and He-excitation temperature

measurement for HC-FANES by Falk *et al.* [124], show that the thermionic electrons do not affect the excitation temperature at higher furnace temperatures; however, they can influence the electron density of the plasma [124]. Sturgeon *et al.* have not reported the variation of electron density with furnace wall temperature for FAPES, because of the increase in reflected powers above 1800 K [80].

For plasma spectrometric methods, analyte ionization may also be significant. When the RF power coupled to the plasma is increased, it not only increases the analyte excitation, and hence, increases the emission but also increases the analyte ionization. Compared with high temperature plasma sources like ICPs (with the excitation temperature ranging from 4000 - 7000 K), the low pressure d. c. plasma sources in FANES (with the excitation temperature ranging from 1000 - 3000 K) are considered to be low ionization plasma sources [13]. However, for the RF plasma source in FAPES, the excitation temperature ranges from 3000 - 5000 K, depending on the RF power and the thermometric species used for the measurement (Sections 3.3.4 and 5.3.1). Evidence for ionization of Ag in FAPES is discussed in Section 6.3.4. Silver with an ionization potential (IP) of 7.5 eV (that of Pb is 7.4 eV), shows an ionization suppression when a high amount of Na (IP is 5.1 eV) is present during the atomization. Analyte ionization may be significant at high RF powers, and hence, a source for the suppression of atomic emission signal intensity in FAPES.

The Pb-excitation temperature for the helium RF plasma source in FAPES is similar to that reported for Ar-ICP operating at an RF power of 1.5 kW [130]. Similar excitation temperatures for FAPES and ICP can be attributed to the fact that radiative and convective heat losses from the FAPES source are much lower than those from an ICP, or to the fact that the electric field strength is much higher in the FAPES source (Section 3.3.4). For the ICP, Blades and Horlick reported norm temperatures (temperature at which the maximum in emission intensity occurs) between 4000 and 5000 K for the emission lines with excitation potentials between 4 and 5 eV, respectively [131]. At temperatures higher than the norm temperature, emission intensity decreases as the ionization become significant. Nevertheless, the exact cause of the decrease in the Pb emission signal at high RF powers (Figure 5.2) is not known at present, and needs further study.

Sturgeon *et al.* have compared the relative intensities for a number of ionic lines at an RF power of 50 W with those of ICP, and suggested that the degree of analyte ionization was significantly lower in the FAPES source [78]. The ionization temperature reported by Sturgeon *et al.* for FAPES ranged from 4800 - 5900 K at an RF power of 100 W, depending on the thermometric species [80], compared with the ionization temperature for ICP which ranged from 6700 - 8000 K for RF powers between 1 and 1.5 kW [68]. However, Sturgeon *et al.* acknowledged that about 85 % of the applied RF power was dissipated in the tuning network for their experimental system, with the

result that the plasma was apparently operating on only a few watts of real power [79].

For HC-FANES, Falk *et al.* reported an increase in the emission intensity for Ni, Cr, Cu, Fe, Co, and Al when the discharge current is increased from 20 to 60 mA [124]. However, the power coupled to the HC-FANES source is only 18 W at a discharge current of 60 mA. For HA-FANES, Harnly *et al.* reported a constant emission intensity for Cu and Cd above a threshold current (50 and 20 mA for Cu and Cd, respectively) when the discharge current was changed from 10 to 80 mA, but the reason for these emission characteristics was not known [125].

5.3.3 Signal-to-Noise ratio

Figure 5.3 depicts the temporal response of the Pb emission signal for 0.5 ng of Pb (solid line) and that of the background (dot line) at an RF power of 20 W. For the study of SNR and SBR, the standard deviation of four replicates of analyte emission signal is assumed to be equal to the noise in the " net " signal. The propagation of error method shows that, for the addition of two independent quantities, the total variance is the sum of the two variances. However, the analyte flicker noise and the blank flicker noise are not an exact addition because analyte flicker noise occurs during the sample and not during the blank [119]. But, at high SBRs, that the total noise in the measurement is equal to the noise in the signal, is a good approximation. It should be noted that these SNRs are overestimates of the

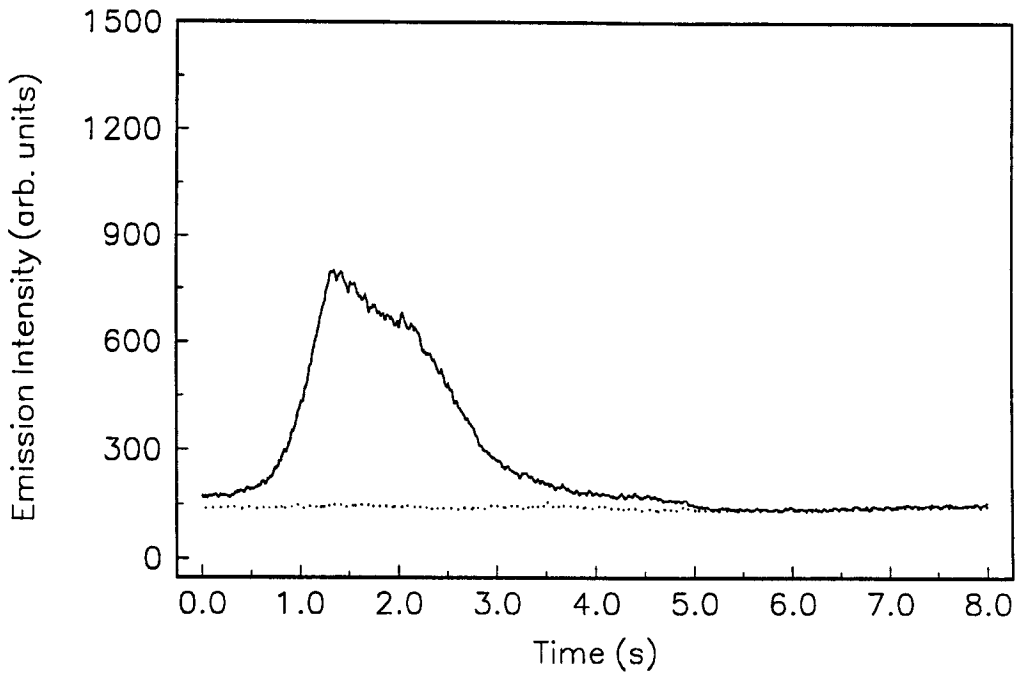

Figure 5.3. Temporal response of the Pb emission signal at an RF power of 20 W for 0.5 ng of Pb (——); and background (- - -).

true SNRs, and the overestimation depends on the number of measurements because the standard deviation is a negatively biased estimate of the variance [132].

It was noted that the best SNR was obtained by peak area measurement compared with peak height measurement because the magnitude of the peak area was high compared with that of the peak height. Furthermore, the standard deviation of the peak height measurement was low compared with

that of peak area measurement. These observations are most likely due to the slow heating rate of the graphite furnace.

For GFAAS, the effect of heating rate on the peak height or the peak area has been reported on a number of occasions. Torsi and Tessari reported an increase in peak height with increasing heating rate [133]. Gregoire *et al.* reported an increase in peak height and an exponential decrease in peak area for relatively volatile elements, but an exponential increase in peak area for relatively non-volatile elements when the heating rate was increased [134]. Zhou *et al.* reported, for Ag and Pb, a decrease in peak area and an increase in peak height when the heating rate was increased under isothermal conditions [135]. However, a constant peak area and an increased peak height were observed when the heating rate was increased under non-isothermal conditions [135]. Falk suggested an increase in peak height and a decease in peak area when the heating rate was increased [136]. In summary, it appears that the effect of increasing heating rate is to increase the peak height at the expense of the peak area. The effect of heating rate on peak height or peak area may also depend on the nature of the analyte.

Although it has been widely believed that improved precision and linearity of the calibration graph can be obtained by peak integration, experimental or theoretical studies on the merits of peak height *vs* peak area measurements have been limited. The main reason for this limited number of studies have been the complexities in dealing with the low frequency flicker noise in transient signals. Schramel evaluated the peak height and the peak area

measurements for GFAAS, and suggested that the peak area gives better precision and increased linearity in the calibration graph [137]. Sturgeon *et al.* reported similar DLs and precision, but lower sensitivity and wider linear range for the measurement of peak area compared with that of peak height for the CRA furnace [138]. However, for the HGA furnace, Sturgeon *et al.* reported increased sensitivity for the peak areas compared with peak height measurement [139]. The difference between analytical characteristics of CRA and HGA furnaces was attributed to the increased diffusion losses from the CRA furnace [139]. For Cu and Pb in GFAAS, Harnly reported that the precision for peak areas integrated from the appearance time to t_{1/e^2} was 30 % better than the precision for areas integrated over the whole peak and were 10 % better than those for peak heights [140]. However, for V, the precision for peak height measurements was better than that for peak area measurements, regardless of the integration interval [140].

Furthermore, it has been recognized that integration of the entire peak does not necessarily yield the maximum SNR. Piepmeier predicted improvements in precision by up to a factor of six when transient absorbance peaks with long tails were only partially integrated; however, there was no loss of precision when the Gaussian absorbance peaks were integrated over 99 % of the total peak [141]. Laeven and Smit estimated the optimum peak area for a shot-noise limited Gaussian peak when the peak was integrated from the peak maximum minus $1.4\sigma_p$ to the peak maximum plus $1.4\sigma_p$ (where σ_p is the variance) [142]. However, the estimation of the

optimum peak area for a flicker noise limited peak was complicated [142]. Voigtman also estimated the optimum peak areas for shot-noise limited signals with different peak shapes [143]. In a recent publication, Kale and Voigtman predicted not well defined boundaries for the integration of the flicker noise limited peaks [144].

In summary, it appears that the determination of the optimum integration time interval for the maximum SNR for a flicker noise limited transient signal is difficult, especially for the transient signals in graphite furnaces where atomization and residence times play an important role in determining the duration of the peak, and hence, noise in the signal. The intent here is to study how noise in the analyte emission signal and that in the background vary with the RF power rather than to determine optimum values for the SNR. All emission signals (both the analyte and background) were integrated for 3 s, starting from 0.5 s into the atomization step, which covers about 95 % of Pb signal at 20 W.

Figure 5.4 is a plot of SNR as a function of Pb emission intensity at an RF power of 20 W. These data illustrate that SNR is constant at higher signal intensities. In addition, both SBR and signal-to-background noise ratio increase linearly with the signal intensity. Thus, at higher SBRs, limiting noise in the Pb signal is due to the analyte flicker noise which has a characteristic linear dependence with signal intensity. Furthermore, the maximum SNR obtained for the Pb signal is about 12, which corresponds to an RSD of about 8 %.

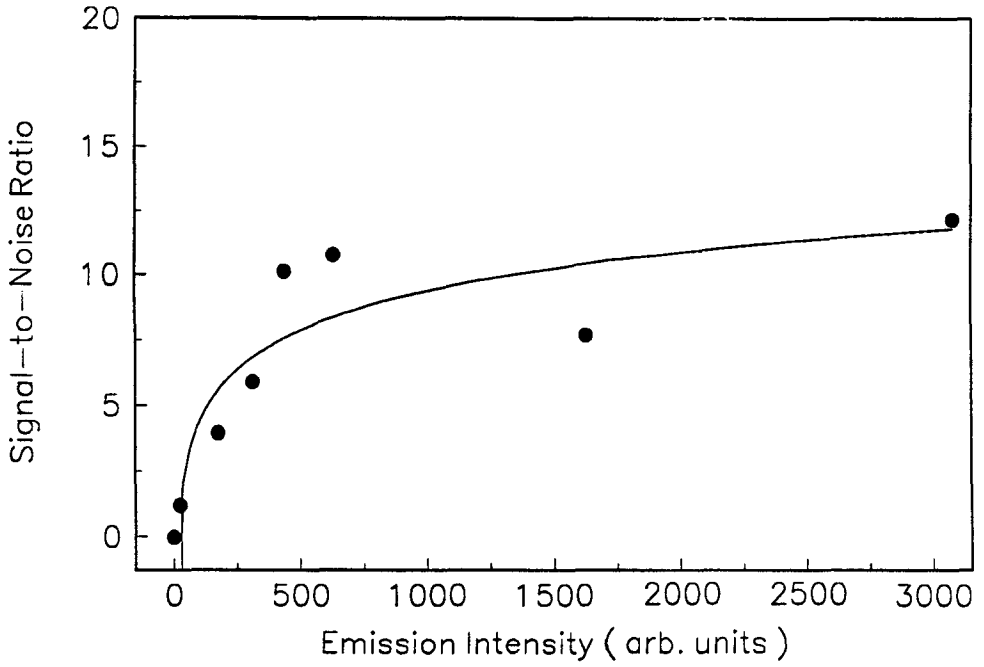

Figure 5.4. Lead signal-to-noise ratio (SNR) as a function of signal intensity.

Figure 5.5 depicts plots of SNR and SBR as a function of RF power. The effect of RF power on the net Pb emission intensity is previously provided in Figure 5.2. The SNR decreases up to about 50 W and then shows a marginal increase as the RF power increases. However, the SBR steadily decreases as the RF power increases. The data presented in Figure 5.5 also show that the highest SNR and SBR are at 20 W. The marginal increase in the SNR at high RF powers is likely due to the changes in the background noise characteristics.

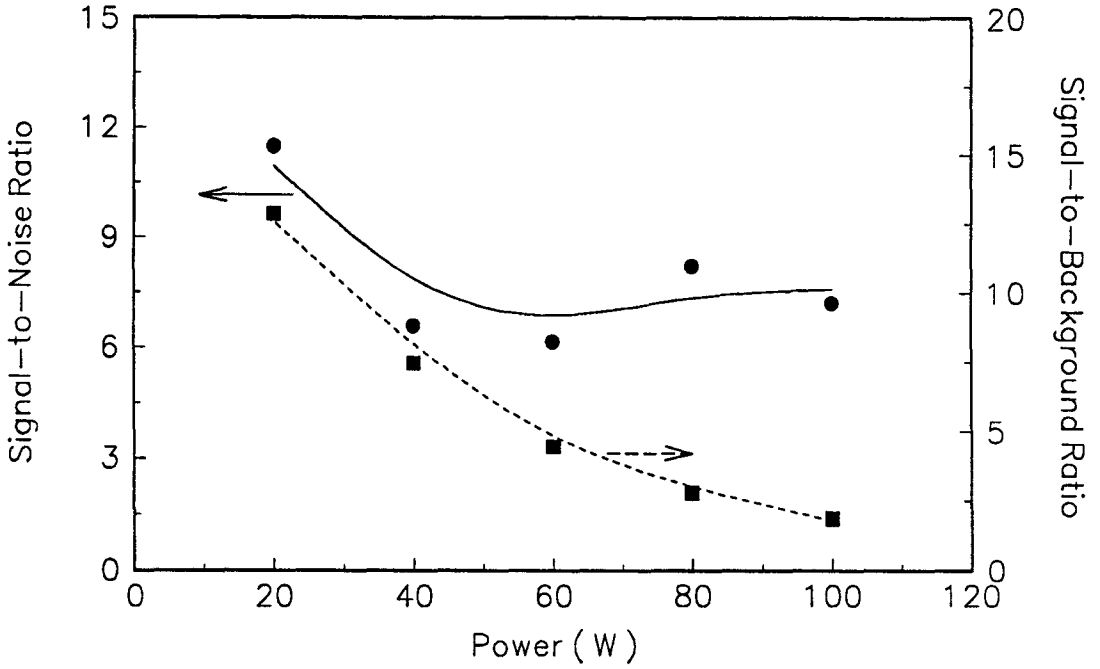

Figure 5.5. Effect of RF power on the signal-to-noise ratio (SNR: ●) and the signal-to-background ratio (SBR: ■) for Pb.

Figure 5.6 depicts the net background emission at 283.3 nm and the relative standard deviation of the background (RSDB) as a function of RF power applied. These data illustrate that the background emission steadily increases up to about 50 W and then shows a marginal increase. In contrast, the RSDB decreases with increasing RF power. This decrease in the noise in the background signal at high RF powers can account for the marginal increase in SNR at low SBRs (Figure 5.5).

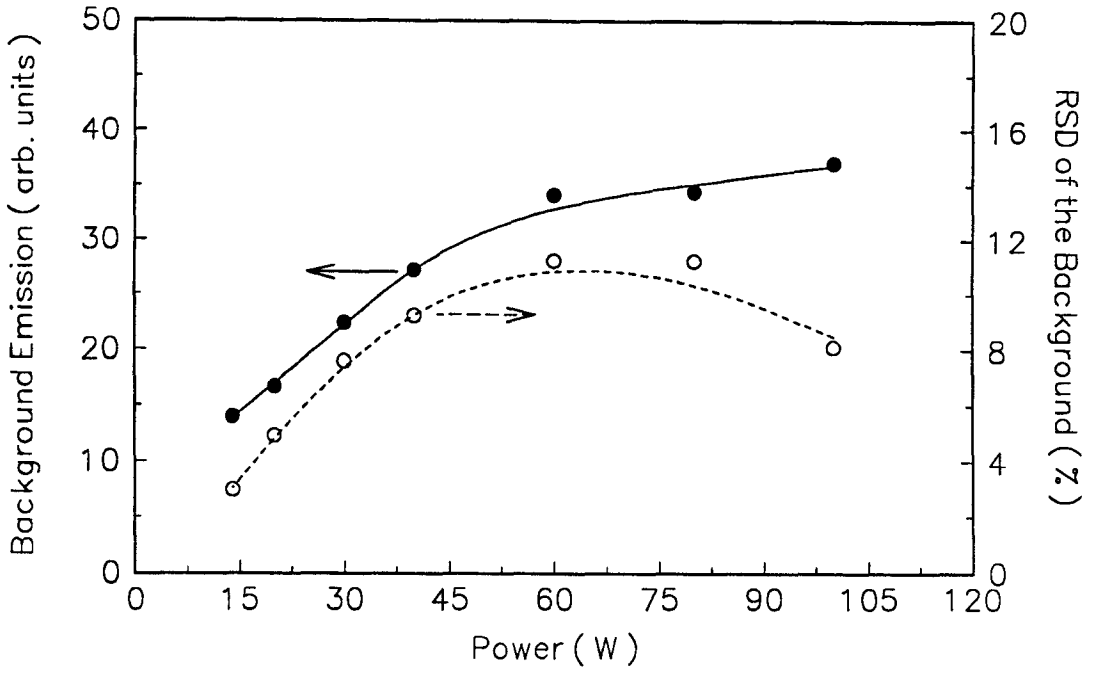

Figure 5.6. Effect of RF power on the net background emission (●) and the relative standard deviation of the background (RSDB: ○).

The plasma background emission is an important diagnostic tool in atomic spectroscopy. If the plasma background emission results from continuum emission as a consequence of radiative recombination (Section 1.4.3), the plasma background can be related to the electron number density and the electron temperature in the plasma [145,146]. The nature of the background emission signal at the analytical wavelength of Pb (283.30 nm) was studied by varying the spectral bandwidth of the monochromator. Figure 5.7 depicts the effect of spectral bandwidth on the square root of the net background

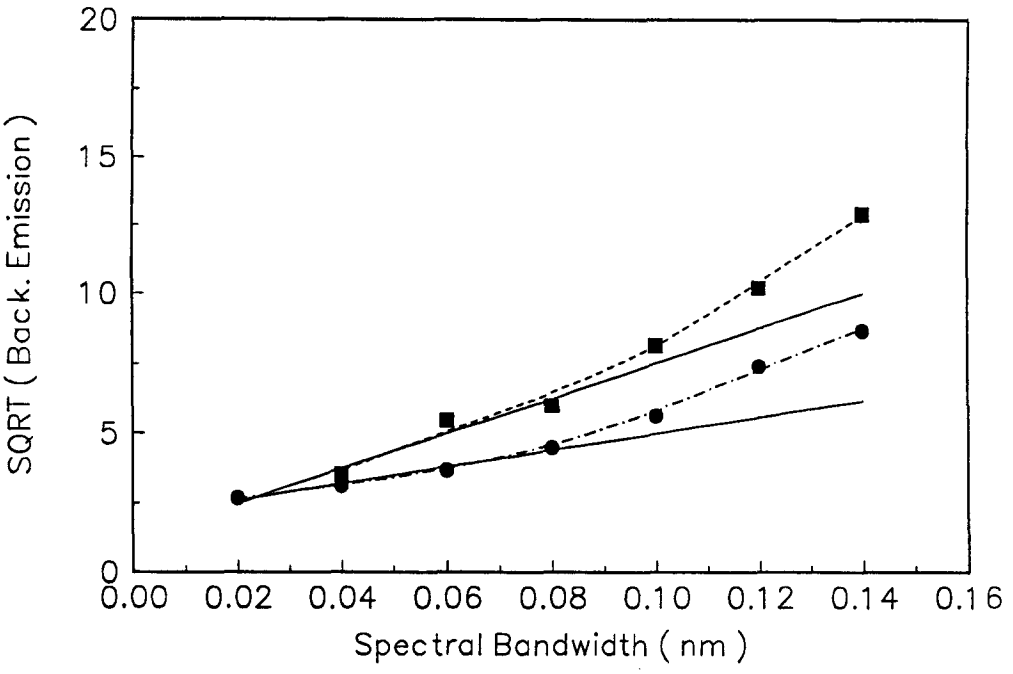

Figure 5.7. Effect of the spectral bandwidth on the square root of the background emission intensity at 283.3 nm; 20 W (●), 40 W (■).

emission intensity. The amount of background emission collected increases linearly with the spectral bandwidth up to about 0.08 nm and then increases exponentially with increasing spectral bandwidth. In addition, an increase in RF power increases the background emission intensity.

If the continuum emission is imaged on an entrance slit, the measured intensity is proportional to the square of the spectral bandwidth. The exponential increase of the background emission with the increase of spectral bandwidth above 0.08 nm (Figure 5.7) indicates a partial spectral overlap.

It was also observed that, an increase in the spectral bandwidth increases the Pb emission intensity linearly; however, increasing the spectral bandwidth above 0.08 nm causes a decrease in SNR, probably due to the higher level of noise in the background. The temporal response of the background at a wider spectral bandwidth is similar to that of the OH at 306 nm (Section 3.3.3). The background emission feature around 283 nm wavelength is the (1,0) OH vibrational band at 281 nm (Section 3.3.1).

At narrow spectral bandwidths and low RF powers, the dominant source of background noise may come from the scattered blackbody radiation from the graphite furnace, which generates both shot-noise and a drift noise due to the varying temperature of the graphite furnace during the atomization step. At wide slit widths, the flicker noise in the background at 283.30 nm is likely due to the significant drift in the characteristic temporal emission of OH during the atomization step and the variation of the amount of OH present in the plasma. The variation of the amount of OH present in the plasma is due to the desorption of OH from the furnace wall and the dissociation of H_2O in the gas-phase. The background transients collected without the ash step or the high temperature atomization step show a large variation in the background emission intensity between replicates with increasing RF power. This observed variation of background emission between replicates may be attributed to a change in the amount of OH present in the plasma gas between each data acquisition cycle.

For HA-FANES, Harnly *et al.* reported a maximum SNR for Cu and Cd at 50 and 20 mA, respectively, when the discharge current was varied from 10 to 80 mA [125]. For the calculation of SNR, Harnly *et al.* assumed that the noise in the signal was independent of the atomization process: black-body, line, and molecular emission were negligible [125]. In a subsequent publication, Riby *et al.* reported a maximum SNR for Cr between 60 and 70 mA at 160 Torr [90]. The low SNR at low and high currents was attributed to the plasma instabilities. Riby *et al.* reported that, at low currents, the discharge fluctuated between partial and total coverage of the cathode, and at high currents, sparking occurred between the base of the cathode and the graphite furnace [90]. It should be noted that the SNR was calculated as the average peak area for triplicate determinations divided by the standard deviation of seven blank atomizations [90].

5.3.4 Figures of merit

Figure 5.8 provides the calibration graph for the determination of Pb in FAPES. Four replicate measurements were carried out for each concentration studied. The RF power used for the collection of data provided in Figure 5.8 and the rest of this study was 20 W.

In order to study the effect of analyte condensation (on the RF electrode) on figures of merit, calibration graphs were obtained at different integration times. The variation in sensitivity (slope of the calibration graph) as a function of integration time is plotted in Figure 5.9. The integration interval

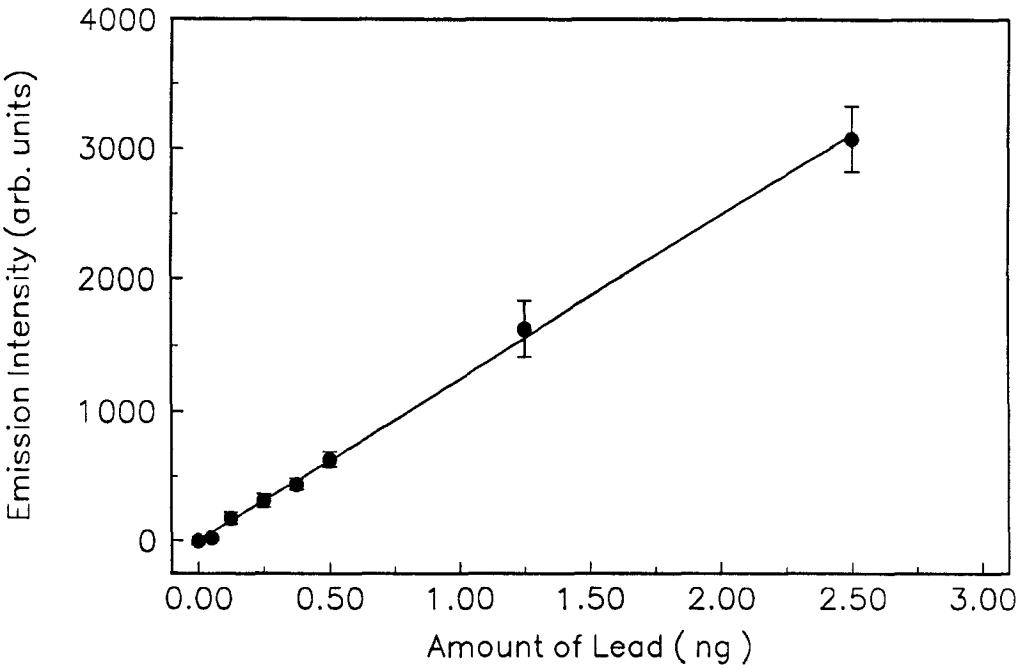

Figure 5.8. The analyte calibration graph for Pb.

was varied up to 3.5 s (from 0.5 to 4 s into the atomization step) for the blank and different analyte amounts because of the unsymmetrical temporal response of Pb with respect to the peak maximum as a result of analyte condensation on the RF electrode. Figure 5.9 shows a linear increase in sensitivity when the integration time is increased. Data provided in Figure 5.9 also show that analyte condensation on the RF electrode lowers the sensitivity of the calibration graph at shorter integration intervals as can be seen by the continued increase in sensitivity even after the first peak maximum. The values in the parentheses (Figure 5.9) give the correlation

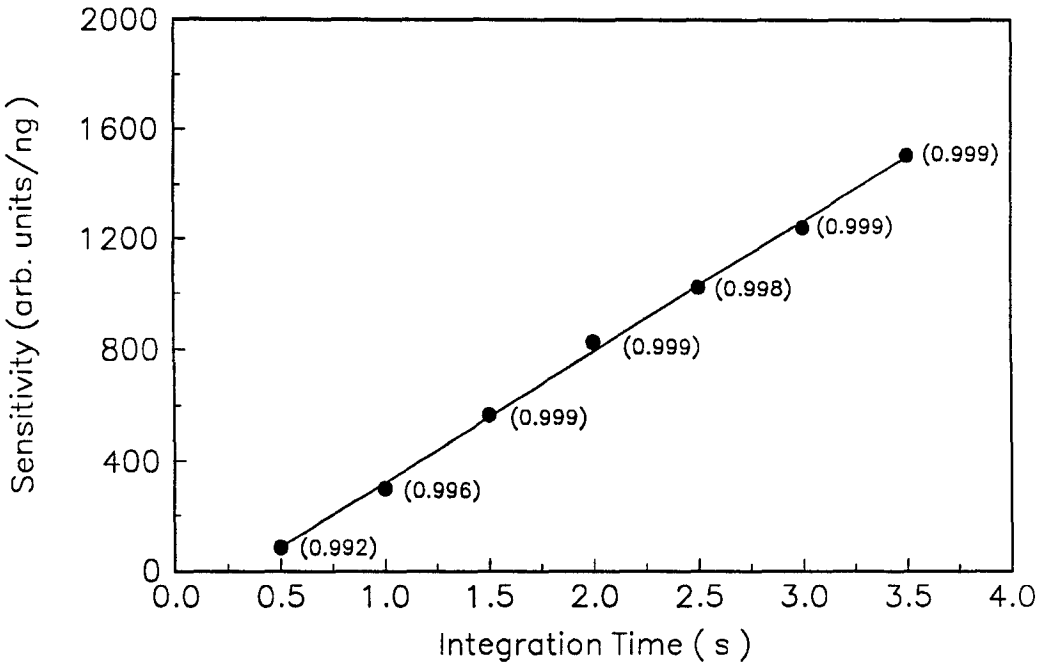

Figure 5.9. Effect of integration time on the sensitivity of the Pb emission intensity. The values in the parentheses give the correlation coefficient of the least square fit for each calibration graph.

coefficient of the least square fit for each calibration graph as a function of integration time. Loss of linearity of the calibration graph is not observed even after integration into the peak maximum of the second peak with higher amounts of Pb.

Figure 5.10 is a plot of the DL as a function of integration time. The DL is defined as the concentration of the analyte which gives a signal equal to the blank signal plus three standard deviations of the blank, and was calculated

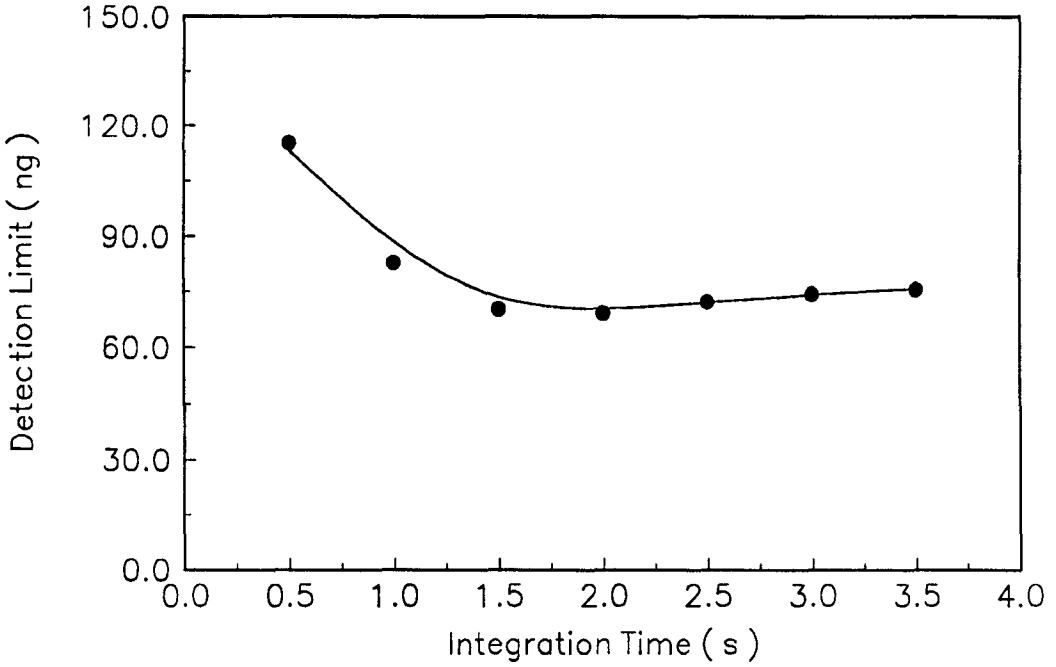

Figure 5.10. Effect of integration time on the detection limit (DL) for Pb.

using equation 5.1. The standard deviation of the blank was determined by fifteen replicates. These data illustrate that, as the integration time increases, the DL decreases and then levels off. The advantage of gain in sensitivity of having a longer integration time is counterbalanced by the high integrated flicker noise in the background. This effect of the integrated noise can be seen from the level off in the DL at longer integration times. At shorter integration times, the integrated flicker noise in the background is low.

The absolute DL calculated by using an integration time of 1 s (from 1.5 to 2.5 s) yields 65 pg and the concentration DL is 13 $\mu g\ L^{-1}$. The previously reported DL for Pb is 46 pg (peak area without the use of a chemical modifier) for FAPES [78], and 15 pg (peak area with the use of a chemical modifier) for GFAAS [147]. Sturgeon *et al.* predicted improvements of 10 to 100-fold for the DLs in FAPES by analyte atomization from a platform, use of chemical modifiers and use of an ICC, more efficient transfer optics and image coupling to a high resolution spectrometer, and background correction [78].

Precision of a Pb determination is about 7 - 10 %. This low precision is likely due to the manual pipetting of the analyte sample onto the graphite furnace side-wall, tendency of the sample droplet to spread over or run along the furnace side-wall, and non-repeatability of the analyte condensation on the RF electrode. For GFAAS with manual pipetting, precision is about 3 - 5 % (120).

It was noted that the partial integration of the Pb emission peaks yields even poorer precision. If analyte condensation on the RF electrode is not repeatable for each atomization step, then the analyte emission intensity may not be repeatable even with the integration of the whole peak. This non-repeatability of the analyte emission intensity likely arises from the temporal non-isothermality of the graphite furnace during the atomization step. The diffusion, and hence, the residence time of different portions of the atomic population in the gas-phase are dependent on the gas-phase

temperature. Therefore, the analyte emission intensity can change between each atomization step due to the non-repeatability of the analyte condensation in temporal non-isothermal conditions. Therefore, under temporal non-isothermal conditions, non-repeatability of the analyte condensation on the RF electrode is a likely contributing factor for the poor precision of the determination of Pb in FAPES.

The calibration graph given in Figure 5.8 shows a linear range of about 1.4-orders of magnitude for Pb determination by FAPES. The linear dynamic range reported by Sturgeon *et al.* for 9 analytes was about 3-orders of magnitude [78], and that reported by Smith *et al.* for Ag was 2-orders of magnitude [17]. For these studies [17,78], end-heated Massmann-type graphite furnaces were employed. It is well known that self-absorption limits the linear dynamic range when this type of end-heated Massmann-type furnaces are used in CFAES [45]. A similar situation is very likely to exist in FAPES, if one uses a short RF electrode leaving a cooler region at the open-end of the graphite furnace. In addition, if one integrates only a portion of the rising edge of the emission peak, the linear dynamic range should increase without sacrificing the DL, because self-absorption is less likely at early stages of the atomization. For GFAAS, the linear dynamic range spans over 1.5-orders of magnitude [120].

It is important to understand the limitations of these figures of merit. These figures of merit give only a measure of the excitation ability of the RF plasma source in FAPES and the detection power of the experimental

system employed for this study. These kinds of figures of merit are useful for comparing different spectrochemical sources. However, most of these kinds of so called " analytical " figures of merit reported in the literature (when the analyte to be determined was present in an isolated form, *i.e.* aqueous standard solutions) reflect direct instrumental procedures. With complex real samples, severe matrix interferences can occur, and as a result, not only the detection ability is degraded but also systematic errors can occur. Furthermore, each analyte should be studied separately because the analyte emission and the plasma background emission may depend on the nature of the analyte and the analytical wavelength.

5.4 SUMMARY

The effect of RF power, between 20 and 100 W, on the analyte emission signal and the plasma background emission is studied for the 283.3 nm Pb (I) resonance line. The time-resolved Pb-excitation temperature for 50 W helium plasma is 4560 ± 100 K. At 20 and 100 W, the Pb-excitation temperatures are 3990 ± 80 and 4840 ± 110 K, respectively.

The highest Pb emission is observed at an RF power of about 50 W. Above 50 W, the Pb emission intensity decreases. This decrease in emission intensity may be attributed to analyte losses during the pre-atomization or atomization step, changes in plasma characteristics, or an increase in ionization of Pb at high RF powers. The highest SNR and SBR are observed

at relatively low RF powers. At these low RF powers (about 20 W), analyte flicker noise is the dominant noise in the emission signal.

The absolute detection limit for Pb is 65 pg and the concentration DL is 13 $\mu g\ L^{-1}$ with a relatively slow heating rate for the graphite furnace. Precision is about 7 - 10 % for the Pb analysis by FAPES. This low precision is likely due to the manual pipetting of the analyte sample onto the graphite furnace side-wall, tendency of the sample droplet to spread over or run along the furnace side-wall, and non-repeatability of the analyte condensation on the RF electrode. Analyte condensation on the RF electrode reduces the sensitivity but shows no effect on the linearity of the analytical calibration curve.

CHAPTER 6

EFFECTS OF SODIUM CHLORIDE AND SODIUM NITRATE ON THE LEAD AND SILVER EMISSION IN FAPES

6.1 INTRODUCTION

An important characteristic of an analyte is its susceptibility to be affected by contaminants in the sample matrix during an analytical determination. In emission spectrochemical methods based on a graphite furnace for analyte atomization and vaporization and a plasma source for analyte excitation, the analyte atomization, vaporization, and excitation characteristics may be affected by matrix effects found in graphite furnace methods and those found in plasma methods.

Matrix effects in graphite furnace methods, which have been studied by using AAS, can be classified into two categories: (1) condensed-phase interferences, which are volatile compound formation, incomplete vaporization due to occlusion, refractory compound formation, and change in the rate of analyte supply, and (2) gas-phase interferences, which are shifts in the dissociation equilibria due to stable compound formation, shifts in ionization equilibria, and changes in the rate of analyte removal [148].

Matrix effects in plasma methods are broadly classified as transport (viscosity and surface tension effects), vaporization, dissociation, and ionization interferences. Additional sources of interference can occur as a result of the interferent affecting the plasma characteristics. Examples of these sources of interference are collisional excitation rate changes for the analyte due to the changes in the electron energy distribution or density in the plasma, and ambipolar diffusion due to shifts in the spatial distribution of plasma constituents [149,150].

Plasma spectrometric methods, such as FAPES and FANES, which are based on a graphite furnace for analyte atomization and vaporization, are distinct from most other common emission spectrometric methods because of the transient nature of the analyte and the interferent populations in the plasma source. In these emission spectrometric methods, the analyte and the interferent populations may have different temporal characteristics. Therefore, gas-phase interferences may not be present in some instances because the analyte and the interferent do not co-exist in the gas-phase. However, in graphite furnace methods, not only the analyte vaporization efficiency but also the interferent vaporization efficiency to the gas-phase is high. As a consequence, when the analyte and interferent co-exist in the gas-phase, interference effects in the gas-phase are expected to be severe.

To date, only a few studies have been reported on the interference effects in FAPES. Smith *et al.* reported a slight enhancement of peak area for Ag at low concentrations and a suppression at higher concentrations of both

$NaNO_3$ and NaCl [17]. The enhancement and the suppression effects were attributed to Na rather than to the counter ion. Smith *et al.* speculated that at low concentrations of Na, the signal was enhanced by a shift in the ionization equilibrium, and at higher concentrations, the free atom population of Ag was being depressed or the excitation characteristics of the plasma were modified by the presence of Na [17]. Sturgeon *et al.* determined Cd and Pb in three marine reference samples from the National Research Council (NRC) of Canada, and it was necessary to employ the method of standard additions for quantification because of matrix effects [121]. In a subsequent publication, Sturgeon *et al.* reported a large reduction in Pb emission when NaCl was present in standard solutions [123]. While the results were not conclusive about the nature of the effect of NaCl on Pb emission, experimental observations were attributed to a gas-phase effect due to the co-existence of Pb and interferents in the gas-phase, quenching of the plasma, or condensation of NaCl on the RF electrode [123]. Although it has been widely speculated that the major cause of the NaCl interference effect in FANES or FAPES methods is the gas-phase co-existence of the analyte, Na, and Cl, no mechanistic study has been reported to date. Obviously, a greater understanding at a fundamental level will be needed before these effects can be fully controlled.

This chapter presents the results of the work undertaken to study the mechanism of NaCl and $NaNO_3$ interference effects in FAPES [151]. Sodium salts constitute one family of interferents in both GFAAS and emission spectrometric methods. In this study, Pb and Ag were examined as the test

analytes because of the expected severe gas-phase interference effects for analytes with similar volatilities to Na. The effect of the addition of ascorbic and phosphoric acid, commonly used matrix modifiers for Pb in GFAAS, are also presented.

6.2 EXPERIMENTAL

A complete description of the experimental system employed to acquire atomic emission signals is given in Chapter 2 of this thesis. This experimental system and a vertical-mount for the RF electrode were employed. The following experimental methods and parameters should be noted.

6.2.1 Signal Presentation

Four replicate measurements were averaged and subjected to a 25-point Savitzky-Golay smoothing procedure [91]. Analytical parameters, such as peak area and peak width, were calculated for each sample deposition.

6.2.2 Reagents

All analyte solutions in distilled water were prepared from serial dilution of 1000 mg L^{-1} in distilled water stock solution prior to analysis. Lead and Ag solutions were prepared by dissolving analytical grade $AgNO_3$ and $Pb(NO_3)_2$

(both BDH, Toronto, Canada). Sodium solutions were prepared by dissolving analytical grade NaCl (BDH, Toronto) and $NaNO_3$ (Anachem, Portland, USA). Nitric acid solutions were prepared by using the analytical grade reagent (BDH, Toronto).

6.2.3 Procedure

A 5 μL aliquot of analyte solution was deposited onto the furnace side wall with an Eppendorf 0.5 - 10 μL UltraMicro pipette. The plasma source work-head was purged with helium (Union Carbide, Toronto, Canada). The furnace temperature was increased to 470 K in 45 s to dry, and was maintained at 470 K for another 45 s to ash the sample. This total time interval was sufficient to exclude the water vapor inside the plasma source work-head before plasma ignition. Within the next 10 s time lag, the plasma was ignited. After this time lag, the furnace temperature was ramped to 2050 K in 5 s for all determinations. The blank determinations were carried out by depositing the same volume of distilled water, or the respective interferent in distilled water (unless otherwise noted). After the analyte atomization step, a dry (without deposition) atomization step was carried out to clean the graphite furnace. Four replicate measurements were carried out for each determination.

All determinations were carried out by using atomic resonance lines of Pb (283.30 nm) and Ag (328.07 nm). Sodium emission was measured at 330.23 nm.

6.3 Results and Discussion

6.3.1 Reflected Power

Reflected power is an important diagnostic tool in plasma spectrochemical methods because the changes in reflected power indicate changes in the plasma characteristics. In FAPES, as the graphite furnace heats during the atomization step of the analyte, the plasma impedance changes, because of the evolution of thermionic electrons from the hot graphite surfaces. This change in the plasma impedance necessitates the use of an impedance matching network, which acts to maintain the reflected power at a minimum and to protect the RF power supply.

The change in the reflected power during the atomization step due to the presence of NaCl, Na, and Cl, or ionization of Na in the plasma, was studied at an RF power of 14, 20, 30, and 40 W. The results of this experiment at an RF power of 20 W for the deposition of distilled water (solid line), 160 ng of Na as NaCl in distilled water (dot line), and the temperature profile of the graphite furnace (dash line), are given in Figure 6.1. There is no significant difference between the reflected power with and without NaCl. At RF powers between 14 and 40 W, the average reflected power measured is about 1 W with some random rather than systematic fluctuations. In addition, no reflected power change is observed up to 3.2 μg of Na (as NaCl or $NaNO_3$) used in the experiments described in this chapter.

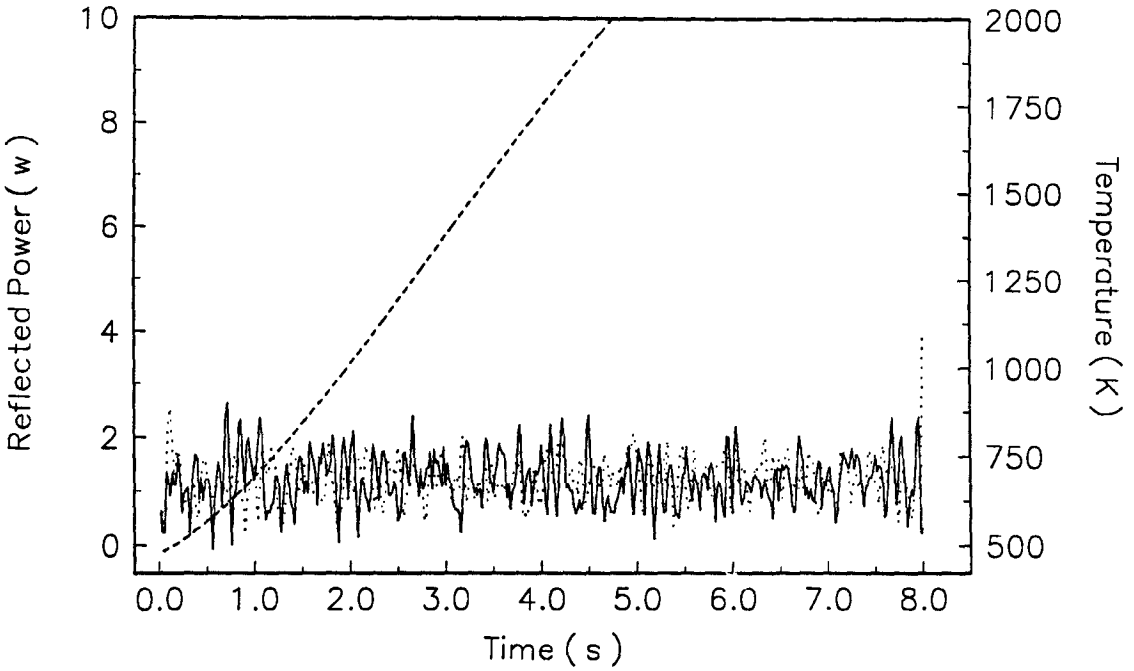

Figure 6.1. Temporal response of the reflected power at an RF power of 20 W for the deposition of distilled water (———), and 160 ng of Na as NaCl in distilled water (• • •); and the temperature profile of the graphite furnace (- - -).

Sturgeon *et al.* reported a reflected power loss when 23 μg of Na (as NaCl in 1 % HNO_3) was atomized at an RF power of 100 W [123]. However, the reflected power loss was observed not during the atomization step of the analyte but after the furnace reached a steady state temperature of 2100 K. Sturgeon *et al.* attributed this observed reflected power loss to the evolution of thermionic electrons from the RF electrode because of the lag time which occurred between the establishment of maximum reflected power and steady

state furnace wall temperature. This lag time was attributed to the radiative heating of the RF electrode by the furnace wall [123].

It should be noted here that, for the experimental system described in this thesis, a reflected power loss is observed even before the furnace reaches 2100 K at RF powers higher than 75 W (Sections 2.1.2 and 5.3.1). This observation can be attributed to the evolution of thermionic electrons from the RF electrode because the onset of the reflected power loss is dependent on the RF power. Furthermore, some changes in the temporal characteristics of the CO^+ emission during the atomization step are also due to the evolution of thermionic electrons from the RF electrode (Section 3.3.3). The observed reflected power loss during the atomization step is most likely due to a higher temperature of the RF electrode for 75 W plasma employed in the work described in this thesis. This higher temperature of the RF electrode can be attributed to an efficient RF power coupling to the plasma source. However, the extent of the RF power coupling efficiency is not known at present. Sturgeon *et al.* employed a manual impedance matching network in their experimental system, and reported 85 % internal loss of RF power within the RF tuner [79].

6.3.2 Temporal Response of Na (as NaCl and $NaNO_3$)

Figure 6.2 provides the temporal response of the Na emission signal for 160 ng of Na as NaCl (solid line) and 160 ng of Na as $NaNO_3$ (dash line) deposited on the furnace wall at an RF power of 20 W. The temporal

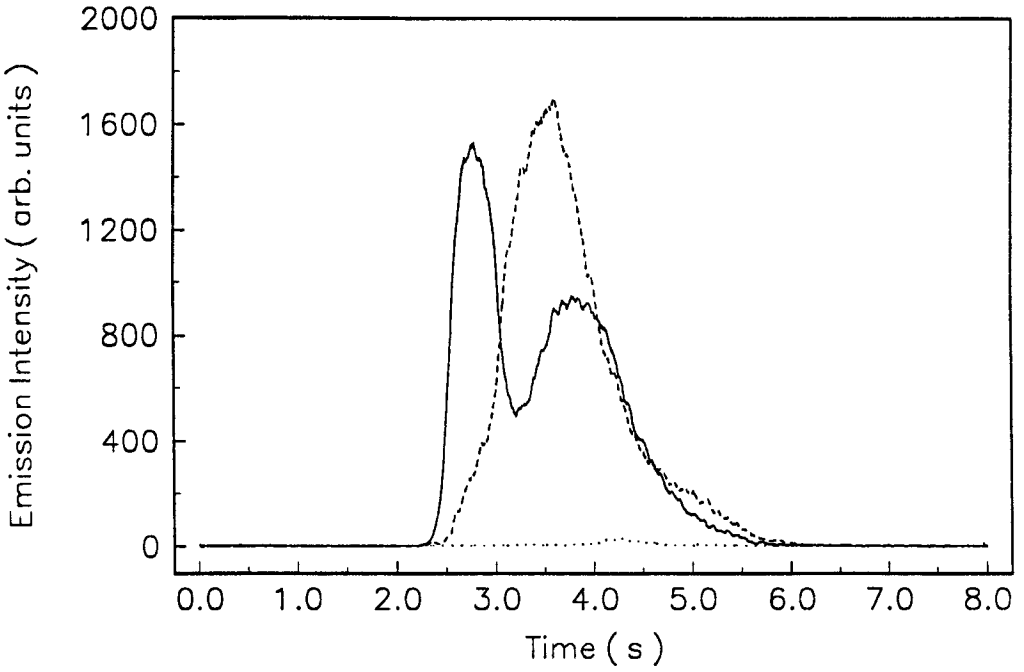

Figure 6.2. Temporal response of the Na emission signal at an RF power of 20 W for the deposition of 160 ng of Na as NaCl (——), and 160 ng of Na as $NaNO_3$ (- - -); and water blank (· · ·).

response of the emission signal of Na as NaCl is different from that of Na as $NaNO_3$. For NaCl, there are two peaks, and the more intense first peak has an appearance temperature of 1080 K. For $NaNO_3$, there is a single broad peak and has a similar appearance temperature compared with Na as NaCl.

When NaCl is deposited on the furnace wall, Na is likely formed from the gas-phase dissociation of NaCl:

$$NaCl_{(s)} \longrightarrow NaCl_{(g)} \longrightarrow Na_{(g)} + Cl_{(g)} \quad (6.1).$$

The existence of two peaks for the Na signal from NaCl is indicative of the presence of Na in the gas-phase at two different stages. The first peak is from initial vaporization from the furnace wall and gas-phase dissociation of NaCl to form Na (equation 6.1) and the second peak is most likely from NaCl (and Na) which has condensed on the RF electrode and subsequent second-surface vaporization into the gas-phase (similar to PbO, Section 4.3.2).

Campbell and Ottaway suggested that, in GFAAS, Na can be formed from carbon reduction of Na_2O [104];

$$4NaNO_{3(s)} \longrightarrow 2Na_2O_{(s)} + 4NO_2 + O_2 \quad (6.2),$$

$$\text{and } Na_2O_{(s)} + C \longrightarrow 2Na_{(g)} + CO \quad (6.3).$$

For $NaNO_3$ in FAPES, the broad Na peak shown in Figure 6.2 may be due to an overlap of Na signals from the initial vaporization of Na from the furnace wall (equation 6.3), and second-surface vaporization subsequent to condensation on the RF electrode. It is also possible that the broad Na peak from $NaNO_3$ may be largely due to the second-surface vaporization of Na from the RF electrode rather than from the furnace wall because of an instantaneous condensation of Na on the RF electrode.

The condensation of Na on the graphite surfaces has been also observed in GFAAS studies. In a study of spatial distribution of Na atoms within the graphite furnace, Stafford and Holcombe observed lower Na atom density near the furnace wall than in the center of the furnace [152]. The observed Na atom gradients were attributed to a gas-phase dissociation mechanism, and strong interaction of atomic Na with graphite [152]. Huie and Curran reported adsorption of Na atoms on the upper-wall of the furnace at a rate higher than the release of Na atoms during the early stages of the atomization [153].

6.3.3 Effect of NaCl and $NaNO_3$ on the Pb Emission Intensity

Interference effects of Na, an easily ionizable element (EIE), have been extensively studied in flame AES and plasma spectrometry. In flame AES, an enhancement of the atomic emission intensity for alkali metals has been observed as a result of a shift in the ionization equilibrium toward the atomic form [154]. In plasma source emission spectrometry, both enhancement and suppression of the analyte emission signal have been observed [155-163]. These observations have been attributed to various modifications of plasma characteristics when Na is present. However, the root cause of these observed matrix effects is not well understood, and is still the subject of considerable debate. In general, the effect of EIE interferences found in the plasmas was to enhance the atomic emission, and has been attributed to ionization suppression or changes in the plasma characteristics rather than

to a chemical effect on the analyte because of the high temperatures of plasma sources.

Figure 6.3 depicts the temporal response of the Pb emission signal for 0.5 ng of Pb (solid line), 0.5 ng of Pb and 160 ng of Na as NaCl (dash line), and 0.5 ng of Pb and 160 ng of Na as $NaNO_3$ (long-dash line) deposited on the furnace wall at an RF power of 20 W. The effect of both $NaNO_3$ and NaCl on the Pb emission signal is to reduce the emission signal relative to that without the interferent.

The appearance and peak temperatures for Pb in the presence of NaCl are the same as those for Pb alone. Moreover, the normalized temporal responses of Pb, with and without NaCl, coincide within the error of the measurement. These observations indicate that in the presence of NaCl, a reduction in the excitation ability of the plasma, or a decrease in the analyte atom population in the plasma, or both, cause the reduction of the Pb emission intensity in FAPES.

Gas-phase co-existence of the analyte and the interferents can be studied by the comparison of temporal responses depicted in Figures 6.2 and 6.3. The temporal response of Na (as NaCl) in Figure 6.2, and that of Pb in Figure 6.3 show that Na vaporizes later in time than Pb. Therefore, Pb, Na, and Cl co-exist in the gas-phase only during the later stages of Pb atomization while Pb is diffusing out of the plasma. The non-overlap of temporal responses for Na as NaCl (Figures 6.2) and Pb (Figures 6.3), and

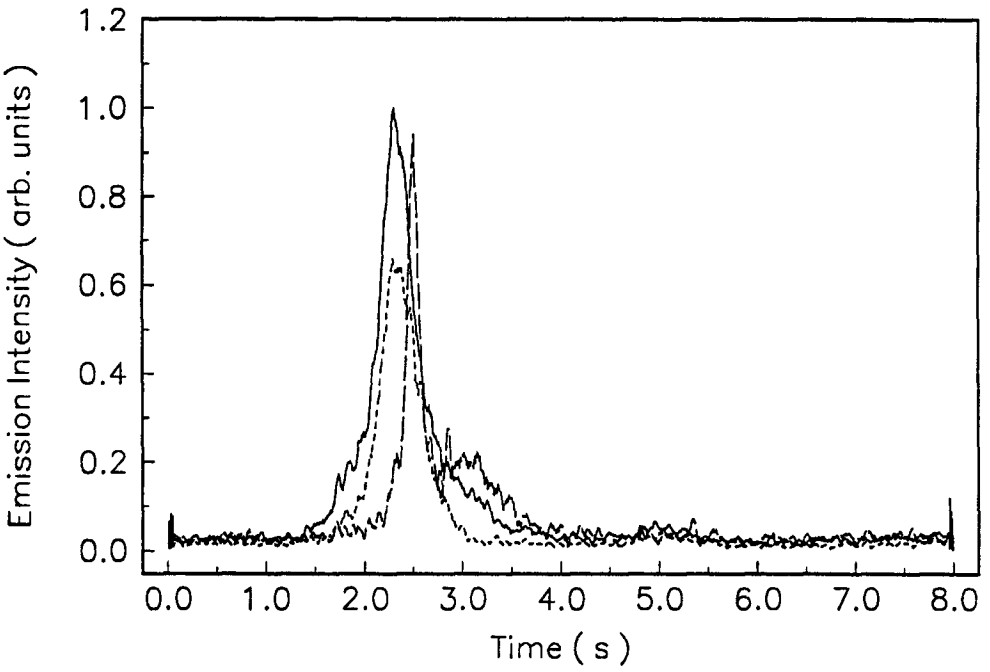

Figure 6.3. Temporal response of the Pb emission signal at an RF power of 20 W for the deposition of 0.5 ng of Pb (——), 0.5 ng of Pb and 160 ng of Na as NaCl (- - -), and 0.5 ng of Pb and 160 ng of Na as $NaNO_3$ (— —).

the reduction of Pb emission intensity when Na (as NaCl) is present, suggest that the major cause of NaCl interference effect on Pb in FAPES is due to a decrease in the Pb population in the plasma. It should be noted here that an early appearance of Pb is observed in FAPES compared with the appearance of Pb in GFAAS (Section 4.3.2).

For GFAAS, Czobik and Matousek studied the effects of metal and alkali chlorides, including NaCl, on atomic absorption signals of Pb and Ni [164].

In the presence of 0.2 to 20 ng of NaCl, the signal for Pb showed a decrease in the peak absorbance and a shift to lower appearance and peak temperatures. They attributed this signal modification to a depletion of analyte atom population in the gas-phase due to the formation of Pb chlorides and to a carrier effect of NaCl on Pb. However, no NaCl interference effect was observed for Ni because NaCl and its decomposition products were lost from the furnace before the Ni atomization temperature was reached [164]. Slavin and Manning reported a decrease in integrated absorbance for Pb as the amount of NaCl was increased [128]. This effect was not observed to be significant when a L'vov platform was used except at very high NaCl amounts (about 0.1 %). The effect of NaCl was attributed to the formation of volatile Pb chlorides in the condensed phase which are lost during the ashing stage [128], and the formation Pb chlorides in the gas-phase [165]. Welz *et al.* used a dual-cavity platform to study the interference effects of NaCl on Pb [129]. Welz *et al.* suggested that while some Pb is lost as volatile Pb chlorides during the ashing stage, Pb was also lost due to the analyte vapor expulsion with the vaporization of the NaCl matrix [129].

Therefore, it appears that the most significant effect of NaCl in GFAAS is not due to Na, but rather to the counter ion: chloride. The interfering chlorides form stable molecular species with the analyte; *i.e.*, " analyte-chloride ". These chloride interferences are most severe for the volatile elements because the dissociation of analyte-chlorides in the gas-phase is less likely at lower temperatures. This is the reason that the use of the L'vov platform is useful for these situations. In addition, at higher

heating rates of the graphite furnace, a higher gas-phase temperature is attained so rapidly that these molecular species can be dissociated before dissipating out of the furnace. However, it is difficult to determine whether the formation of analyte-chlorides is in the condensed-phase prior to vaporization or in the gas-phase after the vaporization from the furnace wall.

In an attempt to determine whether the effect of NaCl originates in the condensed-phase or gas-phase, Pb is deposited on the furnace wall with and without NaCl deposited on the RF electrode. Even though the atomic populations of Pb, Na, and Cl do not co-exist in the plasma, it is possible that undissociated NaCl is present in the plasma at earlier times (compared with the appearance of Na) because dissociation of NaCl in the gas-phase is dependent on the gas-phase temperature. It should be noted here that analytes deposited on the RF electrode have a similar appearance time to those deposited on the furnace wall when a 20 W plasma is used (Chapter 4). Therefore, no significant difference in the temporal response of Na is expected when the NaCl is deposited on the RF electrode. In fact, when the analyte deposited on the furnace wall has an appearance time before 3 s into the atomization step, the appearance time can shift to a earlier time when deposited on the RF electrode.

When 0.5 ng of Pb is deposited on the furnace wall and 160 ng of Na as NaCl is deposited on the RF electrode at an RF power of 20 W, the same integrated emission intensity is obtained compared with that with Pb alone. This observation and the temporal non-overlap of atomic populations of Pb,

Na and Cl, suggest that the effect of Na (as NaCl) is not due to the formation of Pb chloride in the gas-phase. Furthermore, similar integrated intensities with and without NaCl deposited on the RF electrode eliminate the possibility of a reduction in excitation ability of the plasma when NaCl is present (also see the effect of RF power). These observations indicate that loss of Pb chloride (formed in the condensed-phase) during the ashing step and the slow atomization step is the most likely cause for the reduction in Pb emission in FAPES.

However, for GFAAS, it has been shown that Pb samples with NaCl can be ashed up to about 800 K without any significant loss of the absorbance signal [128,129]. For the experiments described in this chapter, sample was ashed at 470 K. Therefore, the loss of Pb as chlorides during the slow atomization step may be the major cause of Pb signal suppression in this study. When the analyte atomization process goes through an analyte-chloride formation step and vaporization of analyte-chlorides occurs at a temperature lower than the appearance temperature, it is essential that the graphite furnace reaches the final temperature quickly in order to prevent any analyte losses.

The effect of $NaNO_3$ on the Pb emission signal (Figure 6.3) is more complex than that observed for NaCl. The Pb signal in the presence of $NaNO_3$ appears at a later time and has a narrower peak width. When 0.5 ng of Pb is deposited on the furnace wall and 160 ng of Na as $NaNO_3$ is deposited on the RF electrode at an RF power of 20 W, a reduction in

emission is observed but the peak shape, appearance temperature, and peak temperature are the same as those obtained without $NaNO_3$ deposited on the RF electrode. The identical peak shapes for Pb with and without $NaNO_3$ deposited on the RF electrode, and the difference in peak shapes with and without $NaNO_3$ deposited on the furnace wall (Figure 6.3) suggest that the effect of $NaNO_3$ on Pb partly takes place in the condensed-phase. The delay in the onset of the Pb emission signal in the presence of $NaNO_3$ (Figure 6.3) is probably due to the entrapment of PbO in the $NaNO_3$ matrix. Therefore, PbO is prevented from vaporizing from the furnace wall and the narrow peak width of the Pb emission signal is due to the rapid expulsion of PbO from the $NaNO_3$ matrix at higher temperatures. The reduction in the emission intensity of Pb in the presence of $NaNO_3$ can be attributed to a decrease in free atom population in the gas-phase, probably due to changes in the gas-phase dissociation equilibrium of PbO. The gas-phase dissociation equilibrium of PbO can be affected by a change in the gas-phase O_2 concentration because of the decomposition products of $NaNO_3$, according to equation (6.2).

Effects of $NaNO_3$ matrices on the atomic absorption signal, in particular on Pb, were studied in GFAAS. Eklund and Holcombe showed that large amounts of nitrate can reduce the signal for Ag, Cu, and Ga in GFAAS as a result of gas-phase oxidation of the metal by NO_2 and O_2 formed during ashing and atomization steps [166]. Cedergren *et al.* reported a depressive effect and narrowing of the absorbance peak width of Pb in GFAAS when $NaNO_3$ is present in the sample [112]. These observations were attributed to

an increase in partial pressure of O_2 formed from the decomposition products of $NaNO_3$. Cedergren *et al.* also reported that in the presence of CO, the Pb peak height increases without any apparent peak shape difference when $NaNO_3$ is present [112]. This effect of CO was attributed to a reduction in O_2 partial pressure. Holcombe *et al.* reported the formation of a double peak for Pb when a 100-fold excess of NO_3^- (as $NaNO_3$) is present and delayed atomization in the presence of 1000-fold excess of NO_3^- [167]. This late shift was attributed to an increase in the sticking coefficient of Pb to the oxygenated surface. However, Sturgeon and Berman suggested that the observed shift is due to the suppression of thermal dissociation of analyte oxides [111]. In a later study, Bass and Holcombe attributed the shifts in absorbance signals to the presence of gas-phase CO and CO_2 [113]. In summary, these observations indicate both condensed and gas-phase effects on Pb in the presence of $NaNO_3$ for GFAAS.

Figure 6.4 depicts the effect of RF power on the interference effect of 160 ng of Na (as NaCl and $NaNO_3$) on the emission signal for 0.5 ng of Pb in FAPES. The emission intensity for the analyte alone is arbitrarily given a value of 1. For Pb in NaCl and $NaNO_3$, the magnitude of the interference effect is essentially the same over the power range 20 to 40 W, although it becomes a little less significant as RF power is increased over this range. This insignificance of RF power on the interference effect indicates a loss of molecular species (for example, Pb chlorides and PbO) without dissociating in the plasma. For the thermal dissociation of these molecular species, and hence, to observe a reduced interference effect, plasma temperature should be

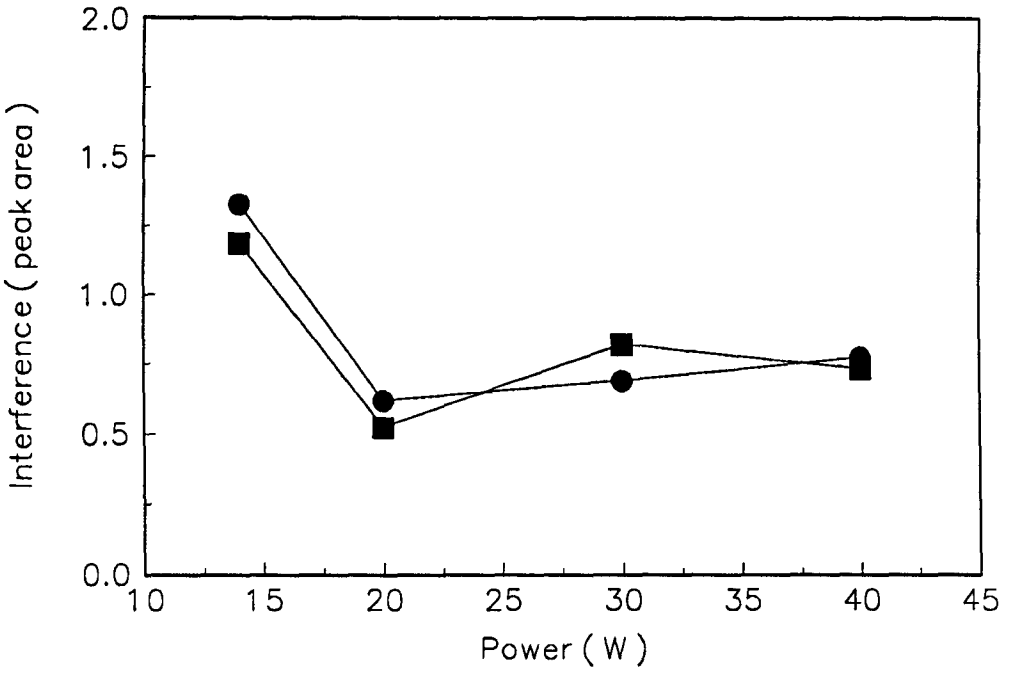

Figure 6.4. Interference effect of 160 ng of Na as NaCl (●) and 160 ng of Na as $NaNO_3$ (■) on the Pb emission intensity as a function of RF power.

increased significantly when the RF power is changed from 20 to 40 W. The gas kinetic temperatures reported by Sturgeon *et al.* were independent of the RF power over the range 50 - 100 W [80]. The minimal effect of RF power on the interference effect of $NaNO_3$ on Pb also indicates that it is not the RF power but the gas-phase composition that limits the gas-phase dissociation of PbO in FAPES.

An important feature of the plot in Figure 6.4 is that at 14 W, there is an enhancement in the emission for Pb in the presence of both NaCl and

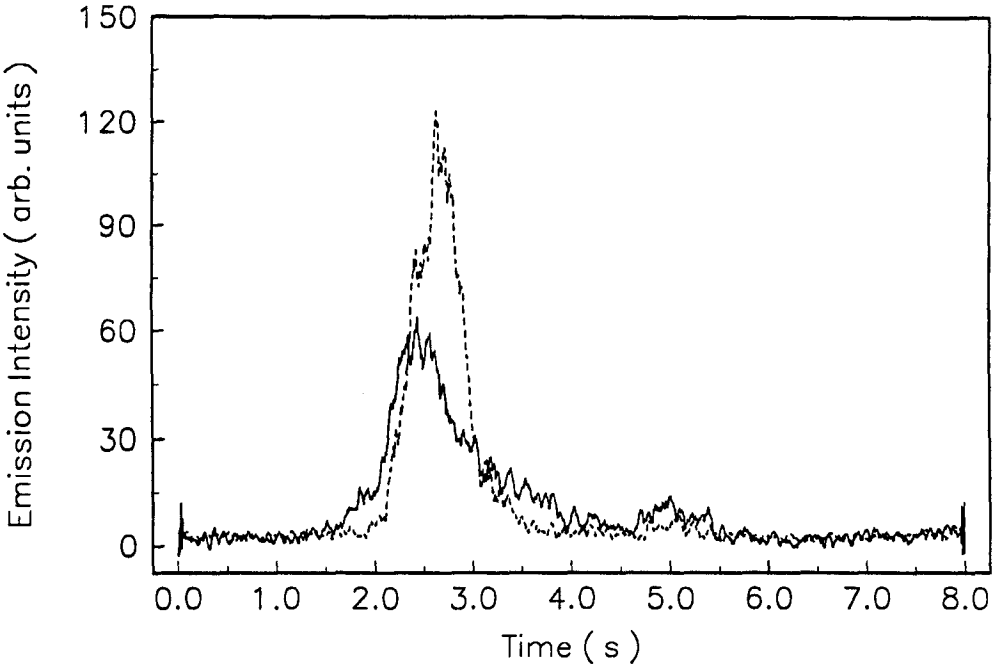

Figure 6.5. Temporal response of the Pb emission signal at an RF power of 14 W for 0.5 ng of Pb (——) and 0.5 ng of Pb and 160 ng of Na as NaCl (- - -).

$NaNO_3$. The Pb emission signals with (solid line) and without (dash line) 160 ng of Na as NaCl at an RF power of 14 W are provided in Figure 6.5. It is clear that in contrast to higher powers, the signal is enhanced at 14 W. A similar effect is seen with $NaNO_3$ as the contaminant. Figure 6.5 also shows a slight late shift in the temporal profile. This enhancement of emission at 14 W should be related to an increase in the analyte population in the gas-phase or to an enhancement in the excitation ability of the plasma. However, cause of this effect is not known at present, and needs further study.

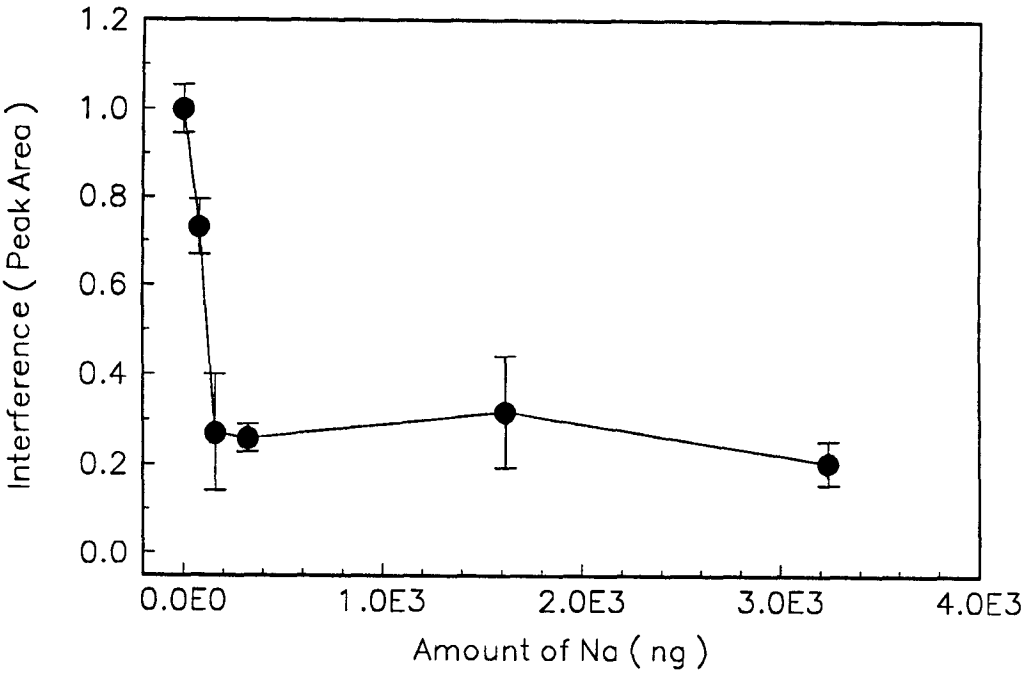

Figure 6.6. Interference effect on the Pb emission intensity at an RF power of 20 W as a function of amount of Na as NaCl.

Figure 6.6 depicts the interference effect from different amounts of Na (as NaCl) on the Pb emission intensity from 0.5 ng of Pb at an RF power of 20 W. It can be seen that even small amounts of Na cause a marked depression in the Pb emission. As the amount of the interferent increases, the interference reaches a fairly stable level. Sturgeon *et al.* also observed a large reduction of Pb intensity even with a small amount of NaCl [123].

It should be noted that the temporal response for 0.5 ng of Pb and 160 ng of Na as NaCl in 1% HNO_3 (v/v) is similar to that of 0.5 ng Pb and 160 ng of Na as $NaNO_3$ in pure aqueous solution (Figure 6.3). These similar peak shapes are because of the conversion of NaCl to $NaNO_3$ in the presence of HNO_3. A similar observation for Pb in GFAAS was reported by Frech and Cedergren [168]. Nitric acid is commonly used in digestion procedures in biological and environmental sample analyses, preceding the determination by GFAAS.

6.3.4 Effects of NaCl and $NaNO_3$ on the Ag Emission intensity

Figure 6.7 provides the temporal response of the Ag emission signal for 0.25 ng of Ag (solid line), 0.25 ng of Ag and 160 ng of Na as NaCl (dash line), and 0.25 ng of Ag and 160 ng of Na as $NaNO_3$ (dot line) deposited on the furnace wall at an RF power of 20 W. The effect of both NaCl and $NaNO_3$ on Ag signal is to decrease the integrated emission intensity relative to that without the interferent. The magnitude of the reduction in Ag emission is much greater for $NaNO_3$ compared with NaCl, and hence, NO_3^- is a major cause for Ag signal suppression. Both Na containing interferents also shift the Ag peak temperatures to lower values. An additional feature of the Ag temporal response is that the emission profile for Ag almost directly overlaps with the emission profile for Na (Figure 6.2) when NaCl is present.

The rising edge of the Ag emission signal from a pure aqueous solution of $AgNO_3$ (Figure 6.7) is different from that observed from $AgNO_3$ in

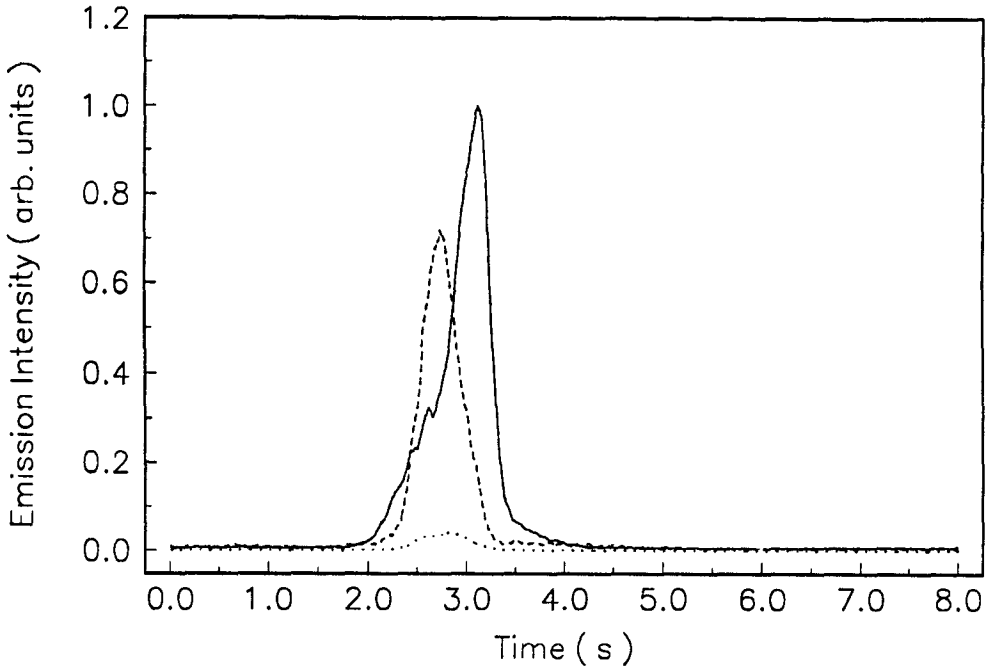

Figure 6.7. Temporal response of the Ag emission signal at an RF power of 20 W for 0.25 ng of Ag (———), 0.25 ng of Ag and 160 ng of Na as NaCl (- - -), and 0.25 ng of Ag and 160 ng of Na as $NaNO_3$ (• • •).

1 % (v/v) HNO_3 (Section 4.3.1). In a study on the mechanism of vaporization of Ag in GFAAS, a change in Ag peak shapes was reported and was attributed to the changes in the surface topology of Ag by chemisorbed O_2 [97]. Gold, with similar atomization characteristics to Ag, showed an unresolved double peak in Ar/O_2 for GFAAS compared with Ar alone, which was attributed to a surface effect of graphite [111]. However, for FAPES, the cause of this observed difference in peak shapes is not known at present, and needs further study.

Figure 6.8 depicts the effect of RF power on the interference effect of 160 ng of Na (as NaCl and $NaNO_3$) on the Ag emission intensity for 0.25 ng of Ag in FAPES. Similar to Pb (Figure 6.4), the effect of NaCl is essentially independent of the magnitude of the RF power, thus the interference effect is constant and not proportional. This constant interference effect as a function of RF power indicates a common interference effect for both Ag and Pb in the presence of NaCl; *i.e.,* formation of analyte-chlorides in the condensed-phase. It should be noted that both AgCl and PbCl have similar dissociation energies (3.2 and 3.1 eV respectively). It should also be noted that an identical number of moles of Pb and Ag (0.0023 n mol) were used in these experiments, and hence, the analyte to interferent molar ratio is the same for both Pb and Ag. The effect of RF power also shows that the NaCl interference effect is not due to any changes in excitation characteristics or a reduction in RF power coupled to the plasma.

For Ag in $NaNO_3$ (Figure 6.8), the interference effect is severe at RF powers less than 20 W, and becomes less significant as the RF power is increased to 40 W. This observation is in contrast to that for Pb in $NaNO_3$. When Ag is present in $NaNO_3$, a decrease in the gas-phase free Ag atom population is possible, due to the oxidation of gaseous Ag to form Ag_2O by NO_2 and O_2 formed from decomposition of $NaNO_3$ (equation 6.2) as mentioned previously [166]. The reduction of interference as the RF power increases suggests that gaseous Ag is lost as Ag_2O at low RF powers, and the dissociation of relatively unstable Ag_2O is increased at high RF powers (*i.e.,* an increase in free Ag atom population in the gas-phase). The bond

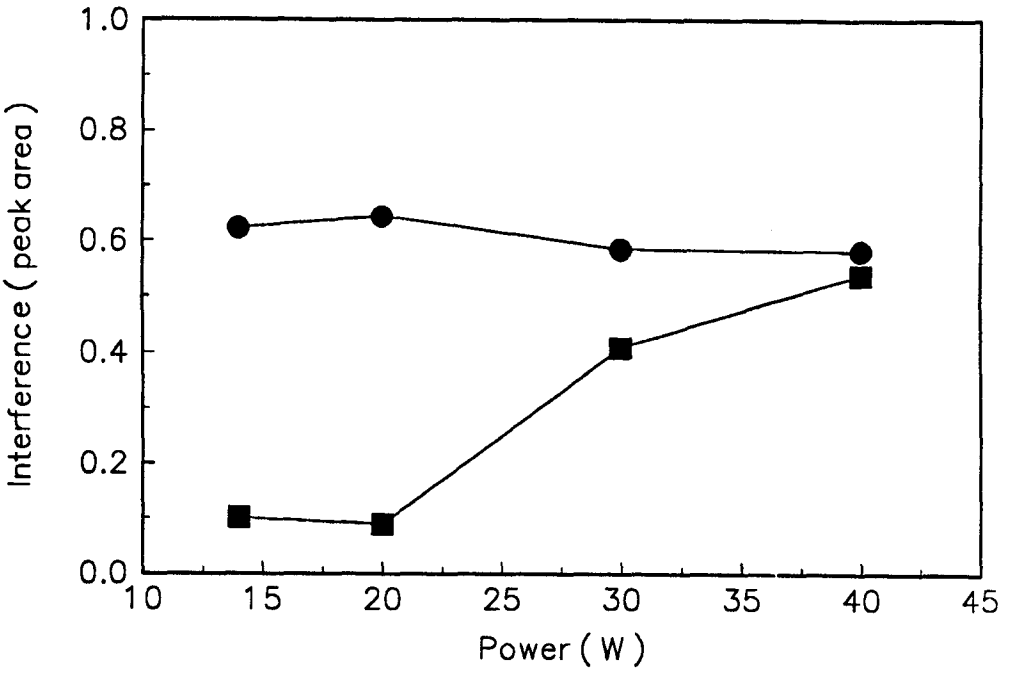

Figure 6.8. Interference effect of 160 ng of Na as NaCl (●) and 160 ng of Na as $NaNO_3$ (■) on the Ag emission intensity as a function of RF power.

dissociation energy of AgO is 2.3 eV, compared with that of PbO (3.8 eV) [81].

Figure 6.9 depicts the interference effect from different amounts of Na (as NaCl) on the Ag emission intensity for 0.25 ng of Ag at an RF power of 20 W. Similar interference effects for both Pb (Figure 6.6) and Ag (Figure 6.9) are also consistent with a common effect causing signal suppression when NaCl is present. In addition, except at 14 W, the interference effect of NaCl on both Ag (Figure 6.8) and Pb (Figure 6.4) as a function of RF power

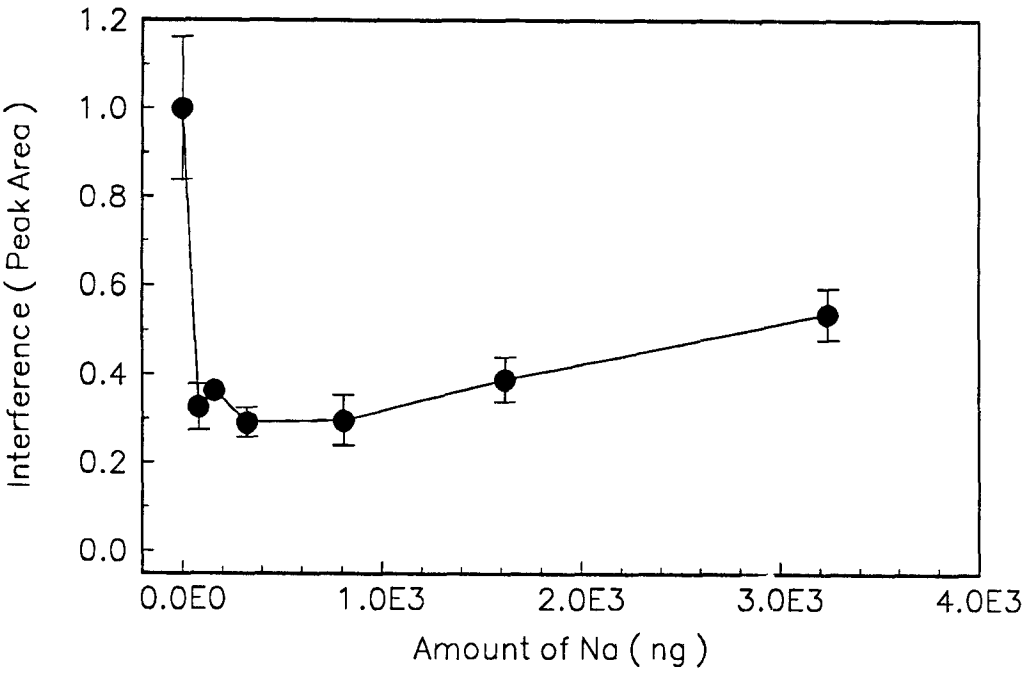

Figure 6.9. Interference effect on the Ag emission intensity at an RF power of 20 W as a function of amount of Na as NaCl.

validates this notion of a common interference effect: loss of analyte-chloride during the slow atomization of the analyte. However, as the amount of NaCl increases, the interference effect shows a marginal decrease relative to low amounts of the interferent (Figure 6.9), probably due to the ionization suppression of Ag in the presence of large amount of Na as an EIE. It should be noted that Ag and Na atomic populations co-exist in the gas-phase for Ag-NaCl system. An enhancement of Ag emission was also reported for nitrous oxide-acetylene flame when EIEs were present and was attributed to ionization suppression of Ag in the flame [169]

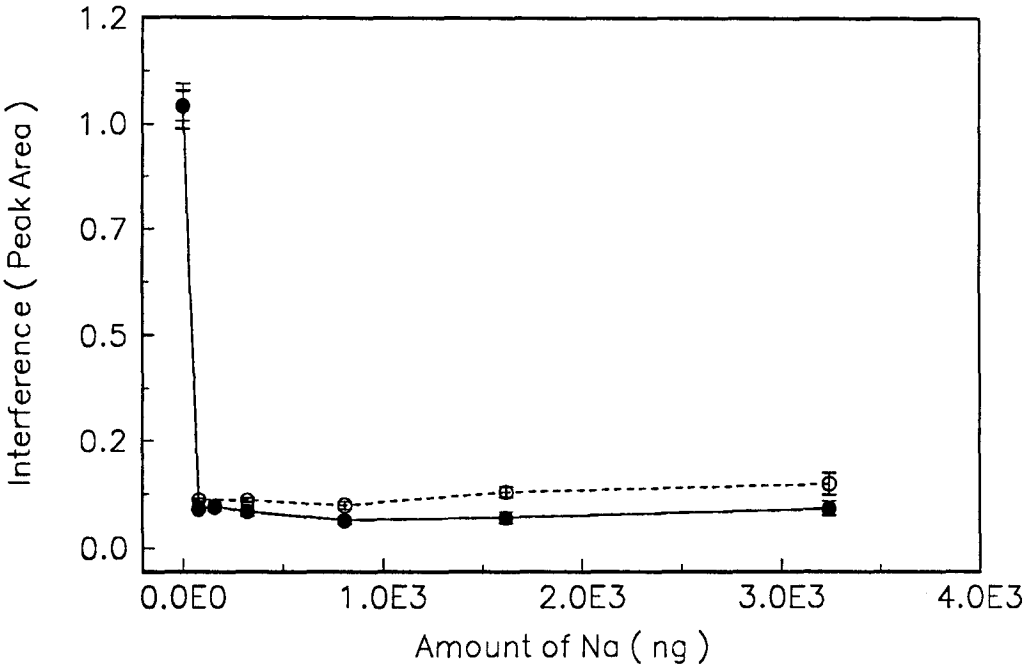

Figure 6.10. Interference effect on the Ag emission intensity at an RF power of 20 W as a function of amount of Na as NaCl in 1 % HNO_3 (○), and Na as $NaNO_3$ (●).

Figure 6.10 depicts the interference effect on Ag emission from different amounts of NaCl in 1 % (v/v) HNO_3 and $NaNO_3$ in water at an RF power of 20 W. Even with very small amounts of interferent, the Ag emission intensity is greatly depressed. Data provided in Figure 6.10 show that the effect of NaCl in HNO_3 and $NaNO_3$ is similar because of the conversion of NaCl to $NaNO_3$ by HNO_3 during the ashing stage or atomization stage.

In contrast to the study by Smith *et al.* [17], the work presented in this thesis indicates two different interferent mechanisms from NaCl and $NaNO_3$ on Ag. In the study by Smith *et al.*, analyte and interferents (both NaCl and $NaNO_3$) were prepared in dilute HNO_3. In the presence of HNO_3, NaCl is converted to $NaNO_3$ during the ashing step of the sample as mentioned previously. This conversion is most likely the reason for similar effects observed for both NaCl and $NaNO_3$ [17]. However, Smith *et al.* reported only a 50 % reduction of Ag emission (peak area) even when 2.3 μg of $NaNO_3$ (in dilute HNO_3) was present in the sample. It should be noted that the RF plasma source was operated at 27 MHz, and the RF power delivered to the plasma was not measured [17]. Furthermore, 8 pg of Ag was deposited with various amounts of interferents, and the blank determination was carried out by depositing deionized water only.

6.3.5 Effects of ascorbic acid and phosphoric acid

Ascorbic acid has been used as a matrix modifier for Pb determinations in GFAAS [99,170,171]. McLaren and Wheeler reported that the presence of ascorbic acid causes the early appearance of the Pb signal in GFAAS with a doubling of peak [99]. Tominaga and Umezaki reported the appearance of a double peak in the presence of 0.05 % (w/v) ascorbic acid and a single peak with a lower appearance temperature when 5 % (w/v) ascorbic acid was present [171]. Since these findings, a number of studies have been reported on the mechanism of ascorbic acid effect on the Pb signal in GFAAS [103,111,114].

The interest on the effect of ascorbic acid on Pb emission in FAPES stems from the observation of early appearance of Pb emission signal compared with the appearance of atomic absorption signal (Section 4.3.2). This early appearance is attributed to the difference in the gas-phase composition in FAPES and GFAAS. This study was undertaken to determine the effect of gaseous decomposition products of ascorbic acid on the Pb emission signal in FAPES.

Figure 6.11 depicts the effect of different concentrations of ascorbic acid on the temporal response of the Pb emission signal for 0.5 ng of Pb deposited on the furnace wall at an RF power of 20 W. The appearance and peak temperatures are the same with and without 0.25 % (w/v) ascorbic acid. However, a late shift in the peak temperature can be seen in the presence of 1.5 % (w/v) ascorbic acid (long-dash line).

Figure 6.12 presents the peak area of the Pb emission signal as a function of ascorbic acid concentration. An enhancement of peak area at 0.25 % (w/v) ascorbic acid followed by a gradual decrease as the ascorbic acid concentration is increased, are observed. The effect of CO on the gas-phase dissociation of PbO is given in the following equilibria (also see Section 4.3.2);

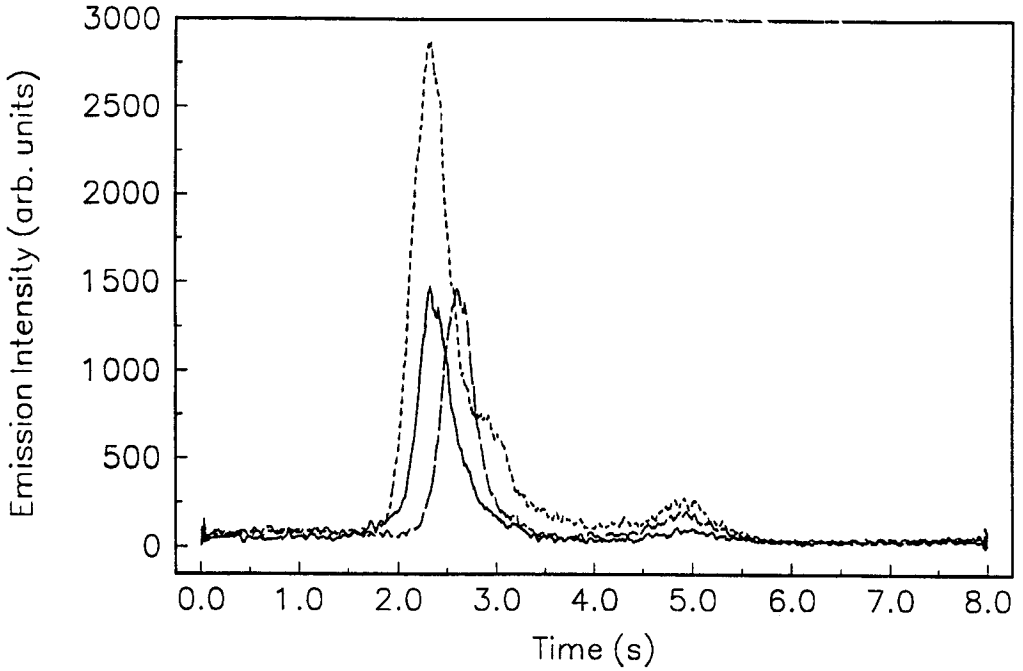

Figure 6.11. Temporal response of the Pb emission signal at an RF power of 20 W for 0.5 ng of Pb (———), 0.5 ng of Pb in 0.25 % (w/v) ascorbic acid (- - -), and 0.5 ng of Pb in 1.5 % (w/v) ascorbic acid (— —).

$$2PbO_{(g)} \rightleftharpoons 2Pb_{(g)} + O_2 \qquad (6.4),$$

$$\text{and} \quad O_2 + 2CO \rightleftharpoons 2CO_2 \qquad (6.5).$$

The effect of CO and CO_2 concentrations on the gas-phase dissociation of PbO is opposing. When CO concentration is increased, O_2 concentration decreases, which leads to a shift in equilibrium (6.4) to right. The enhancement of Pb emission in the presence of 0.25 % (w/v) ascorbic acid,

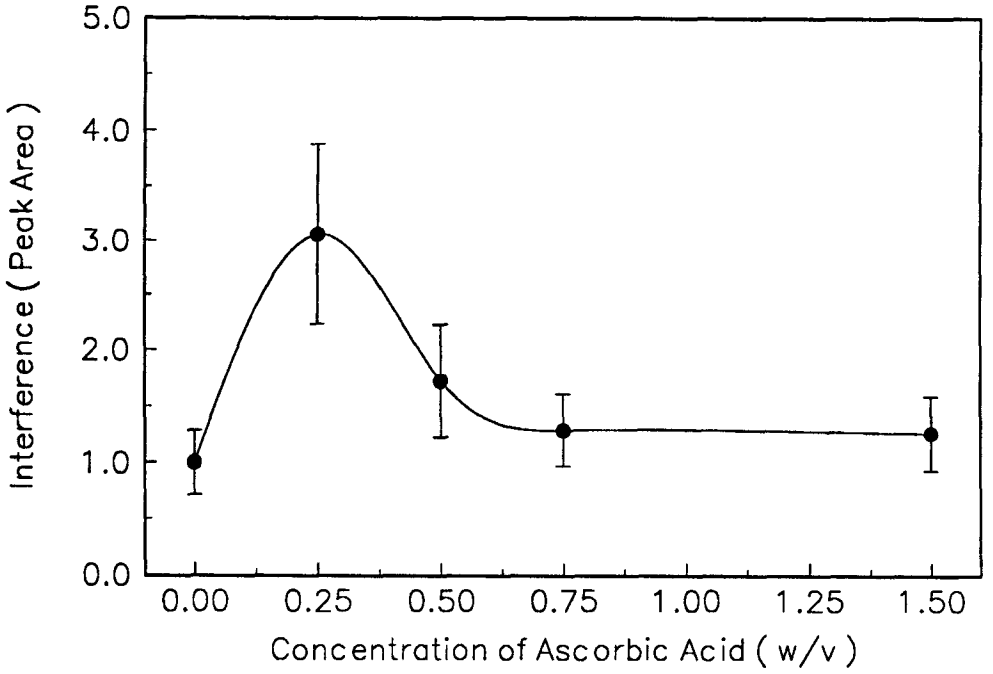

Figure 6.12. Interference effect on the Pb emission intensity at an RF power of 20 W as a function of concentration of ascorbic acid.

can be attributed to an increase in the CO concentration, and hence, a decrease in O_2 concentration. However, at high CO_2 concentrations, equilibrium (6.5) may be shifted to left. The depression effect and the late shift of the Pb temporal response can be attributed to an increase in the CO_2 concentration as the ascorbic acid concentration is increased.

The late shift of Pb in FAPES at higher concentrations of ascorbic acid differs from GFAAS observations where an early shift has been reported. This difference in appearance temperature can be attributed to the difference

in the gas-phase concentrations of O_2 and CO, due to the plasma and to the effect of ascorbic acid. It seems that the plasma has effectively increased the CO concentration (similar to the effect of ascorbic acid in GFAAS, also see Sections 3.3.2 and 4.3.2), and the effect of ascorbic acid in FAPES is to increase the CO_2 concentration such that the net effect is a suppression of Pb emission and a late shift for the appearance of Pb. A late shift in the appearance of Pb atomic absorption signal was reported when CO_2 was added to the purge gas [102].

Figure 6.13 depicts the effect of increasing concentration of ascorbic acid on the temporal response of the Ag emission signal for 0.25 ng of Ag deposited on the furnace wall at an RF power of 20 W. When ascorbic acid concentration is increased, there is a late shift in the peak temperature but no effect on the appearance temperature is observed. At higher concentrations of ascorbic acid, Ag emission is an overlap of two peaks. When atomic absorption is measured without the plasma (AA at an RF Power of 0 W), no peak shift is observed but there is a decrease in the Ag absorbance. The effect of ascorbic acid on Ag emission in FAPES may be due to the formation of stable molecular species (for example, Ag_2C_2) when the plasma is present. The first peak is likely due to the residual Ag present on the graphite furnace which gives the same appearance temperature. The later peak with a higher peak temperature can be attributed to the dissociation of these molecular species.

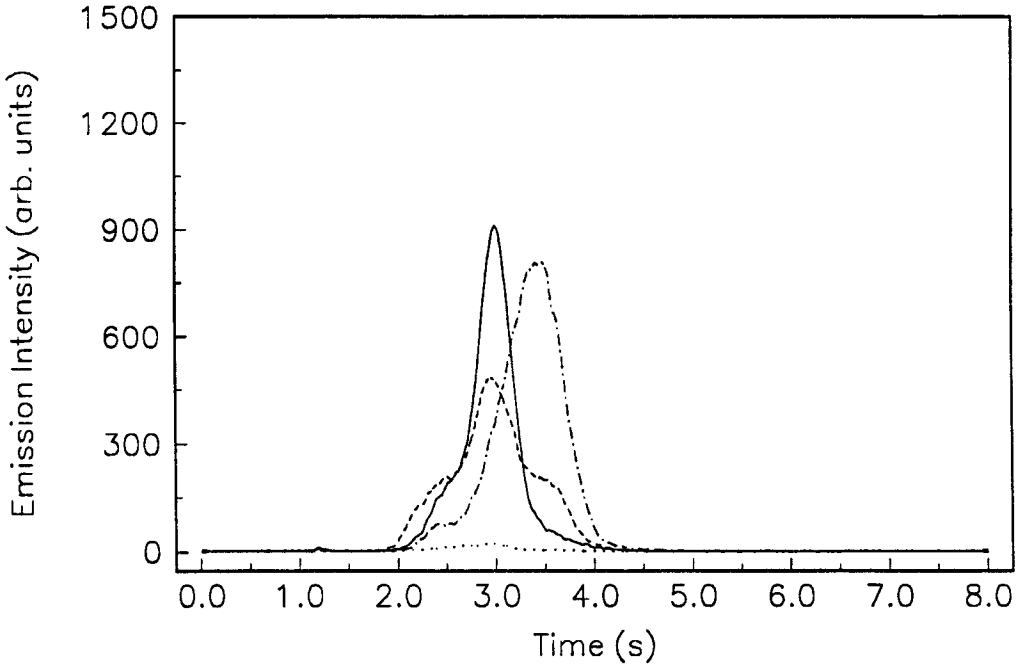

Figure 6.13. Temporal response of the Ag emission signal for the deposition of 0.25 ng of Ag (——), 0.25 ng of Ag in 0.25 % (w/v) ascorbic acid (- - -), and 0.25 ng of Pb in 1.5 % (w/v) ascorbic acid (- · - ·) at an RF power of 20 W.

In addition to ascorbic acid, phosphate modifiers have been used in analysis of Pb in GFAAS [172-174]. Matousek and Brodie used phosphoric acid to obtain higher ashing temperatures and to obtain more repeatable peaks [172]. In a later study, Czobik and Matousek suggested a heterogeneous reaction to form metal-pyrophosphate which decomposes at a higher temperature [173]. In a mass spectral study, Bass and Holcombe

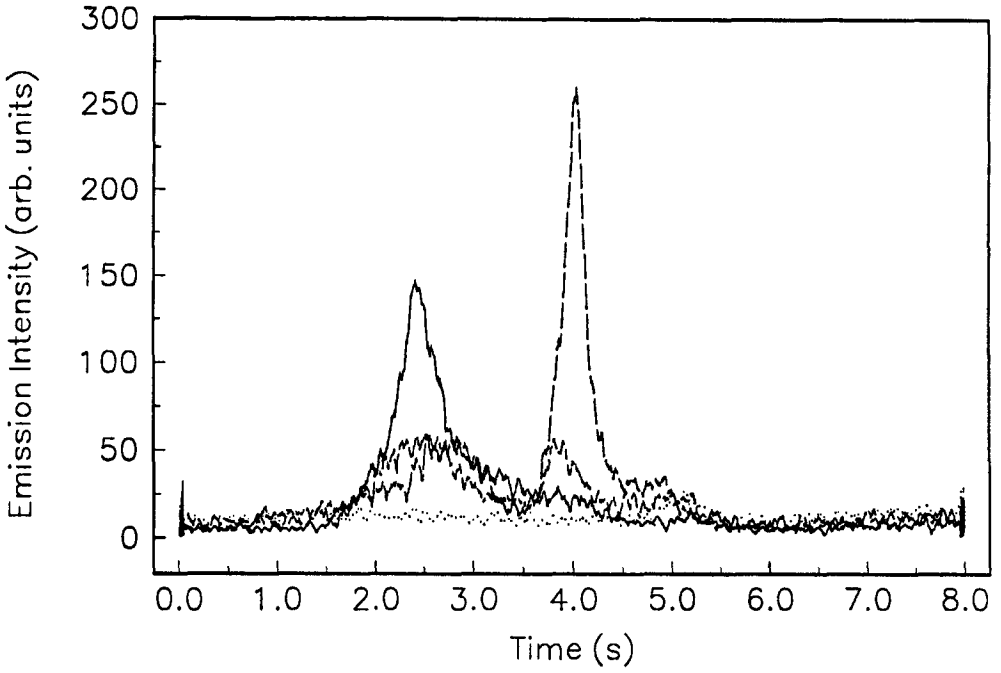

Figure 6.14. Temporal response of the Pb emission signal for 0.5 ng of Pb (———), 0.5 ng of Pb in 2.5 % (v/v) phosphoric acid (— — —), 2.5 % (v/v) phosphoric acid blank (- - -), and water blank (· · ·) at an RF power of 20 W.

proposed the formation of surface bound $Pb_2P_2O_7$ which decomposes to form PbO at 1150 K and immediate reduction of PbO to form Pb [109].

Figure 6.14 depicts the effect of 2.5 % (v/v) phosphoric acid on the temporal response of the Pb emission signal for 0.5 ng of Pb at an RF power of 20 W. The effect of increasing concentration of phosphoric acid on Pb and Ag is to late shift the emission peaks for both elements. When Pb is deposited on the furnace wall and phosphoric acid is deposited on the

RF electrode, no Pb emission signal is observed. This observation suggests that phosphoric acid or its decomposition products form stable molecular species with Pb in the gas-phase. These results shows that phosphoric acid can be used as a matrix modifier for Pb when mixed in solution, or it can act as an interferent in the gas-phase.

6.4 SUMMARY

The effect of NaCl and $NaNO_3$ on the emission intensity of Pb and Ag in FAPES is studied in an effort to understand the interference mechanism and to distinguish the plasma effects from graphite furnace effects. The interferent effect of both NaCl and $NaNO_3$ is to decrease the emission intensity for both Pb and Ag. There are different features associated with the temporal response for analyte with and without interferent which suggest that the NaCl and $NaNO_3$ interferences are due to two different mechanisms.

For Pb in the presence of NaCl and $NaNO_3$, the magnitude of the interference effect is essentially the same over the power range, 20 to 40 W. However, the temporal response of the Pb signal in the presence of $NaNO_3$ shows a different effect from that obtained in the presence of NaCl. In addition, experiments carried out by depositing Pb on the furnace wall and interferent on the RF electrode indicate that both NaCl and $NaNO_3$ interferences are due to two different condensed-phase effects.

The interference effect of NaCl on Pb is due to the formation of Pb chlorides in the condensed-phase which are lost during the slow atomization step of the analyte. The interference effect of $NaNO_3$ on the Pb emission is due to both condensed-phase and gas-phase effects. Lead oxide may be trapped in the $NaNO_3$ matrix to yield a late shift in the Pb emission peak. The gas-phase dissociation of PbO may be hindered by the increased O_2 concentration due to the decomposition products of $NaNO_3$. The heating rate of the graphite furnace likely plays an important role in the dissociation of Pb chlorides and PbO in the gas-phase because a higher gas-phase temperature can be reached rapidly with a higher heating rate of the graphite furnace. Gas-phase reactions are also suggested for the effects of ascorbic acid and phosphoric acid, widely used matrix modifiers, on the Pb emission intensity.

The interference effect of NaCl on the Ag emission is similar to that of NaCl on the Pb emission. The interference mechanism is the loss of Ag as chloride during the slow atomization step of the analyte. For Ag in $NaNO_3$, the interferent effect is caused by the loss of Ag as Ag_2O in the gas-phase. Silver oxide is formed by the oxidation of gaseous-Ag due to the decomposition products of $NaNO_3$. The relatively unstable Ag_2O is dissociated at high RF powers, and hence, show a reduced interference effect as the RF power is increased.

Results obtained for both Pb and Ag show that the major cause of interference from NaCl and $NaNO_3$ for these analytes is the chemical

interference effects found in GFAAS. A slight enhancement in atomic emission is observed at higher amounts of Na (as NaCl) relative to low amounts, probably due to the shift in the analyte equilibrium between atomic and ionic forms of Ag, caused by Na acting as an easily ionizable element (EIE). The temporal overlap of atomic populations of analyte and Na in the gas-phase is only observed for the Ag-NaCl system.

CHAPTER 7

CONCLUSIONS

The basic characteristics of the helium plasma source at 13.56 MHz in Furnace Atomization Plasma Excitation Spectrometry (FAPES) have been investigated as a spectrochemical source for elemental analysis. The primary objective of this study was to characterize the fundamental processes occurring within the plasma source during the analyte atomization, vaporization, and excitation. An effort has been made to distinguish the effect of the plasma on the analyte.

Background spectra for the useful analytical wavelength region, 200 - 500 nm, are dominated by emission features from CO^+, N_2^+, OH, NH, and N_2. The plasma background emission is most intense near the RF electrode and less intense near the graphite furnace wall. This spatial dependence of the background emission intensity arises because of the difference in the RF field strengths at the co-axial RF electrode and at the furnace wall due to the differences in the surface area of the two electrodes. The temporal response of these molecular emission features, during the atomization step of the analyte, shows complex emission characteristics, probably due to the recombination of ionic species with the thermionic electrons and dissociation of molecular species. Experimental results also suggest the presence of higher levels of CO in the FAPES source compared with those in GFAAS. These higher levels of CO in FAPES are due to the

enhanced oxidation of graphite on the RF electrode and on the graphite furnace wall in the presence of the plasma.

The time-averaged Fe and Pb-excitation temperatures are in the range of 3000 - 5000 K at RF powers between 10 and 100 W. The Fe-excitation temperature at 50 W is similar to that of a low power Ar-ICP operating at about 600 W. The measured Fe-excitation temperature is higher near the RF electrode compared with that near the furnace wall. These high excitation temperatures in FAPES are likely caused by either lower radiative and convective heat losses from the plasma in FAPES compared with those from an ICP or higher RF field strength in the plasma in FAPES, or both. These excitation temperatures are also significantly higher than those reported for CFAES. The emission features of CO^+ and N_2^+ indicate that the FAPES source is capable of exciting energy levels as high as 20 eV. However, the energy transfer mechanism in this case is near-resonant charge transfer.

The temporal response of Ag, Pb, and Mn emission signals during the atomization step was studied by simultaneous measurement of atomic absorption and emission signals. Both atomic absorption and emission experiments show a non-uniform temperature distribution along the length of the RF electrode, and it is likely that the RF connector-end of the RF electrode acts as a heat-sink. The RF electrode heats significantly when the plasma is present inside the graphite furnace relative to that without the plasma, but no significant change in the furnace wall temperature is observed. However, late into the atomization step, the temperature of most

parts of the RF electrode lags relative to that of the furnace wall. These differences in temperature-time characteristics between the graphite furnace and the RF electrode cause condensation of analytes on the RF electrode and subsequent second-surface vaporization resulting in two peaks in the temporal emission profile. The relative intensities of these two peaks are affected by the RF power. Analyte condensation on the RF electrode is severe at low RF powers and can be observed when high amounts of analyte are deposited. At present, the effect of the heating rate of the graphite furnace on the temporal response of the emission signals in FAPES is not known. However, it is quite possible that the heating rate of the graphite furnace affects the temperature-time characteristics of the RF electrode relative to the furnace wall, and hence, analyte condensation and second-surface vaporization characteristics from the RF electrode. Furthermore, results obtained for Pb show an early shift in the appearance and peak temperatures in FAPES compared with those in GFAAS. These early shifts are likely due to the changes in the gas-phase composition in the FAPES source, and hence, to a shift in the dissociation equilibria of analyte oxide in the gas-phase.

The similar peak shapes observed for simultaneously measured atomic absorption and atomic emission signals for Ag and Pb show that the temporal emission response of these analytes in FAPES is determined by atomization and vaporization characteristics of the analyte rather than by excitation characteristics. In addition, the time-resolved Pb-excitation temperature shows that the excitation temperature is not affected by the thermionic electrons during the atomization of Pb. At RF powers below 50 W and

furnace temperatures below 1800 K, conditions under which Ag and Pb are present in the plasma, the thermionic electron concentration in the plasma is too low to significantly affect the excitation characteristics of these analytes.

For Mn, an early shift in the emission signal is observed compared with the simultaneously measured atomic absorption signal, probably due to a high energetic excitation region experienced by Mn when second-surface vaporization occurs from the RF electrode. This observed shift for Mn cannot be explained by a change in the Mn-excitation temperature. However, at higher furnace temperatures, thermal excitation of analyte and effects of thermionic electrons may alter the plasma excitation characteristics during the atomization step which may result in complex temporal emission characteristics for analytes with higher appearance temperatures.

The effect of RF power, and hence, the excitation temperature on the analyte emission signal was investigated for Pb. Results show a decrease in Pb emission intensity at RF powers higher than 50 W. This decrease in emission intensity may be due to a premature loss of analyte, a change in excitation characteristics or an increase in ionization of Pb at high RF powers. The highest signal-to-noise and signal-to-background ratios are observed at relatively low RF powers (about 20 W). Lead condensation on the RF electrode at low RF powers does not affect the linearity of the analytical calibration curve, but it does affect the sensitivity and precision for the analytical determination.

The matrix effects of NaCl and $NaNO_3$ on Pb and Ag emission intensities were investigated to understand the interference mechanism and the effect of the plasma. For both Pb and Ag, the major cause of interference effects from NaCl and $NaNO_3$ is chemical interference effects found in GFAAS which lead to a decrease in the atomic emission intensity in FAPES. The major cause of the signal suppression in a NaCl matrix is the formation of relatively stable molecular species and the subsequent losses during the slow atomization step. The interference effect for both Pb and Ag in a $NaNO_3$ matrix is complex and exhibits both condensed and gas-phase effects. A slight enhancement in the Ag atomic emission intensity is observed at higher amounts of Na (as NaCl) relative to low amounts, probably due to the ionization suppression of Ag, caused by Na acting as an EIE. The co-existence of the atomic populations of analyte and Na in the gas-phase is observed for Ag-NaCl system.

Most of the experiments described in this thesis were limited to an atomization temperature of 2100 K and RF powers less than 50 W. At higher furnace temperatures, thermionic electrons affect the plasma impedance, and hence, the RF power dissipated by the plasma. The major course of these thermionic electrons is the RF electrode. Because of the reflected power changes late into the atomization step, application of RF powers higher than 50 W is limited by the appearance temperature of analytes and the atomization temperature of 2100 K. Regardless, these experimental conditions should be extended to use higher atomization temperatures up to 3200 K and to use higher RF powers to achieve the full

analytical capability of graphite furnace methods. The RF power supply and matching network employed for this study were designed for plasma processing work. Therefore, the obvious remedy for the problem of variable RF power dissipation by the plasma is to modify the matching network to deliver a constant RF power during the high temperature ramp of the atomization step. Another option would be the use of a free-running RF oscillator. Furthermore, the electrical characteristics of this atmospheric pressure plasma source are not yet understood. To this end, a comprehensive study of the current-voltage characteristics of the plasma source should be undertaken.

Analyte condensation on the RF electrode at low RF powers can be avoided by depositing the sample on the RF electrode. The experiments carried out by depositing the sample on the RF electrode show that the RF electrode can be employed similar to a L'vov platform in GFAAS. When the RF electrode is employed as a platform to vaporize the analytes, a combination of a high ash temperature and a high heating rate for the furnace should be used to overcome the analyte condensation on the furnace wall. Alternatively, the plasma can be employed with a pre-heated furnace. When a pre-heated graphite furnace is employed, the analyte sample can be introduced into the plasma source *via* a secondary rod, similar to the L'vov method in the early years of GFAAS. This method should overcome the temporal non-isothermality and analyte condensation on the RF electrode because the furnace and the RF electrode are pre-heated before the sample introduction. Furthermore, difficulties arising during a ramp atomization step to maintain

a constant RF power dissipation by the plasma can be avoided because the plasma can be ignited and allowed to stabilize before the sample introduction. Difficult and time consuming sample deposition onto the graphite furnace side-wall can also be avoided by introducing the sample through a secondary rod.

Moreover, specifically for the experimental system employed for this work, the plasma source work-head should be redesigned to reduce the void volume, to allow more efficient and uniform cooling of the graphite furnace and the furnace mount, and to use higher furnace temperatures with a hold-step after the atomization step. In addition, use of a higher heating rate for the graphite furnace during the atomization step is beneficial to improve the analytical characteristics and to reduce the matrix effects in analytical determinations.

In summary, this thesis presents the first study of some important basic characteristics of the helium plasma source in FAPES as a spectrometric source for chemical analysis. This study provides a greater understanding of physical and chemical phenomena occurring in the plasma at a fundamental level. Furthermore, this study identifies the limitations of FAPES and suggests modifications to instrumentation to improve the analytical characteristics for FAPES determinations. Moreover, this thesis suggests further studies to improve the understanding of fundamental processes occurring in the plasma.

BIBLIOGRAPHY

[1] H. A. Laitinen, *Anal. Chem.*, 2305, **45** (1973).

[2] A. Walsh, *Spectrochim. Acta*, 108, **7** (1955).

[3] M. D. Amos and J. B. Willis, *Spectrochim. Acta*, 1325, **22** (1966).

[4] B. V. L'vov, *Spectrochim. Acta*, 761, **17** (1961).

[5] W. Slavin, *Anal. Chem.*, 589A, **58** (1986).

[6] W. G. Schrenk, *Appl. Spectrosc.*, 4, **42** (1988).

[7] S. L. Greenfield, I. L. Jones, and C. T. Berry, *Analyst*, 713, **89** (1964).

[8] R. H. Wendt and V. A. Fassel, *Anal. Chem.*, 920, **37** (1965).

[9] W. Shen, J. A. Caruso, F. L. Fricke, and R. D. Satzger, *J. Anal. At. Spectrom.*, 451, **5** (1990).

[10] J. M. Ottaway and F. Shaw, *Analyst*, 438, **100** (1975).

[11] D. Littlejohn and J. M. Ottaway, *Analyst*, 553, **102** (1977).

[12] H. Falk, E. Hoffmann, I. Jaeckel, and Ch. Ludke, *Spectrochim. Acta*, 333, **34B** (1979).

[13] H. Falk, E. Hoffmann, and Ch. Ludke, *Spectrochim. Acta*, 283, **39B** (1984).

[14] N. E. Ballou, D. L. Styris, and J. M. Harnly, *J. Anal. At. Spectrom.*, 1141, **3** (1988).

[15] D. C. Liang and M. W. Blades, *Spectrochim. Acta*, 1049, **44B** (1989).

[16] R. E. Sturgeon, S. N. Willie, V. Luong, and S. S. Berman, *J. Anal. At. Spectrom.*, 669, **4** (1989).

[17] D. L. Smith, D. C. Liang, D. Steel, and M. W. Blades, *Spectrochim. Acta*, 493, **45B**, (1990).

[18] J. G. Grasselli, *Anal. Chem.*, 677A, **64** (1992).

[19] H. Falk, *J. Anal. At. Spectrom.*, 255, **7** (1992).

[20] S. R. Koirtyohann, *Spectrochim. Acta*, 663, **35B** (1980).

[21] S. R. Koirtyohann, *Anal. Chem.*, 1024A, **63** (1991).

[22] W. Slavin, *Anal. Chem.*, 685A, **54** (1982).

[23] G. M. Hieftje, *J. Anal. At. Spectrom.*, 117, **4** (1988).

[24] B. L'vov, *Anal. Chem.*, 924A, **63** (1991).

[25] G. A. Meyer, *Anal. Chem.*, 1345, **59** (1987).

[26] J. M. Carey and J. A. Caruso, *CRC. Crit. Rev. in Anal. Chem.*, 397, **23** (1992).

[27] H. Matusiewickz, *J. Anal. At. Spectrom.*, 171, **1** (1986).

[28] R. S. Houk, *Anal. Chem.*, 97A, **58** (1986).

[29] G. M. Hieftje and G. H. Vickers, *Anal. Chim. Acta*, 1, **216** (1989).

[30] J. W. Olesik, *Anal. Chem.*, 12A, **63** (1991).

[31] D. Slinkman and R. Sacks, *Anal. Chem.*, 1656, **62** (1990).

[32] D. Slinkman and R. Sacks, *Appl. Spectrosc.*, 155, **45** (1991).

[33] D. Slinkman and R. Sacks, *Anal. Chem.*, 343, **63** (1991).

[34] K. W. Jackson and H. Qiao, *Anal. Chem.*, 50R, **64** (1992).

[35] G. F. Kirkbright, *Analyst*, 609, **96** (1971).

[36] A. Syty, *CRC. Crit. Rev. in Anal. Chem.*, 155, **4** (1974).

[37] R. Woodriff, *Appl. Spectrosc.*, 413, **28** (1974).

[38] R. E. Sturgeon and C. L. Chakrabarti, *Prog. Analyt. Atom. Spectrosc.*, 5, **1** (1978).

[39] S. R. Lawson, F. G. Dewalt, and R. Woodriff, *Prog. Analyt. Atom. Spectrosc.*, 1, **6** (1983).

[40] B. V. L'vov, *Spectrochim. Acta*, 53, **24B** (1969).

[41] H. Massmann, *Spectrochim. Acta*, 215, **23B** (1968).

[42] R. E. Sturgeon and C. L. Chakrabarti, *Spectrochim. Acta*, 231, **32B** (1977).

[43] B. V. L'vov, *Spectrochim. Acta*, 153, **33B** (1978).

[44] W. Slavin and D. C. Manning, *Spectrochim. Acta*, 701, **35B** (1980).

[45] J. E. Marshall, D. Littlejohn, J. M. Ottaway, J. M. Harnly, N. J. Miller-Ihli, and T. C. O'Haver, *Analyst*, 178, **108** (1983).

[46] W. Slavin and G. R. Carnrick, *Spectrochim. Acta*, 271, **39B** (1984).

[47] S. Wu and C. L. Chakrabarti, *Prog. Analyt. Atom. Spectrosc.*, 111, **10** (1987).

[48] W. Frech, D. C. Baxter, and B. Hutsch, *Anal. Chem.*, 1973, **58** (1986).

[49] J. R. Baired and P. D. Coleman, *Proc. IRE*, 1890, **49** (1961).

[50] A. M. Howatson, *An Introduction to Gas Discharges*, Pergamon, London, 1965.

[51] H. A. Schwab and C. K. Manka, *J. Appl. Phys.*, 696, **40** (1969).

[52] R. F. Hotz, *J. Appl. Phys.*, 1500, **41** (1970).

[53] H. A. Schwab and R. F. Hotz, *J. Appl. Phys.*, 1503, **41** (1970).

[54] H. A. Schwab, *Proc. IEEE*, 613, **59** (1971).

[55] D. C. Duckworth and R. K. Marcus, *Anal. Chem.*, 1879, **61** (1989).

[56] M. R. Winchester, C. Lazik, and R. K. Marcus, *Spectrochim. Acta*, 483, **46B** (1991).

[57] B. Chapman, *Glow Discharge Processes*, John Wiley, New York, 1980.

[58] S. M. Levitskii, *Sov. Phys-Tech. Phys.*, 887, **2** (1957).

[59] H. Norstrom, *Vacuum*, 341, **29** (1979).

[60] H. R. Koenig and L. I. Maissel, *IBM J. Res. Develop.*, 168, **14** (1970).

[61] H. Y. Fan, *Phy. Rev.*, 769, **55** (1939).

[62] J. L. Vossen and J. J. O'Neill, Jr., *J. Vac. Sci. Technol.*, 1052, **12** (1975).

[63] J. B. Hasted, *Physics of Atomic Collisions*, Butterworths, London, 1972.

[64] A. von Engel, *Ionized Gases*, Oxford, London, 1965.

[65] H. R. Griem, *Plasma Spectroscopy*, McGraw-Hill, New York, 1964.

[66] P. W. J. M. Boumans, *Theory of Spectrochemical Excitation*, Hilger and Watts, London, 1966.

[67] J. F. Alder, R. M. Bombelka, and G. F. Kirkbright, *Spectrochim. Acta*, 163, **35B** (1980).

[68] M. W. Blades, B. L. Caughlin, Z. H. Walker, and L. L. Burton, *Prog. Analyt. Atom. Spectrosc.*, 57, **10** (1987).

[69] I. Reif, V. A. Fassel, and R. N. Kniseley, *Spectrochim. Acta*, 105, **28B** (1973).

[70] T. D. Hettipathirana and M. W. Blades, *Spectrochim. Acta*, 493, **47B** (1992).

[71] T. D. Hettipathirana and M. W. Blades, *J. Anal. At. Spectrom.*, 1039, **7** (1992).

[72] P. W. J. M. Boumans, *Spectrochim. Acta*, 799, **45B** (1990).

[73] P. W. J. M. Boumans, *Spectrochim. Acta*, 431, **46B** (1991).

[74] R. W. B. Pearse and A. G. Gaydon, *The Identification of Moleculer Spectra*, Chapman and Hall, London, 1976.

[75] C. B. Collins and W .W. Robertson, *J. Chem. Phys.*, 701, **40** (1964).

[76] M. Endoh, M. Tsuji, and Y. Nishimura, *J. Chem. Phys.*, 5368, **79** (1983).

[77] R. E. Sturgeon and H. Falk, *J. Anal. At. Spectrom.*, 27, **3** (1988).

[78] R. E. Sturgeon, S. N. Willie, V. T. Luong, and S. S. Berman, *Anal. Chem.*, 2370, **62** (1990).

[79] R. E. Sturgeon, S. N. Willie, V. T. Luong, and J. G. Dunn, *Appl. Spectrosc.*, 1413, **45** (1991).

[80] R. E. Sturgeon, S. N. Willie, and V. T. Luong, *Spectrochim. Acta*, 1021, **46B** (1991).

[81] A. A. Radzig and B. M. Smirnov, *Reference Data on Atoms, Molecules, and Ions*, Springer-Verlag, Berlin Heidelberg, 1985.

[82] A. Kh. Gilmutdinov, Yu. A. Zakharov, and V. P. Ivanov and A. V. Voloshin, *J. Anal. At. Spectrom.*, 505, **6** (1991).

[83] J. M. Bridges and R. L. Kornblith, *Astrophys. J.*, 793, **192** (1974).

[84] D. Littlejohn and J. M. Ottaway, *Analyst*, 208, **104** (1979).

[85] S. L. Paveri-Fontana, G. Tessari, and G. Torsi, *Anal. Chem.*, 1032, **46**, (1974).

[86] G. Torsi and G. Tessari, *Anal. Chem.*, 839, **47** (1975).

[87] D. A. Bass and J. A. Holcombe, *Spectrochim. Acta*, 1473, **43B** (1988).

[88] S. J. Cathum, C. L. Chakrabarti, and J. C. Hutton, *Spectrochim. Acta*, 35, **46B** (1991).

[89] W. Slavin and D. C. Manning, *Spectrochim. Acta*, 955, **37B** (1982).

[90] P. G. Riby, J. M. Harnly, D. L. Styris, and N. E. Ballou, *Spectrochim. Acta*, 203, **46B** (1991).

[91] A. Savitzky and M. J. E. Golay, *Anal. Chem.*, 1627, **36** (1964).

[92] B. V. L'vov, A. V. Novichikhin, and L. K. Polzik, *Spectrochim. Acta*, 289, **47B** (1992).

[93] P. Hocquellet, *Spectrochim. Acta*, 719, **47B** (1992).

[94] W. Frech, E. Lundberg, and A Cedergren, *Prog. Analyt. Atom. Spectrosc.*, 257, **8** (1985).

[95] C. Duval, *Inorganic Thermogravimetric Analysis*, Elsevier, New York, 1963.

[96] J. McNally and J. A. Holcombe, *Anal. Chem.*, 1105, **59** (1987).

[97] R. W. Fonseca, J. McNally, and J. A. Holcombe, *Spectrochim. Acta*, 79, **48B** (1993).

[98] W. L. Winterbottom and J. P. Hirth, The Vaporization Kinetics of Solid Silver, Ed.; E. Rutner, P. Goldfinger, and J. P. Hirth, *Condensation and Evaporation of Solids*; Science Publishers, New York, 1964; p 348.

[99] J. W. McLaren and R. C. Wheeler, *Analyst*, 542, **102** (1977).

[100] D. C. Manning, W. Slavin, and S. Myers, *Anal. Chem.*, 2375, **51** (1979).

[101] S. G. Salmon, R. H. Davis, Jr., and J. A. Holcombe, *Anal. Chem.*, 324, **53** (1981).

[102] G. F. R. Gilchrist, C. L. Chakrabarti, J. P. Byrne, and M. Lamoureux, *J. Anal. At. Spectrom.*, 175, **5** (1990).

[103] S. Imai and Y Hayashi, *Anal. Chem.*, 772, **63** (1991).

[104] W. C. Campbell and J. M. Ottaway, *Talanta*, 837, **21** (1974).

[105] R. E. Sturgeon, C. L. Chakrabarti, and C. H. Langford, *Anal. Chem.*, 1792, **48** (1976).

[106] M. Suzuki, K. Ohta, T. Yamakita, and T. Katsuno, *Spectrochim. Acta*, 679, **36B** (1981).

[107] G. F. R. Gilchrist, C. L. Chakrabarti, J. T. F. Ashley, and D. M. Hughes, *Anal. Chem.*, 1144, **64** (1992).

[108] R. E. Sturgeon, D. F. Mitchell, and S. S. Berman, *Anal. Chem.*, 1059, **55** (1983).

[109] D. A. Bass and J. A. Holcombe, *Anal. Chem.*, 974, **59** (1987).

[110] J. Drowart, R. Colin, and G. Exsteen, *U.S. Govt. Res. Develop. Rept.*, 20, **40** (1965).

[111] R. E. Sturgeon and S. S. Berman, *Anal. Chem.*, 1268, **57**, (1985).

[112] A. Cedergren, W. Frech, and E. Lundberg, *Anal. Chem.*, 1382, **56** (1984).

[113] D. A. Bass and J. M. Holcombe, *Anal. Chem.*, 578, **60** (1988).

[114] G. F. R. Gilchrist, C. L. Chakrabarti, and J. P. Byrne, *J. Anal. At. Spectrom.*, 533, **4** (1989).

[115] R. E. Sturgeon and S. N. Willie, *J. Anal. At. Spectrom.*, 339, **7** (1992).

[116] B. Smets, *Spectrochim. Acta*, 33, **35B** (1980).

[117] J. Aggett and A. J. Sprott, *Anal. Chim. Acta*, 49, **72** (1974).

[118] J. McNally and J. M. Holcombe, *Anal. Chem.*, 1918, **63** (1991).

[119] C. Th. J. Alkemade, W. Snelleman, G. D. Boutilier, B. D. Pollard, J. D. Winefordner, T. L. Chester, and N. Omenetto, *Spectrochim. Acta*, 383, **33B** (1978).

[120] M. S. Epstein and J. D. Winefordner, *Prog. Analyt. Atom. Spectrosc.*, 67, **7** (1984).

[121] R. E. Sturgeon, S. N. Willie, V. T. Luong, and S. S. Berman, *J. Anal. At. Spectrom.*, 635, **5** (1990).

[122] C. H. Corliss and W. R. Bozman, *Experimental Transition Probabilities for Spectral Lines of Seventy Elements*, NBS Monogrpg # 53, US Dept. Commerce., 1962.

[123] R. E. Sturgeon, S. N. Willie, V. T. Luong, and S. S. Berman, *J. Anal. At. Spectrom.*, 19, **6** (1991).

[124] H. Falk, E. Hoffmann, and Ch. Ludke, *Prog. Analyt. Atom. Spectrosc.*, 417, **11** (1988).

[125] J. M. Harnly, D. L. Styris, and N. E. Ballou, *J. Anal. At. Spectrom.*, 139, **5** (1990).

[126] W. M. G. T. van den Broek and L. de Galan, *Anal. Chem.*, 2176, **49** (1977).

[127] J. M. Ottaway and F. Shaw, *Appl. Spectrosc.*, 12, **31** (1977).

[128] W. Slavin, and D. C. Manning, *Anal. Chem.*, 261, **51** (1979).

[129] B. Welz, S. Akman, and G. Schlemmer, *J. Anal. At. Spectrom.*, 793, **2** (1987).

[130] M. W. Blades, Ph.D. Thesis, University of Alberta, Canada, 1980.

[131] M. W. Blades and G. Horlick, *Spectrochim. Acta*, 861, **36B** (1981).

[132] R. R. Williams, *Anal. Chem.*, 1638, **63** (1991).

[133] G. Torsi and G. Tessari, *Anal. Chem.*, 1812, **45** (1973).

[134] D. C. Gregoire, C. L. Chakrabarti, and P. C. Bertels, *Anal. Chem.*, 1730, **50** (1978).

[135] N. G. Zhou, W. Frech, and L. de Galan, *Spectrochim. Acta*, 225, **39B** (1984).

[136] H. Falk, *CRC. Crit. Rev. in Anal. Chem.*, 29, **19** (1988).

[137] P. Schramel, *Anal. Chim. Acta*, 414, **72** (1974).

[138] R. E. Sturgeon, C. L. Chakrabarti, I. S. Maines, and P. C. Bertels, *Anal. Chem.*, 1240, **47** (1975).

[139] R. E. Sturgeon, C. L. Chakrabarti, and P. C. Bertels, *Anal. Chem.*, 1250, **47** (1975).

[140] J. M. Harnly, *J. Anal. At. Spectrom.*, 43, **3** (1988).

[141] E. H. Piepmeier, *Anal. Chem.*, 1296, **48** (1976).

[142] J. M. Laeven and H. C. Smit, *Anal. Chim. Acta*, 77, **176** (1985).

[143] E. Voigtman *Appl. Spectrosc.*, 237, **45** (1991).

[144] U. Kale and E. Voigtman *Appl. Spectrosc.*, 1636, **46** (1992).

[145] G. R. Kornblum and L. de Galan, *Spectrochim. Acta*, 71, **32B** (1977).

[146] A. Batal, J. Jarosz, and J. M. Mermet, *Spectrochim. Acta*, 983, **36B** (1981).

[147] D. Littlejohn, J. N. Egila, R. M. Gosland, U. K. Kunwar, and C. Smith, *Anal. Chim. Acta*, 71, **250** (1991).

[148] J. P. Matousek, *Prog. Analyt. Atom. Spectrosc.*, 247, **4** (1981).

[149] C. Veillon and M. Margoshes, *Spectrochim. Acta*, 503, **23B** (1968).

[150] P. W. J. M. Boumans and F. J. DeBoer, *Spectrochim. Acta*, 355, **31B** (1976).

[151] T. D. Hettipathirana and M. W. Blades, *J. Anal. At. Spectrom.*, in press.

[152] J. D. Stafford and J. A. Holcombe, *J. Anal. At. Spectrom.*, 35, **3** (1988).

[153] C. W. Huie and C. J. Curran, Jr., *Appl. Spectrosc.*, 1307, **42** (1988)

[154] R. Herrmann and C. T. J. Alkemade, *Chemical Analysis by Flame Photometry*, Wiley-Interscience, New York, 1963.

[155] G. F. Larson, V. A. Fassel, R. H. Scott, and R. N. Kniseley, *Anal. Chem.*, 238, **47**, (1975).

[156] D. J. Kalnicky, V. A. Fassel, and R. N. Kniseley, *Appl. Spectrosc.*, 137, **31** (1977).

[157] M. W. Blades, and G. Horlick, *Spectrochim. Acta*, 881, **36B** (1981).

[158] R. Rezaaiyaan, J. W. Olesik, and G. M. Hieftje, *Spectrochim. Acta*, 73, **40B** (1985).

[159] L. J. Prell, C. Monnig, R. E. Harris, and S. R. Koirtyohann, *Spectrochim. Acta*, 1401, **40B** (1985).

[160] M. S. Hendrick, M. D. Seltzer, and R. G. Michel, *Spectrochim. Acta*, 335, **41B** (1986).

[161] J. P. Matousek, B. J. Orr, and M. Selby, *Spectrochim. Acta*, 415, **41B** (1986).

[162] S. Dahai, Z. Zhanxia, Q. Haowen, and C. Mingxiang, *Spectrochim. Acta*, 391, **43B** (1988).

[163] C. LeBlanc and M. W. Blades, *J. Anal. At. Spectrom.*, 99, **5** (1990).

[164] E. J. Czobik and J. P. Matousek, *Anal. Chem.*, 2, **50** (1978).

[165] W. Slavin, G. R. Carnrick, and D. C. Manning, *Anal. Chem.*, 163, **56** (1984).

[166] R. H. Eklund and J. A. Holcombe, *Anal. Chim. Acta*, 97, **109** (1979).

[167] J. A. Holcombe, G. D. Rayson, and N. Akerlind, Jr., *Spectrochim. Acta*, 319, **37B** (1982).

[168] W. Frech, and A. Cedergren, *Anal. Chim. Acta*, 57, **88** (1977).

[169] K. Visser, F. M. Hamm, and P. B. Zeeman, *Appl. Spectrosc.*, 620, **6** (1976).

[170] J. G. T. Regan, and J. Warren, *Analyst*, 447, **103** (1978).

[171] M. Tominaga, and Y. Umezaki, *Anal. Chim. Acta*, 279, **139** (1982).

[172] J. P. Matousek and K. G. Brodie, *Anal. Chem.*, 1606, **45** (1973).

[173] E. J. Czobik and J. P. Matousek, *Talanta*, 573, **24** (1977).

[174] D. L. Tsalev, V. I. Slaveykova, and P. B. Mandjukov, *Spectrochim. Acta Rev.*, 225, **43** (1990).